CONTINUOUS FLOW PLATFORMS FOR THE SYNTHESIS OF HIGH-QUALITY SEMICONDUCTOR NANOCRYSTALS

BY

VIVEK KUMAR

DISSERTATION

Submitted in partial fulfillment of the requirements
for the degree of Doctor of Philosophy in Chemical Engineering
in the Graduate College of the
University of Illinois at Urbana-Champaign, 2016

Urbana, Illinois

Doctoral Committee:

Professor Paul J.A. Kenis, Chair
Professor Hong Yang
Assistant Professor Ying Diao
Associate Professor Moonsub Shim
Dr. Kishori Deshpande, The Dow Chemical Compan

Abstract

Semiconductor nanocrystals are of great interest due to their unique optical and electronic properties that are intermediate between bulk semiconductors and molecules. These nanoparticles find use in various applications ranging from electronics (light emitting diodes, photovoltaics) to photocatalysis and biolabeling. Typically, these nanoparticles are produced via batch synthesis routes that suffer from various issues, including slow mixing, slow heating/cooling, and lack of batch-to-batch reproducibility. These issues escalate further when increasing the scale of the production, thereby hindering their application on a commercial scale. Continuous flow synthesis can be an alternative approach that may enable high throughput and superior control of particle size and quality. However, since its first application in the early 2000s, most of the literature remains focused on continuous flow synthesis of Cd-based dots. Recently, the use of Cadmium (Cd) has been banned for many applications owing to its toxicity. Therefore, there is an immediate need for robust continuous flow reactors that enable synthesis of high quality Cd-free semiconductor nanoparticles.

The modular continuous flow reactor reported in this work enables multistep, high temperature (up to 750 °C), air-sensitive synthesis of semiconductor nanocrystals involving solid and/or viscous reactants. Additionally, the millifluidic dimensions of the reactor allow for high working flow rates (> 10 ml/min) that translate into a production rate of about 150 g/day of nanocrystals. This this configuration is well suited for scale-up. The developed continuous flow reactor is designed to achieve quick heating and cooling times (< 1 s), thereby providing superior control over reaction conditions c

ompared to the level of control that can be achieved in conventional batch synthesis techniques. The flow reactor is composed of fracture-resistant material, stainless steel, which is compatible with a wide variety of solvents at high temperatures. Furthermore, the modular flow reactor allows for inline characterization of the product, through absorbance and fluorescence spectroscopy. To demonstrate the applicability of the modular continuous flow reactor, we used the reactor to synthesize multi-layered Cd-based core-shell dots, CdSe bipods and nanorods, ZnSe nanorods, and highly luminescent InP/ZnSeS core-shell dots.

The need for superior size control, shape selectivity and high reproducibility has resulted in a shift from conventional batch synthesis techniques to alternate synthesis routes. In the wake of such tight requirements, continuous flow syntheses, especially those relying on microfluidics, have emerged as viable routes for the synthesis of high-quality semiconductor nanocrystals. In general, continuous flow syntheses provide higher control over reaction conditions, for example mixing and heating times. We started by identifying the right material of construction and fabrication technique for building a continuous flow reactor that could withstand high temperatures. Design and fabrication of a simple oil-bath based continuous flow reactor and its application to demonstrate proof-of-principle syntheses of multi-layered Cd-based core-shell nanocrystals is discussed in **Chapter 2**. Use of heating media such as oil or hot water limits the maximum temperature attained by the reactor and is not suited for scale-up. To obviate the use of oil as a heating medium, a new continuous flow reactor was developed that uses a solid-state heating technique. The reactor configuration was further modified and coupled with a Schlenk line to enable high temperature, air-sensitive synthesis of semiconductor nanocrystals. **Chapter 3** describes the design, fabrication, and operation of the new continuous flow reactor setup to synthesize anisotropic semiconductor nanocrystals, both Cd-based (CdSe nanorods/bipods) and Cd-free (ZnSe nanorods). Next, an inline mixer and a second reactor were added to the setup to enable multistep synthesis of InP/ZnSeS dots. Furthermore, the reactor design was upgraded to minimize the residence time distribution effects by the effective use of static mixers inside the reactor modules. Two flow cells were installed downstream of the reactors to enable inline spectroscopic characterization of the product. The design, fabrication, and operation of this multistep reactor setup are discussed in **Chapter 4**. Effective and fast mixing is critical to obtain uniform nanocrystals. However, fast mixing comes at the expense of high pressure drop. To alleviate this problem, we designed a high-throughput millifluidic herringbone mixer which is discussed in **Chapter 5**.

In summary, the modular continuous flow reactor developed here will pave the path for high-throughput synthesis of high-quality semiconductor nanocrystals. The described platform equipped with inline characterization capabilities can also be used to study the reaction kinetics of the aforementioned syntheses, which are not fully understood at present. Furthermore, the reactor also can be used for syntheses other than semiconductor nanocrystals, especially those that require stringent conditions, including high temperature, inert conditions, and fast mixing.

Acknowledgments

I am extremely grateful to everyone who has motivated, supported, or helped me in any way to make my journey through the doctoral program a memorable one.

First and foremost, I would like to thank my PhD adviser, Dr. Paul J. A. Kenis for his critical guidance and constant support that helped set my project on the right course. His immaculate attention to details and relentless pursuit of perfection has inspired me in many ways to give my best to the project. Dr. Kenis has been very encouraging and supportive of my endeavors at UIUC outside of research. As he would often say, "PhD is a tortuous journey that makes a man out of a boy", his critical attitude and stern feedback have helped me transition into an independent problem solver. He has been more like a strict and patient father to a "juvenile" child. I believe the set of skills, both personal and professional, that I have acquired under his tutelage are going to be an asset for life that will help me in my future engagements. I would also like to thank all the committee members, Dr. Hong Yang, Dr. Moonsub Shim, Dr. Kishori Deshpande, and Dr. Ying Diao, for providing their valuable insight and feedback on the project.

These past 5 years at UIUC have been an absolute delight, thanks to all the current and former members of the Kenis group who have helped me improve, both as a researcher and person. In particular, I would like to thank Dr. Matt Naughton, who mentored me and helped me to get up to speed in the initial years of the project. I learned a great deal by working alongside him on the project. I would further like to make a special mention of Dr. Amit Desai, Dr. Sudipto Guha, Dr. Sachit Goyal, and Dr. Adam Hollinger for their invaluable input and expert opinions that helped me grasp the project better, given that the project was completely different from the group's area of expertise. I would like to extend my gratitude to Joseph Whittenberg for helping me with the static mixer project in particular, and the quantum dot project in general. I cannot emphasize enough the importance of fruitful discussions with Jeremy Schieferstein, Sichao Ma, and Sumit Verma about various topics spanning science, philosophy, and politics that greatly enriched my experience in the Kenis group. I would like to thank Sarah Leonard for helping me

with some of the important project- and lab-related logistics. Last but not the least, I am extremely grateful to Elizabeth Horstman, Byoungsu Kim, Dr. Ashtamurthy Pawate, Dr. Matthew Byrne, Dr. Ritika Mohan, Dr. Daria Khvostichenko, Dr. Michael Thorson, and Dr. Joshua Tice, Dr. Huei-Ru "Molly" Jhong for being absolutely delightful colleagues to work with in the Kenis group.

This project would not have been possible without the vital contributions from a pool of immensely talented undergraduates, Yolanda Bonita, Hector Aaron Fuster, Utkarsh Ramesh, and Karthik Balakrishnan. They have been the backbone of the project helping me out with the reactor fabrication and installation, experiments, and product analyses.

My project is a part of a collaborative effort that includes several research groups at UIUC and the Dow Chemical Company. I am thankful to all the people involved in the collaboration for their support throughout the project. In particular, I would like to thank Dr. Yang and Dr. Shim for providing vital input that helped me understand the fundamental principles of nanocrystal synthesis. I would also like to thank Nuri Oh, You Zhai, and Steven Warren for helping me out with various analysis techniques that further bolstered my understanding of these nanocrystals. The expert opinions, feedback, and fruit discussions with Dr. Kishori Deshpande at the Dow Chemical Co. have greatly helped me make rapid progress in my project. Her close involvement in the project ensured that I was always headed in the right direction. I would further like to mention Dr. Peter Trefonas, Dr. Kevin Howard, Dr. Jieqian Zhang, Dr. Park Jong, Dr. Trevor Ewers, and Dr. Anne Leugers for their constant guidance throughout the project.

I would like to greatly acknowledge Mike Harland, Supervisor, SCS Machine shop, who sat down patiently with me through the long discussions about design of the various reactors. His expert input and feedback has inspired some of the innovative reactor designs studied in this thesis. I would like to pay homage to late Rob Brown (Senior Mechanic, SCS Machine Shop) who was kind and accepting enough to accommodate my last minute amends to the reactor design. I would like to thank Dr. Kiran Subedi, Rudi Laufhutte, and Ratna Dutta for their prompt services at the SCS Microanalysis Lab. I would like to extend a note of thanks to Wacek Swiech and Honghui Zhou at the Materials Research Laboratory for being a great help with the TEM imaging of the semiconductor nanocrystals. My sincere thanks to Danielle Gray and Jeffrey

Bertke at the SCS George L. Clark X-Ray Facility for their help with the X-Ray diffraction technique. I would like to mention Natalie Staciewicz at the Materials Research Laboratory for helping me out with the X-Ray Fluorescence spectroscopy.

I would also like to thank all my ChBE and non-ChBE friends particularly, Prakalp, Ankur, Mayank (Chchaa), Shikha, Ankita (Bhutani), Shashank, Dileep (Kini), Advitya, Shikhar, Shishir, Pranav, Piyush, Manila, Jeremy, Joe, Sichao, Sumit, Steven, Dan, Laura, Rob, and Danielle for their love, support, candid discussions, and for making my stay in Urbana-Champaign enjoyable. They have been family away from home.

Most importantly, I owe this degree to my family for their constant motivation and immense support that have always helped me make important decisions in my life. This especially goes out to my father who inspired me to be an engineer and instilled in me the values of hardwork and sincerity. I cannot emphasize enough the sacrifices made by my mother to get me to the position I am in today. She always encouraged me to dream big and never give up. I am extremely grateful to my elder brother who taught me everything that I know today and my loving sisters who were always there when I needed them. Finally, I am extremely grateful to my wife for her undeniable belief in my abilities that inspires me to aim big and her selfless love that fills my life with pure joy.

To my parents, siblings, and wife

Table of Contents

Chapter 1
INTRODUCTION TO SEMICONDUCTOR NANOCRYSTALS

Quantum dots are nanometer-sized semiconductor particles that bridge the gap between bulk semiconductors and molecules. Their size lends them unique properties that are intermediate between bulk semiconductors and molecules that leads to size-dependent bandgap energy, thereby enabling tunable optoelectronic properties. They find use in a variety of applications including, solid-state lighting, display, photovoltaics, photocatalysis, wavefunction engineering, optically induced light modulation, among many more. The recent thrust in the field of synthesis and application of quantum dots is exemplified by the fact that over 15,000 journal publications related to quantum dots have been published in just the last two decades[1].

The key challenge in the field of quantum dots production is to synthesize monodisperse quantum dots whose size can be effectively controlled. The first major development in this area came in early 1990s when a controlled synthesis of small quantum dots was achieved using organometallics. Since then, the methods for quantum dot synthesis have undergone many improvements, including hot-injection synthesis, heat-up synthesis, improved size control and selectivity, organometallic synthesis in hot coordinating and non-coordinating solvents. Despite the major improvements in batch synthesis techniques, quantum dots have yet to become a commercial success partly due to the high costs associated with their synthesis. The high production costs engender from a lack of *reliable* scalable methods to produce high quality, monodisperse nanoparticles. Therefore, continuous flow synthesis mode came across as a viable synthesis technique for scalable production of quantum dots. In addition to being cost effective, continuous synthetic techniques enable superior control over reaction conditions compared to the

batch synthesis techniques. The field of continuous flow synthesis of quantum dots has gained a lot of momentum since the first reported synthesis of quantum dots using a microfluidic system in 2002. However, the majority of the literature still remains focused on Cadmium (Cd)-based dots. There is no account of any major breakthrough on continuous flow synthesis of anisotropic nanocrystals or luminescent Cd-free particles in the literature. Furthermore, the recently implemented regulations against the use of Cadmium in consumer products have forced the field to focus on continuous flow synthesis of Cadmium-free quantum dots with properties of interest for commercial applications.

1.1 Quantum dots: properties and applications

Quantum dots act as a bridge between bulk semiconductor and molecules. They are of great interest due to their tunable electronic and optical properties. An important property of semiconductor materials is the energy band gap that separates the conduction and valence energy bands. For bulk semiconductors, this energy gap remains fixed depending on the identity of the material (**Figure 1.1**). However, the aforementioned rule holds no longer true as the size of the semiconductor decreases to about 20 nm for most of the semiconductors[2]. The effect of the particle size on the band gap of the nanocrystals becomes prominent for the size range of 10 nm or below[3]. This size range corresponds to a regime of quantum confinement for which the electronic excitations feel the presence of the particle boundaries and respond to the changes in the particle size by adjusting their energy spectra giving rise to a phenomenon known as quantum size effect and the nanoparticles that exhibit such an effect are often referred to as quantum confined materials. In general, when a semiconductor absorbs a photon an electron is transferred to the conduction band resulting in the generation of an electron-hole pair, called an exciton. However, in the case where the physical boundaries or the size of the semiconductor

becomes comparable or smaller than the Bohr-exciton radius of the bulk semiconductor, the particle exhibits quantum confinement properties. **Table 1.1** lists the Bohr-exciton radius of the some commonly used semiconductors[4]. In quantum confinement regime, the energy band-gap of the particles increases with the decrease in their size (**Figure 1.2** and **1.3**). As a rule of thumb, the energy band-gap is directly proportional to$1/R^2$, where 'R' is the radius of the nanoparticle (assumption of particle in a box holds)[5]. As the size of the particles goes below the exciton Bohr radius, continuous energy levels collapse into discrete energy bands exhibiting "atom-like" behavior[3]. The splitting of continuous energy bands into discrete energy bands becomes more prominent with the decreasing particle size (**Figure 1.3**)[6]. The tunable band-gap based on size and composition enables effective control over the emission properties of the quantum-confined nanoparticles. This property makes these nanoparticles indispensable in the field of electronics (**Figure 1.2**)[7].

In free space, electron and hole are strongly correlated, which in simple terms means that a hole follows an electron wherever it goes due to strong electronic interaction. However, in a quantum confined regime, the effect of confinement becomes much stronger than the electrostatic force, therefore resulting in holes and electrons being no more correlated[8]. This phenomenon adds another unique property to the quantum dots that results in uncorrelated hole-electron pair[9].

Table 1.1. Exciton Bohr radii of several direct and indirect band gap semiconductors[10]

Semiconductor	CdSe	CdS	CdTe	InP	GaN	GaP	ZnSe	Si	Ge
Radius (nm)	5.6	2.9	2.8	12	3.6	1.17	4.6	4.9	17.7

The term "quantum dot" refers to the spherical semiconductor nanoparticles that exhibit quantum confinement properties. However, besides spherical shaped particles, other shapes,

including triangles, bipods, tripods, tetrapods, rice, arrow, exhibit quantum confinement properties as well since one or more dimensions for these nanoparticles is comparable or smaller than the Bohr-excitonic radius of the bulk semiconductor. For the purposes of this manuscript, the term quantum dots will be interchangeably used for semiconductor nanocrystals, unless specified otherwise. Depending on the number of physical dimensions (out of the three) that are comparable to the Bohr excitonic radius the nanoparticles exhibit 1-dimensional (wells), 2-dimensional (wires/rods), or 3-dimensional (quantum dots) quantum confinement (**Figure 1.4**). The quantum confinement effect varies strongly depending on the material geometry[11,12], for example, quantum dots (3-D quantum confined) exhibit more prominent quantum confinement effects than 2-D confined nanowires.

Core-shell QDs: Quantum dots usually have a high surface to volume ratio due to their small size which results in high chemical potential due to an active surface. Therefore, these quantum dots are extremely susceptible to agglomeration. To make a stable quantum dot colloidal solution, organic ligands are typically employed that attach to the dots by forming stable complexes with the dangling bonds of the surface atoms (**Figure 1.5**). However, in most cases these organic ligands do not cover the entire quantum dot surface resulting in the creation of surface-related trap sites. These trap sites lead to fast non-radiative recombination of excitons, thereby significantly reducing the quantum yield of the quantum dots. Therefore, passivation of quantum dot surface is critical to ensure high performance of these nanomaterials. To passivate the surface of quantum dots effectively, a layer of inorganic shell is grown around the nanocrystals forming what is more commonly known as the core-shell structure. However, certain considerations including, similar lattice structure and constants, and band gap alignment are evaluated to choose the suitable candidate for the inorganic shell layer. Core-shell structures are generally divided into three categories based on their band gap alignment – Type I, Type $I^{1/2}$,

and Type II (**Figure 1.6**). In the Type I structure, the band gap for one semiconductor material lies completely within that of the other, *e.g.*, CdSe/ZnS[13]. Therefore, both the electron and hole are confined in the same material (with the narrower band gap). Similarly, in the Type I[1/2] structure, only one charge carrier is confined to one semiconductor, while the other is delocalized over the entire core-shell structure. Type II structure has different charge carriers delocalized over separate materials as a result of staggered band gap alignment, *e.g.*, CdTe/CdSe[14]. Recently, an alternative form of Type I structure, also known as the "Reverse Type I", has been developed by overgrowing a shell with a narrower band gap around a core with a higher band gap. This leads to partial delocalization of (at least one) charge carrier in the shell, thereby allowing to tune the emission properties by varying the shell thickness, *e.g.*, CdS/HgS[15].

Application: Quantum dots find use in a range of optoelectronic devices, including light emitting devices (solid state lighting)[16-19], lasing[20], displays[21,22], photoconductors[23], photovoltaics and photodetectors[23-25], among many more. For light emitting devices, spatial accumulation of electrons and holes in the same volume leads to the recombination of electron and holes on a film composed of quantum dots resulting in bright photon emission. Broad spectral tunability coupled with high color purity makes these particles an ideal choice for displays and solid state lighting. As shown in **Figure 1.7**, quantum dots enable higher color gamut than the best competing products in the market[7]. In the case of solid state lighting, quantum dots possessing narrow full width at half maximum (fwhm) enable color rendering index (CRI) higher than 90 at lower correlated color temperature (CCT), which was earlier not possible with conventional inorganic phosphors[7]. Laser requires additional gains for the quantum dots to be used. High photostability, narrow and symmetric emission spectra, and broad absorption spectra[26] enable simultaneous excitation of multiple fluorescence colors, thereby making quantum dots a good candidate for biolabeling and biosensor applications[27-31]. In photovoltaics, doped quantum dot

films are combined with a metal or another semiconductor, along with asymmetric electrodes to form a complete photovoltaic device[32-36].

1.2 Synthesis principles of semiconductor nanocrystals

The majority of the quantum dot-based applications require highly crystalline, monodisperse quantum dots for proper implementation in the final products. Therefore, understanding the basic process that determines the final size distribution and morphology of these nanocrystals has been of prime importance. Quantum dot synthesis, at the heart of it, is quintessentially a crystallization process. Therefore, the fundamentals of crystallization apply well to quantum dots synthesis.

Classic Studies of LaMer and Dinegar: A major breakthrough in understanding the crystallization process came about in 1950s in the form of Classic studies by La Mer and Dinegar[37]. Building upon some of the existing theories by Gibbs, Thompson, and Debye, La Mer and Dinegar were able to show that the synthesis of monodisperse colloids requires a temporally discrete nucleation step, followed by a slower and controlled growth step (**Figure 1.8**). For purposes of this work, we define "Supersaturation" (S) as [log ($C_{monomer}/C_{saturation}$)], which is indicative of the level of supersaturation in the solution. Essentially, rapid addition of reagents to the reaction vessel leads to a spike in the concentration of precursors/monomers. A sudden spike in the concentration of monomers results in high supersaturation, thereby allowing the monomers to overcome the high energy barrier required for spontaneous nucleation. This step is almost instantaneous and leads to the formation of very small clusters, also called "embryos". These embryos are formed when the Supersaturation level is above a certain critical concentration of the monomers, also referred to as the "Threshold supersaturation" or "Nucleation threshold", determined by the required Gibbs free energy of the monomers for spontaneous nucleation. Therefore, rapid injection leads to a very short period of nucleation, rightly called the "burst

nucleation" for its brevity. As monomers are consumed to form nuclei during the burst nucleation period, the monomer concentration drops below the nucleation threshold (**Figure 1.8**). Once the concentration of monomers drops below the nucleation threshold, no more spontaneous nucleation takes place. However, post burst nucleation, the monomers start to deposit on the formed nuclei present in the solution since the concentration of monomers is still above the saturation limit. This zone is characterized by a slow and controlled growth in the size of the nuclei and is therefore called the "growth zone". The growth rate of the colloidal particles in the growth zone depends on many parameters, most importantly, their size. In case of spherical particles, smaller particles grow at a faster rate than bigger particles [38]. The differential growth rate based on the size of the particles leads to "size-focusing" [39]of the population if growth is allowed for an optimum duration. For instance, in **Figure 1.9**, the two particles start at different radii, $r_1^0 and\ r_2^0$. After about four time units, both the particles reach similar final radii, $r_1^4 and\ r_2^4$ respectively, despite starting off with very different sizes. It is worth noting that the inverse relationship between the growth rate and particle size comes from the diffusion-controlled growth mode, which results in the rate of increase of the particle volume equal to the diffusion rate of the monomers from the solution to the particle surface[40]. In the diffusion-controlled growth regime, when the supersaturation value (S) is higher than 0 (and lower than the Nucleation threshold), all of the monomers that diffuse onto the crystal surface immediately precipitate. However, when the supersaturation is nearly 0 or even negative, which essentially means the concentration of molecules is lower than the solubility of the particles, then the mass transport is reversed resulting in the dissolution of the particles. This process is called Ostwald ripening that occurs when the driving force for crystallization weakens leading to the growth of the big particles at the expense of dissolution of the smaller particles that have a high surface energy. In general, Ostwald ripening results in "size defocusing" of the crystal population. [41-44]

The first successful synthesis of colloidal quantum dots was performed by Brus and Henglein in late 1980s. They employed weak reducing agents, for instance, H_2S in case of CdS, to trigger precipitation reaction in single-phase aqueous solutions in the presence of surfactants or polymer-type stabilizers to avoid agglomeration of colloidal nanocrystals[45-49]. In parallel, other synthetic routes including, two-phase synthesis that involve arrested precipitation of colloidal quantum dots within inverse micelles, were also developed. However, the aforementioned synthesis routes occurred at low temperatures (typically < 100 °C) and therefore failed to produce high-quality nanocrystals with well-defined absorption and fluorescence spectral features.

Hot injection synthesis technique: It wasn't until 1993 that the first seminal work towards obtaining a high quality, monodisperse (σ < 10%) colloidal quantum dots was published by Bawendi and his colleagues[50]. The synthesis was based on the rapid injection of "cold" (room temperature) organometallic precursors in a hot bath of high-boiling organic solvent containing coordinating ligands. The bath was typically maintained at an elevated temperature, typically in the range of 150 °C to 300 °C. This synthesis technique is popularly known as the "Hot injection" technique. Specifically, Bawendi *et al.* demonstrated the synthesis of highly crystalline monodisperse CdX particles (X – Selenium (Se), Sulfur (S), Tellurium (Te)) by using dimethyl Cadmium and Se dissolved in Trioctylphosine (TOP) as the metal precursors and Trioctylphosphine oxide (TOPO) as the coordinating solvent. Hot injection of organometallic precursors leads to instantaneous nucleation of CdX. However, post hot injection of the "cold" precursors, the temperature of the bath drops to less than 200 °C, thereby stemming any further nucleation. As the temperature rises again slowly (although < 300 °C), the free CdX molecules start to deposit on the nuclei. The growth of nuclei occurs in a controlled (and slower) manner due to the presence of TOPO that act as capping agents (**Figure 1.10**). The entire process

harkens back to La Mer and Dinegar's work in which they demonstrated synthesis of monodisperse hydrosols by temporally disengaging nucleation and growth regimes. Hot injection technique has been successfully applied to various compositions, including variants of CdX[51-55], InP[56-58], InAs[59], InAs/ZnSe, ZnSe[60], ZnO[61], PbS[62], PbSe[63-65], PbTe[66], ever since its first application in 1993. In addition, Bawendi's original work led to the adoption of organometallics as the choice of precursor for quantum dots synthesis in subsequent works.

Heat-up synthesis technique: Heat-up method is another synthesis technique that is gaining traction to obtain monodisperse colloidal quantum dots. The strength of the method lies in the fact that there is no noticeable synthetic operation to induce size uniformity. As the name suggests, heat-up synthesis technique involves mixing the precursors at low temperature followed by raising the temperature of the bath to the reaction temperature[67,68]. High supersaturation is attained when the temperature is high enough to trigger the reaction resulting in nucleation. A period of quick nucleation consumes the monomers relieving the level of supersaturation, thereby aiding the transition to the size-focusing growth regime. The Cao group effectively used the heat-up technique to obtain monodisperse CdSe and CdTe nanoparticles[69]. Recently, the Reiss group adopted the technique to synthesize highly luminescent, monodisperse Indium-based quantum dots as well[70]. Beside semiconductor nanocrystals, this technique has been demonstrated to synthesize high quality Manganese and Zirconium-based particles[71,72], FePt[67], CeO_2[73,74], Gd_2O_3[75] nanoparticles. The heat-up method, due to its convenient operation steps, is more suited for large scale synthesis of monodisperse quantum dots on a continuous scale compared to the hot injection technique. In this work, we have applied the heat-up synthesis technique to obtain highly luminescent high quality semiconductor nanoparticles on a continuous flow reactor.

1.3 Continuous flow synthesis techniques for semiconductor nanoparticles

Quantum dots are still more expensive compared to the competing inorganic phosphors. This, along with some other operational issues, proves to be an impediment to the application of quantum dots on a commercial scale. The majority of the synthesis of highly luminescent, highly crystalline semiconductors nanocrystals performed on a batch scale with a typical volume of the order of 10 mL. Furthermore, batch syntheses are known to suffer from challenges, including slow mixing, slow and inefficient temperature control, and batch-to-batch reproducibility[76-80]. These issues escalate further with the scale of the synthesis. Therefore, a need for superior control over reaction conditions coupled with reduction in the cost of production led to the idea of synthesis quantum dots on a continuous scale. Along with scalable production of quantum dots, precise control over reaction conditions in continuous flow reactors enabled a better understanding of the intricate physical processes involved in the formation of these nanocrystals with the help of sophisticated analytical tools that can be integrated with the reactor setup to provide real time information[81-83].

Since the first reported use of a microfluidic reactor to prepare nanocrystals was as recent as 2002[84], microfluidic approach has established itself as one of the preferred techniques to produce high quality quantum dots in small quantities for commercial resale. Fast heating and mixing times due to the short channel dimensions present in microfluidic systems enable superior control over the reaction conditions, allowing for high tunability of nanoparticle size and morphology. To date microfluidics has been used successfully to synthesize a host of semiconductor nanoparticles, including CdSe[78,80,85-91], CdS[84,92-94]. Complex morphologies like core-shell structures were successfully synthesized for CdSe/ZnS[95-97], CdSe/ZnSe/ZnS[98], and ZnS/CdSe/ZnS[99]. High quantum yields in the range of 70 – 80% was achieved for CdSe/ZnS

particles by optimizing the temperature and residence times for shell-growth step[79,100]. Furthermore, tight control of temperature enabled continuous syntheses in which the nucleation and growth steps were temporally separated to yield monodisperse CdSe particles with FWHM as small as 29 nm[82]. However, only a limited number of studies has been reported on continuous synthesis of Cd-free particles – InP[101,102], ZnSe[103] dots, and ZnSe/ZnS[104] core-shell particles. Continuous flow reactors fall into two broad categories – capillary-based reactors and chip-based reactors. Capillary-based reactors comprise of simple capillaries in the size range of 100 – 1000 μm (**Figure 1.12a** and **1.11c**). These reactors are made from a variety of materials with glass and PTFE being the most commonly used ones. The reagents are flowed through the reactor at a desired flow rate using a syringe pump. The reactor is typically placed in hot oil-bath to attain the required temperature (**Figure 1.12a**). Due to a simple design, capillary-based reactors have been used by many research groups. The second type of microfluidic reactors uses a solid host or chip to house the channels. The typical size of these channels range between 100 – 1000 μm. The chips can be fabricated from a range of materials including silicon, glass, polymers (**Figure 1.11a-b** and **1.12b-c**). High temperatures in these reactors are typically achieved by using hot plates, heating blocks, or special localized heaters integrated on the reactor. Fast mixing and heating times in continuous reactors are the two distinct advantages over conventional batch synthesis techniques. Several methods have been used to achieve rapid mixing in continuous reactors including liquid-liquid[85,93,94,105-107] (**Figure 1.11a-b** and **1.12b-c**) and gas-liquid segmented flow reactors[98,108], convective micromixers[109] (**Figure 1.12a**), split and recombine mixing techniques, and different geometries[102] (serpentine channels, convoluted channels in 3-dimensions). Additionally, microfluidic reactors have expanded the achievable operating conditions beyond what was previously available on batch scale, for instance, Jensen *et al.* demonstrated enhanced mixing by operating in the supercritical regime of hexane that was used

as the solvent for CdSe synthesis in a pressurized microfluidic reactor[110-112]. Following this, similar works were published that employed pressurized reactors to operate in supercritical regime[81,113] (**Figure 1.12b**)\. Continuous flow reactors have been used to screen optimum operating conditions for quantum dot synthesis by utilizing inline analytical technique to obtain real-time information about the product, most commonly absorbance and fluorescence measurements[87,114]. Krishnadasan *et al.* demonstrated the application of a fully automated microfluidic reactor to optimize quantum yield of the synthesized CdSe particles of a desired wavelength[115].

1.4 Continuous flow synthesis: current challenges

Despite the high commercial value of semiconductor nanoparticles, not many attempts have been made to produce these particles at a high throughput on a continuous scale, whilst maintaining a high product quality. To date the majority of the literature on continuous-scale synthesis of quantum dots is based on microreactors, which are not considered a viable option for high-throughput synthesis. This perception is further corroborated by the literature where almost all the syntheses in microreactors, barring a few, have at best achieved a production of sub-gram per day. Recent work by De Mello *et al.* stands as the only example of a scale-out synthesis in which they applied five-way parallelization to their capillary-based reactor (made out of Teflon tubing) to synthesize CdSe quantum dots at a rate of 150 g/day[116]. Aside from the aforementioned work, there is no work in the literature to have demonstrated any example of scale-up or scale-out synthesis of quantum dots on a continuous scale (> 100 g/day) synthesis.

The commonly used solvents in microscale flow reactors include octadecene, hexane, squalene, trioctylphosphine, thereby ruling out the waxy long-chain ligands typically used in

batch syntheses[86]. Furthermore, narrow channels in the microreactors run into the risk of clogging caused by the precipitation of reagents or products if left unchecked. These factors impede the application of the continuous flow synthesis of anisotropic semiconductor nanocrystals. To date only one work on continuous synthesis of anisotropic semiconductor (both Cd-based and Cd-free) nanoparticles exists in the literature[77]. Additionally, most of these syntheses require inert conditions for all synthesis steps including precursor preparation, precursor transfer (to the reactor), and reaction. This makes implementation of such syntheses difficult in a continuous flow system. The majority of the conventional flow reactors use heating media such as oil or hot water, which limits the maximum temperature attained by these reactors. Use of oil baths also complicates scalability of such reactor setups.

To date the majority of the literature on continuous flow synthesis has been focused on Cd-based quantum dots; only a handful of studies on Cd-free quantum dots has been reported. Furthermore, none of the continuous-scale synthesis of Cd-free nanoparticles comes even close to Cd-based quantum dots in terms of performance. For instance, the highest quantum yield achieved for a Cd-free nanoparticle synthesized on a continuous scale is about 30 – 40%[117], which is far below the quantum yields (70 – 80%) achieved in the case of Cd-based quantum dots. In the wake of the recent regulations against the use of Cd in electronic appliances, novel continuous flow reactors that enable high throughput synthesis of high-quality Cd-free quantum dots have become all the more important if quantum dots are ever to make a transition from laboratories to consume products.

1.5 Project Goals

The work presented in this thesis focuses on the design, fabrication, and application of continuous flow platforms for the synthesis of novel semiconductor nanoparticles for potential

application in solid-state lighting and displays. Therefore, the main focus of this project is on (1) validation of the design by implementing model chemistry (CdSe/CdS/ZnS, CdSeS/ZnS) in the reactor setup (described in Chapter 2); (2) design and fabrication of a robust reactor setup that enables high temperature, air-sensitive syntheses (containing solid/viscos reactants) of nanoparticles (described in Chapter 3); (3) demonstration of the first instance of continuous synthesis of Cd-based and Cd-free anisotropic nanoparticles (described in Chapter 3); (4) demonstration of multistep continuous flow synthesis of highly luminescent Cd-free nanoparticles (InP/ZnSeS) that exhibit high quantum yield with the ability to tune the emission wavelength of these particles (Chapter 4). Also, as a side effort, we designed, fabricated, and characterized a millifluidic static mixer to enable fast mixing. The developed mixer was further used to synthesize gold nanoparticles with a good size-control, thereby demonstrating its fast mixing capabilities (Chapter 5)

1.6 Figures

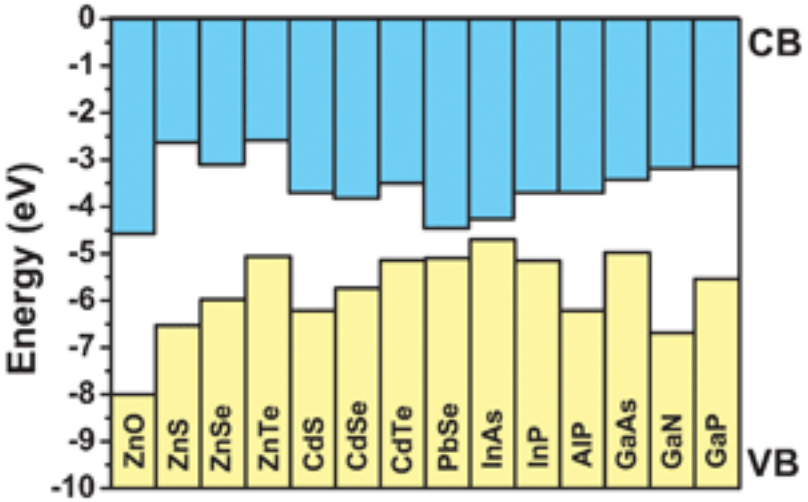

Figure 1.1. Plot showing electronic band edges for the conduction (blue) and valence bands of various bulk semiconductors relative the vacuum level. The band gap for each semiconductor is represented by the space between the solid bars. Bulk values are used for all the semiconductors, except for PbSe, whose values were estimated from nanocrystal results[118]. Reproduced with permission from The Royal Society of Chemistry[6].

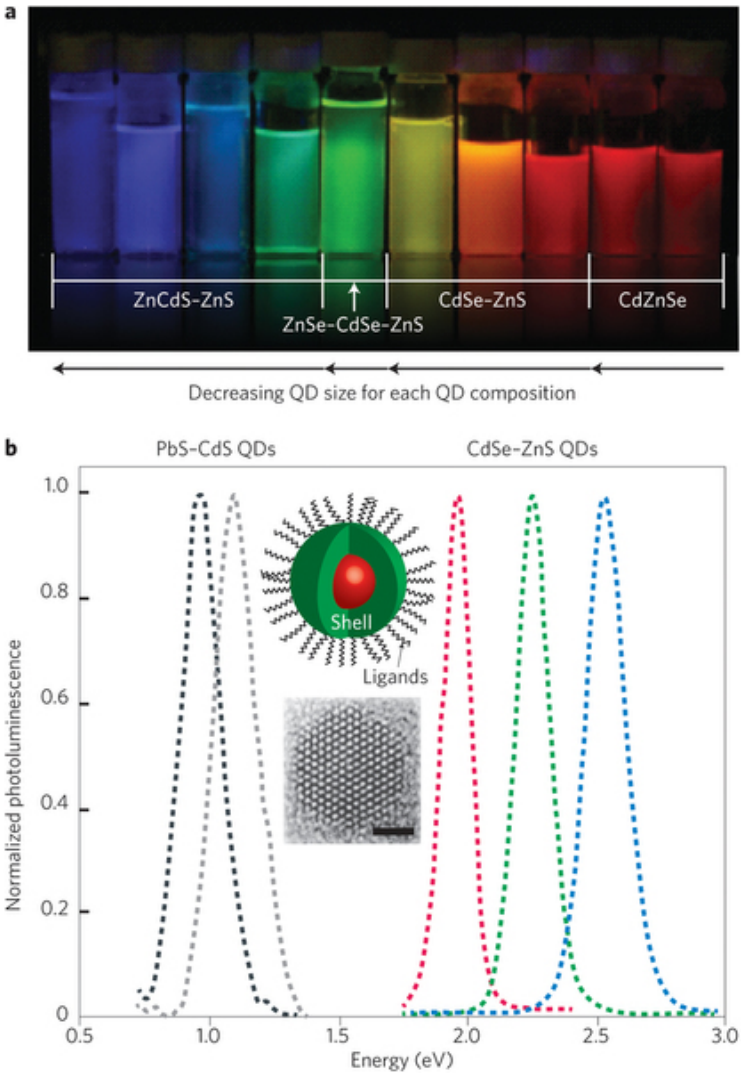

Figure 1.2. (a) Quantum dots (QDs) of varying size and composition illuminated under UV light[119]. **(b)** Photoluminescence spectra of CdSe/ZnS and PbS/CdS core–shell QDs. The upper inset shows a cartoon of a typical core–shell QD with capping ligands attached to the nanoparticle surface. The lower inset shows a high-resolution transmission electron microscope image of a CdSe QD (scale bar = 1.5 nm)[120]. Reprinted by permission from Macmillan Publishers Ltd: Nature Photonics[7], Copyright 2015.

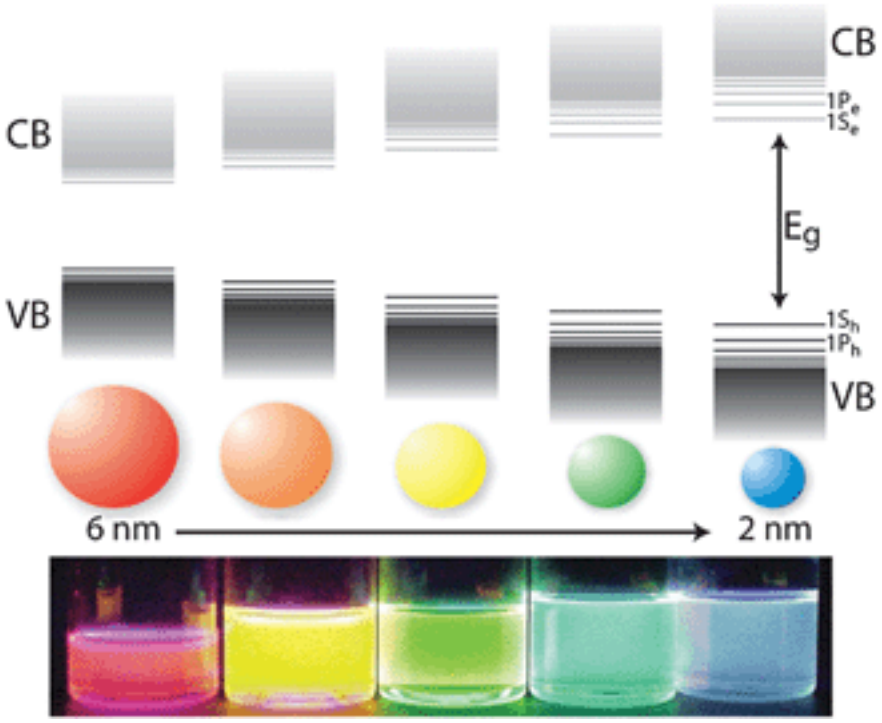

Figure 1.3. The upper inset shows a schematic representation of the quantum confinement effect on the energy levels of a semiconductor nanomaterial. The band gap (between the conduction and valence band) increases with a decrease in the size of the quantum confined nanomaterial. Additionally, the number of discrete energy states increases as the size of the QD decreases indicating an increase in the strength of the quantum confinement effect. The lower inset shows solutions of colloidal CdSe QDs illuminated under UV light. Courtesy of R. Koole (Philips Research Laboratories, The Netherlands). Reproduced with permission from The Royal Society of Chemistry[6].

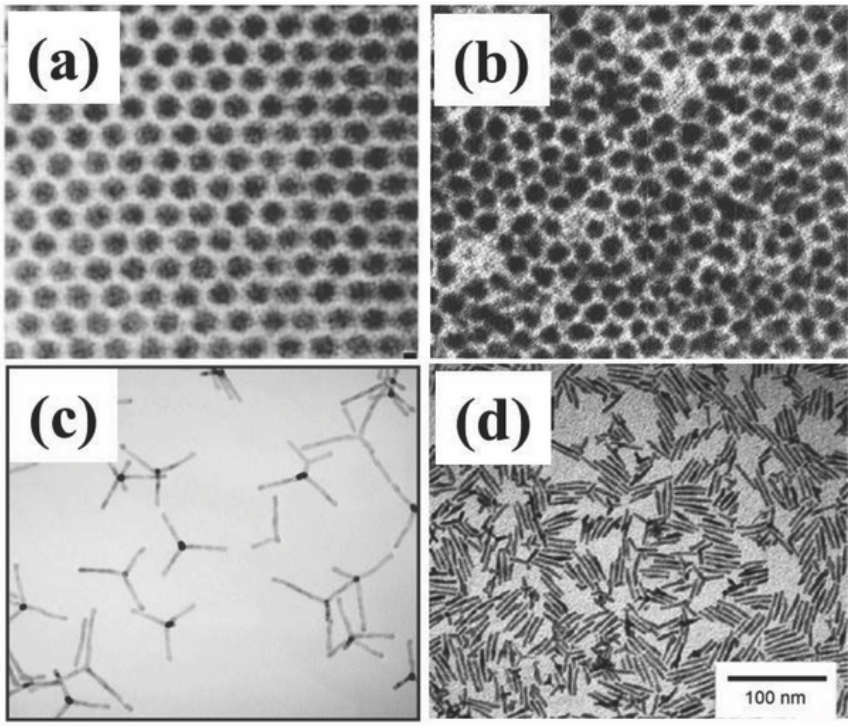

Figure 1.4. Quantum confined nanomaterials exist in different morphologies - **(a)** TEM image of monodisperse CdSe QDs that are roughly 4.8 nm in diameter[2], **(b)** TEM image of CdSe/ZnS core/shell QDs[121], **(c)** TEM image of CdTe tetrapods[122], **(d)** Anisotropic growth enabled by kinetic shape control and selective adhesion results in the formation of nanorods (TEM)[123]. Reproduced with permission[1].

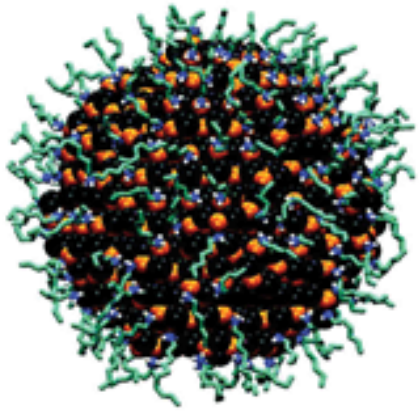

Figure 1.5. Cartoon of a CdSe QDs with capping ligands attached to its surface. The image was obtained via a molecular simulation. Hexylamine molecules are the capping ligands in this case. Colour coding: black, Se; orange, Cd; light blue, C; dark blue, N; white, H; yellow, S; brown, P; red, O[124]. Reproduced with permission The Royal Society of Chemistry[6].

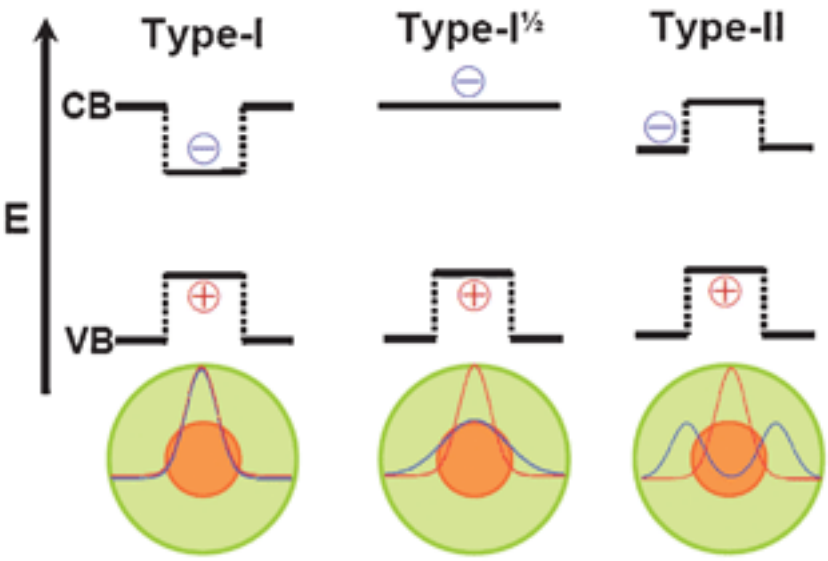

Figure 1.6. The upper inset shows a schematic representation of the three basic types of Heteroanocrystals (HNCs) based on the localization of the charge carriers. The conduction and valence band edges are indicated by CB and VB, respectively. The plus and minus signs represent holes and electrons, respectively. The lower inset depicts the electron and hole ground-state wave functions for the three types of HNCs that are represented as core-shell structures here. Courtesy of M. Vis and A. G. M. Brinkman (Utrecht University, The Netherlands). Reproduced with permission The Royal Society of Chemistry[6].

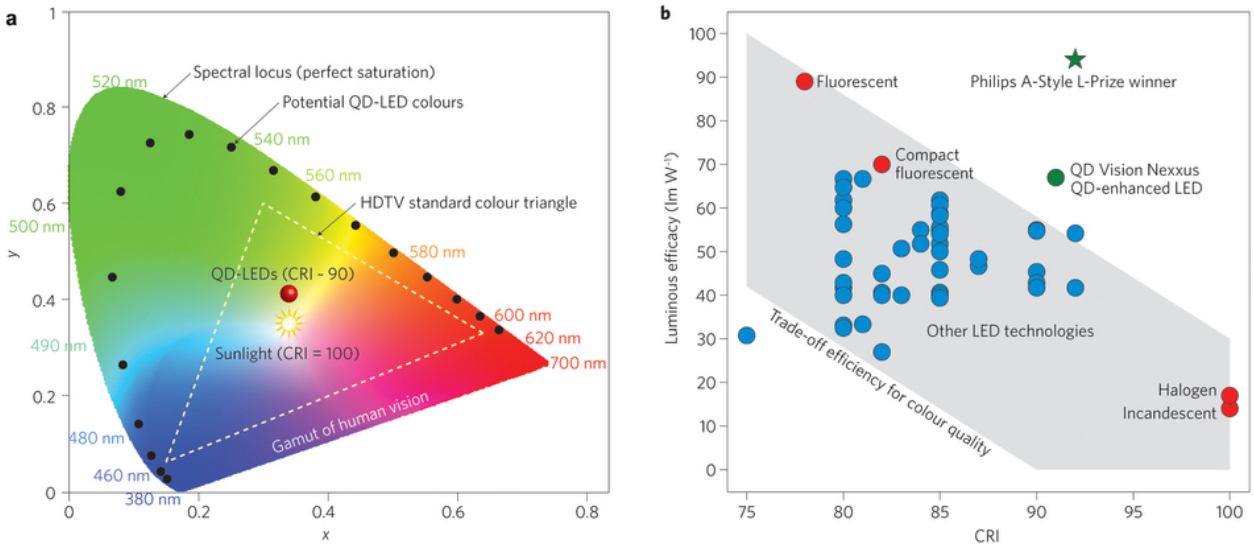

Figure 1.7. (a) CIE chromaticity comparing the color gamut attained by QDs (dotted line) and commercially available standard high-definition television (dashed line). The plot indicates that the QDs enable a higher color gamut compared to a standard high-definition TV. **(b)** Plot showing the luminous efficacy and Color Rendering Index of various commercial lighting products. The first commercial QD-based Solid State Light source, developed by QD Vision and Nexxus Lighting, demonstrated high CRI and luminescence efficacy. In general, a recent surge in the number of products using QDs indicate an emerging big market in terms of the application of QDs for lighting, displays, and downconverters. Reprinted by permission from Macmillan Publishers Ltd: Nature Photonics[7], Copyright 2015.

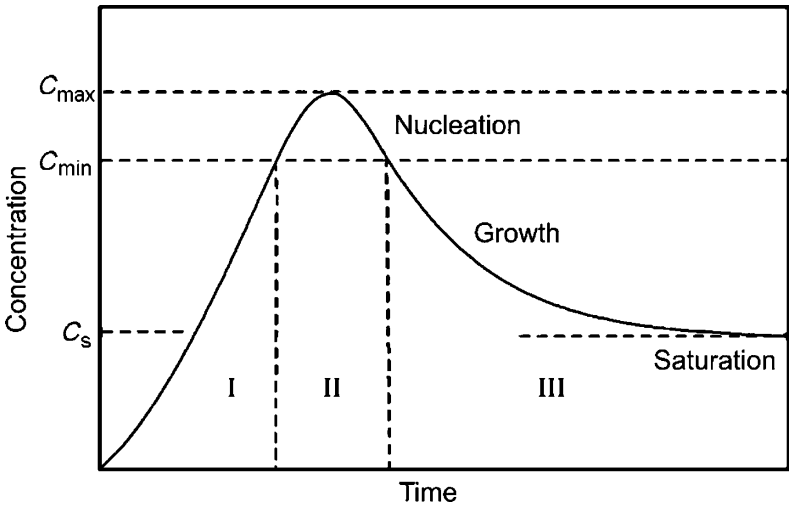

Figure 1.8. Schematic representation of LaMer and Dinegar's model that depicts various stages of a crystal formation (modified reproduction of the **Figure** used in the original work of LaMer *et al.*[37]). **Figure** reprinted with permission from Bahrig *et al.*[125]

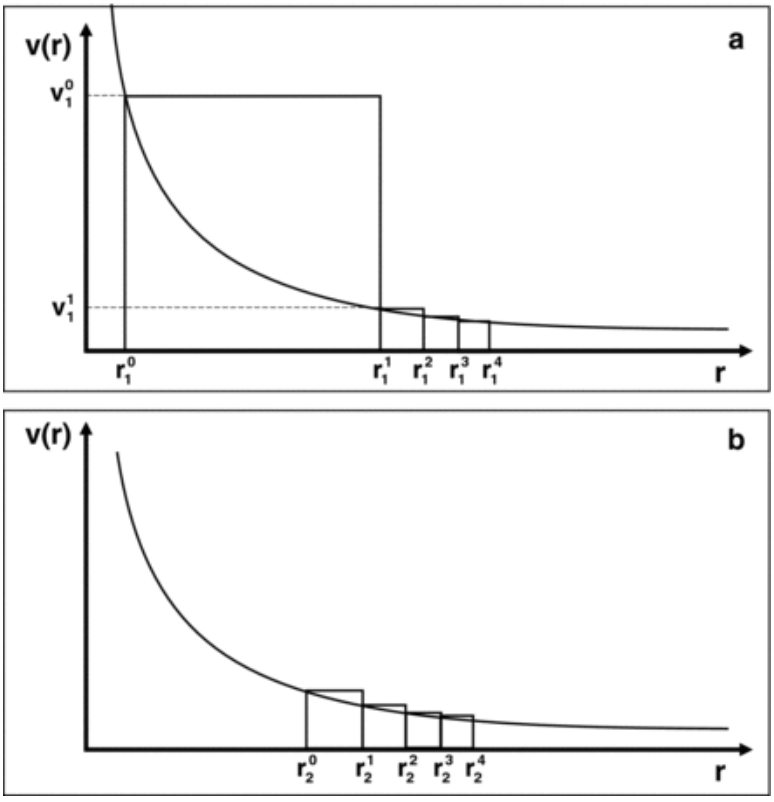

Figure 1.9. Plots illustrating the growth of Particles 1 **(a)** and 2 **(b)**. The terms v(r) and r indicate the growth rate and the particle radius respectively. r_1^n and r_2^n are the radii of particles 1 and 2 at n^{th} time. Reproduced (figure and caption) with permission[126].

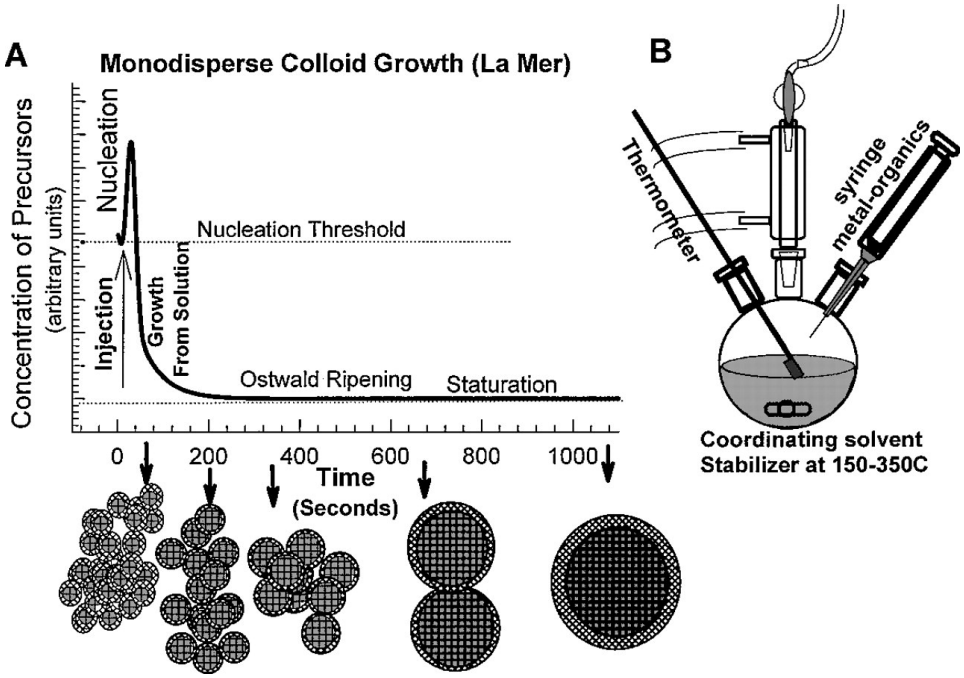

Figure 1.10. (a) The upper inset consists of a plot showing the various stages of nanocrystal formation via hot-injection synthesis technique. The bottom inset shows the relative size and number of the nanoparticles corresponding to the different stages of the hot-injection synthesis technique. **(b)** Schematic representation of a typical synthetic apparatus employed to produce monodisperse colloidal nanocrystals via hot-injection synthesis technique. Reproduced with permission[2].

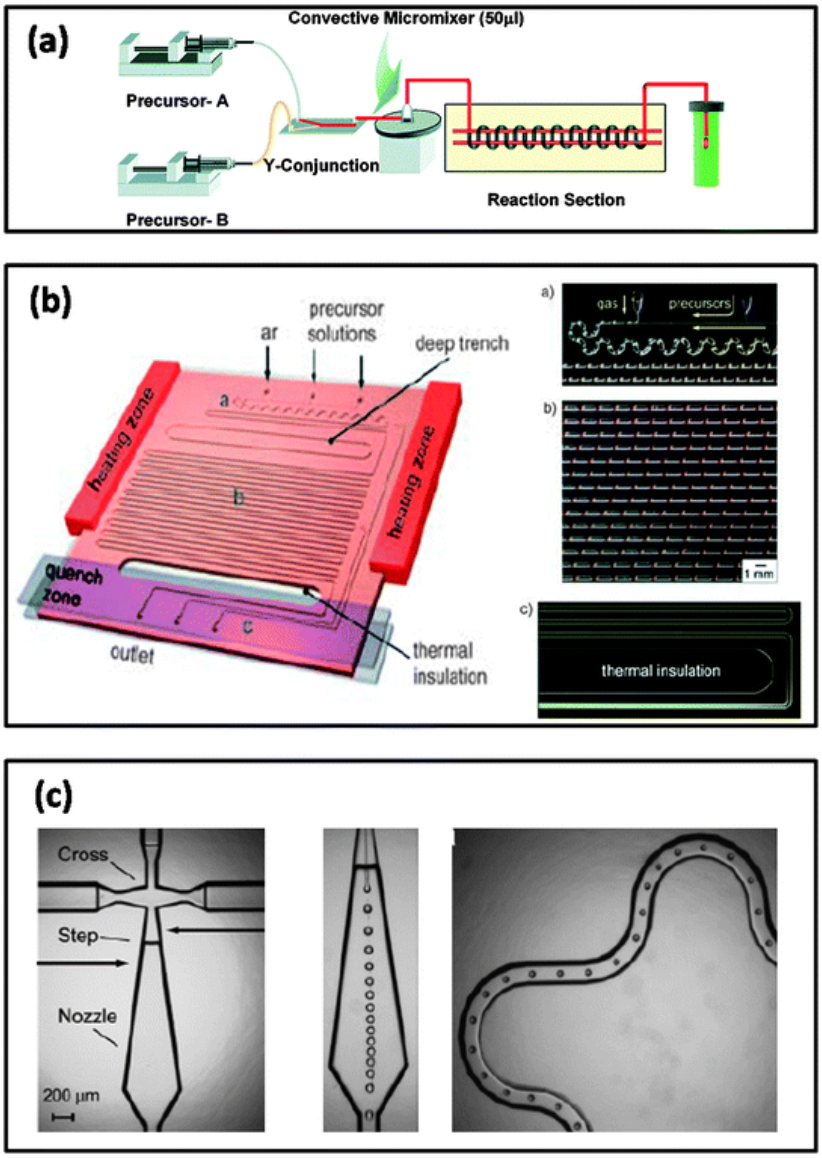

Figure 1.11. Examples of various microfluidic flow reactors that enable high temperature synthesis of QDs. **(a)** Simple silica capillary tube based flow reactor that employs an oil bath to attain high temperatures for QD synthesis[80], **(b)** A gas–liquid flow reactor made out of Silicon and Pyrex microreactor for the segmented synthesis of CdSe QDs with on chip mixing, ageing and quenching zone[108]. **(c)** Pyrex-based microreactor that employs liquid–liquid (ODE–Fomblin) droplet-based system for the synthesis of CdSe QDs[106]. Reproduced with permission of The Royal Society of Chemistry[127].

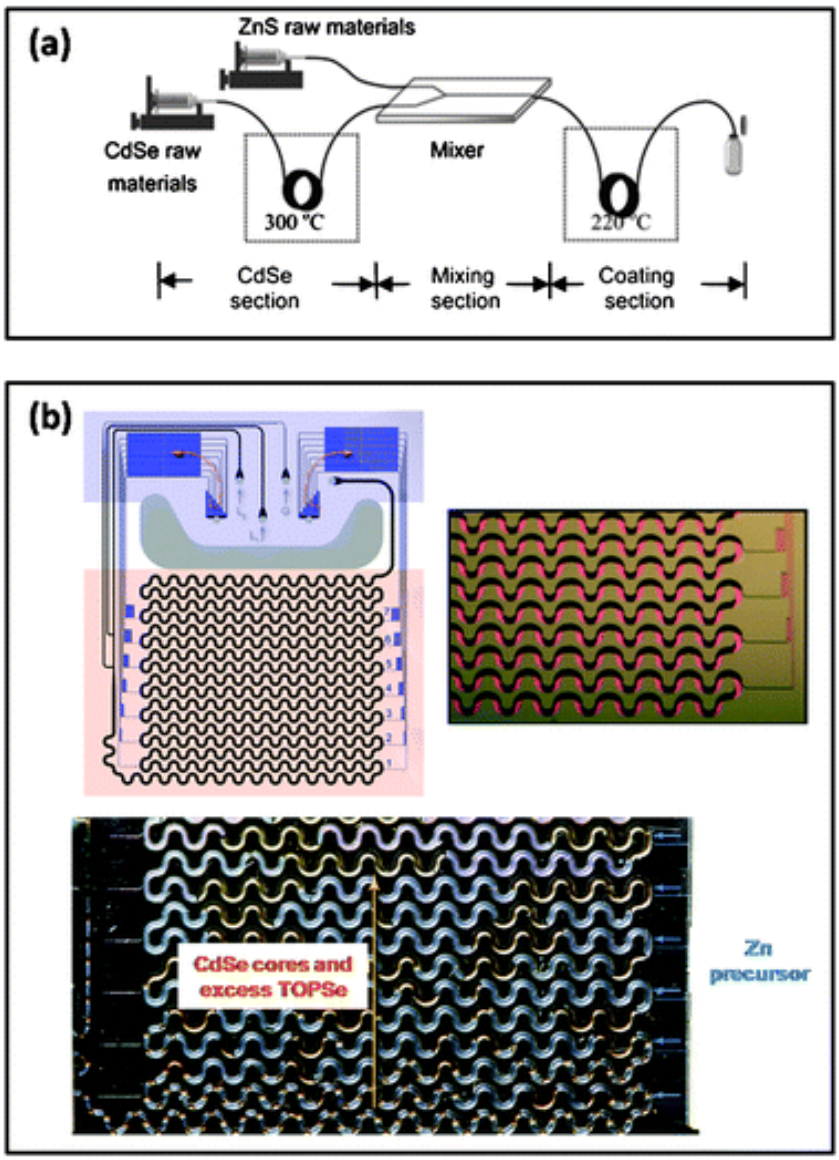

Figure 1.12. Examples of microfluidic flow reactors that enable high temperature on-ship synthesis of core–shell QDs. **(a)** A multistep flow microreactor based on silica capillary tubing. The first stage enables CdSe cores synthesis followed by on-chip mixing and a second reaction stage for the growth of ZnS shell over synthesized CdSe cores[95]. **(b)** Silicon–Pyrex microreactor equipped with two temperature zones for multistep synthesis of CdSe/ZnSe core-shell QDs. Reproduced with permission of The Royal Society of Chemistry[127].

1.6 References

1 Kim, J. Y., Voznyy, O., Zhitomirsky, D. & Sargent, E. H. 25th Anniversary Article: Colloidal Quantum Dot Materials and Devices: A Quarter-Century of Advances. *Advanced materials* **25**, 4986-5010, doi:10.1002/adma.201301947 (2013).

2 Murray, C. B., Kagan, C. R. & Bawendi, M. G. Synthesis and characterization of monodisperse nanocrystals and close-packed nanocrystal assemblies. *Annu Rev Mater Sci* **30**, 545-610, doi:DOI 10.1146/annurev.matsci.30.1.545 (2000).

3 Klimov, V. I. Nanocrystal quantum dots. CRC Press, Boca Raton, 2010.

4 Martienssen, W., Warlimont, H. Springer handbook of condensed matter and materials data Springer. Heidelberg ; New York, 2005.

5 De Mello Donegá, C. Nanoparticles: Workhorses of nanosciences. Springer Berlin Heidelberg, S.l., 2014.

6 Donega, C. D. Synthesis and properties of colloidal heteronanocrystals. *Chemical Society reviews* **40**, 1512-1546, doi:10.1039/c0cs00055h (2011).

7 Shirasaki, Y., Supran, G. J., Bawendi, M. G. & Bulovic, V. Emergence of colloidal quantum-dot light-emitting technologies. *Nat Photonics* **7**, 13-23, doi:10.1038/Nphoton.2013.328 (2013).

8 D'Andrea, A. *Optics of excitons in confined systems : proceedings of the international meeting, Giardini Naxos, Italy, 24-27 September 1991*. (Institute of Physics, 1992).

9 Uozumi, T. & Kayanuma, Y. Excited states of an electron-hole pair in spherical quantum dots and their optical properties. *Phys Rev B* **65**, doi:ARTN 16531810.1103/PhysRevB.65.165318 (2002).

10 Martienssen, W. & Warlimont, H. (Springer,, Heidelberg ; New York, 2005).

11 Yang, C. C. & Li, S. Size, dimensionality, and constituent stoichiometry dependence of bandgap energies in semiconductor quantum dots and wires. *J Phys Chem C* **112**, 2851-2856, doi:10.1021/jp076694g (2008).

12 Yu, H., Li, J. B., Loomis, R. A., Wang, L. W. & Buhro, W. E. Two- versus three-dimensional quantum confinement in indium phosphide wires and dots. *Nature materials* **2**, 517-520, doi:10.1038/nmat942 (2003).

13 Talapin, D. V., Rogach, A. L., Kornowski, A., Haase, M. & Weller, H. Highly luminescent monodisperse CdSe and CdSe/ZnS nanocrystals synthesized in a hexadecylamine-trioctylphosphine oxide-trioctylphospine mixture. *Nano Lett* **1**, 207-211, doi:10.1021/nl0155126 (2001).

14 McDaniel, H., Zuo, J. M. & Shim, M. Anisotropic Strain-Induced Curvature in Type-II CdSe/CdTe Nanorod Heterostructures. *J Am Chem Soc* **132**, 3286-+, doi:10.1021/ja910233a (2010).

15 Mews, A., Eychmuller, A., Giersig, M., Schooss, D. & Weller, H. Preparation, Characterization, and Photophysics of the Quantum-Dot Quantum-Well System Cds/Hgs/Cds. *J Phys Chem-Us* **98**, 934-941, doi:DOI 10.1021/j100054a032 (1994).

16 Colvin, V. L., Schlamp, M. C. & Alivisatos, A. P. Light-Emitting-Diodes Made from Cadmium Selenide Nanocrystals and a Semiconducting Polymer. *Nature* **370**, 354-357, doi:DOI 10.1038/370354a0 (1994).

17 Coe, S., Woo, W. K., Bawendi, M. & Bulovic, V. Electroluminescence from single monolayers of nanocrystals in molecular organic devices. *Nature* **420**, 800-803, doi:10.1038/nature01217 (2002).

18 Mueller, A. H. *et al.* Multicolor light-emitting diodes based on semiconductor nanocrystals encapsulated in GaN charge injection layers. *Nano Lett* **5**, 1039-1044, doi:10.1021/nl050384x (2005).

19 Stouwdam, J. W. & Janssen, R. A. J. Red, green, and blue quantum dot LEDs with solution processable ZnO nanocrystal electron injection layers. *Journal of Materials Chemistry* **18**, 1889-1894, doi:10.1039/b800028j (2008).

20 Klimov, V. I. *et al.* Single-exciton optical gain in semiconductor nanocrystals. *Nature* **447**, 441-446, doi:10.1038/nature05839 (2007).

21 Bae, W. K. *et al.* R/G/B/Natural White Light Thin Colloidal Quantum Dot-Based Light-Emitting Devices. *Advanced materials* **26**, 6387-6393, doi:10.1002/adma.201400139 (2014).

22 Bae, W. K. & Lee, S. H. Colloidal quantum dot-based thin flexible light-emitting devices. *Abstr Pap Am Chem S* **248** (2014).

23 Konstantatos, G. *et al.* Ultrasensitive solution-cast quantum dot photodetectors. *Nature* **442**, 180-183, doi:10.1038/nature04855 (2006).

24 Huang, L. D., Tu, C. C. & Lin, L. Y. Colloidal quantum dot photodetectors enhanced by self-assembled plasmonic nanoparticles. *Applied Physics Letters* **98**, doi:Artn 11311010.1063/1.3567514 (2011).

25 Keuleyan, S., Lhuillier, E., Brajuskovic, V. & Guyot-Sionnest, P. Mid-infrared HgTe colloidal quantum dot photodetectors. *Nat Photonics* **5**, 489-493, doi:10.1038/Nphoton.2011.142 (2011).

26 Kairdolf, B. A. *et al.* Semiconductor Quantum Dots for Bioimaging and Biodiagnostic Applications. *Annu Rev Anal Chem* **6**, 143-162, doi:10.1146/annurev-anchem-060908-155136 (2013).

27 Alivisatos, P. The use of nanocrystals in biological detection. *Nat Biotechnol* **22**, 47-52, doi:10.1038/nbt927 (2004).

28 Michalet, X. *et al.* Quantum dots for live cells, in vivo imaging, and diagnostics. *Science* **307**, 538-544, doi:10.1126/science.1104274 (2005).

29 Medintz, I. L., Uyeda, H. T., Goldman, E. R. & Mattoussi, H. Quantum dot bioconjugates for imaging, labelling and sensing. *Nature materials* **4**, 435-446, doi:10.1038/nmat1390 (2005).

30 Goldman, E. R. *et al.* Self-assembled luminescent CdSe-ZnS quantum dot bioconjugates prepared using engineered poly-histidine terminated proteins. *Analytica Chimica Acta* **534**, 63-67, doi:10.1016/j.aca.2004.03.079 (2005).

31 Baker, M. Nanotechnology imaging probes: smaller and more stable. *Nature methods* **7**, 957-962, doi:10.1038/nmeth1210-957 (2010).

32 Luther, J. M. *et al.* Stability assessment on a 3% bilayer PbS/ZnO quantum dot heterojunction solar cell. *Advanced materials* **22**, 3704-3707, doi:10.1002/adma.201001148 (2010).

33 Willis, S. M., Cheng, C., Assender, H. E. & Watt, A. A. R. The Transitional Heterojunction Behavior of PbS/ZnO Colloidal Quantum Dot Solar Cells. *Nano Lett* **12**, 1522-1526, doi:10.1021/nl204323j (2012).

34 Kim, S. *et al.* Air-Stable and Efficient PbSe Quantum-Dot Solar Cells Based upon ZnSe to PbSe Cation-Exchanged Quantum Dots. *Acs Nano* **9**, 8157-8164, doi:10.1021/acsnano.5b02326 (2015).

35 Zhang, J. B. *et al.* PbSe Quantum Dot Solar Cells with More than 6% Efficiency Fabricated in Ambient Atmosphere. *Nano Lett* **14**, 6010-6015, doi:10.1021/nl503085v (2014).

36 Zhang, J. B., Gao, J. B., Miller, E. M., Luther, J. M. & Beard, M. C. Diffusion-Controlled Synthesis of PbS and PbSe Quantum Dots with in Situ Halide Passivation for Quantum Dot Solar Cells. *Acs Nano* **8**, 614-622, doi:10.1021/nn405236k (2014).

37 Lamer, V. K. & Dinegar, R. H. Theory, Production and Mechanism of Formation of Monodispersed Hydrosols. *J Am Chem Soc* **72**, 4847-4854, doi:DOI 10.1021/ja01167a001 (1950).

38 Klabunde, K. J., Erickson, L., Koper, O. & Richards, R. Review of Nanoscale Materials in Chemistry: Environmental Applications. *Acs Sym Ser* **1045**, 1-13 (2010).

39 Peng, X. G., Wickham, J. & Alivisatos, A. P. Kinetics of II-VI and III-V colloidal semiconductor nanocrystal growth: "Focusing" of size distributions. *J Am Chem Soc* **120**, 5343-5344, doi:DOI 10.1021/ja9805425 (1998).

40 Sugimoto, T. Preparation of Monodispersed Colloidal Particles. *Adv Colloid Interfac* **28**, 65-108, doi:Doi 10.1016/0001-8686(87)80009-X (1987).

41 De Smet, Y., Deriemaeker, L. & Finsy, R. A simple computer simulation of Ostwald ripening. *Langmuir : the ACS journal of surfaces and colloids* **13**, 6884-6888, doi:DOI 10.1021/la970379b (1997).

42 DeSmet, Y., Malfait, J., DeVos, C., Deriemaeker, L. & Finsy, R. Ostwald ripening of concentrated alkane emulsions: a comparison of fiber-optics dynamic light scattering and conventional dynamic light scattering. *Prog Coll Pol Sci S* **105**, 252-255 (1997).

43 Gratz, H. A time constant for Ostwald ripening of precipitates and normal grain growth. *J Mater Sci Lett* **18**, 1637-1639, doi:Doi 10.1023/A:1006601026899 (1999).

44 Gratz, H. Ostwald ripening: New relations between particle growth and particle size distribution. *Scripta Mater* **37**, 9-16, doi:Doi 10.1016/S1359-6462(97)00068-7 (1997).

45 Weller, H. *et al.* Photochemistry of Semiconductor Colloids .14. Photochemistry of Colloidal Semiconductors - Onset of Light-Absorption as a Function of Size of Extremely Small Cds Particles. *Chem Phys Lett* **124**, 557-560, doi:Doi 10.1016/0009-2614(86)85075-8 (1986).

46 Spanhel, L., Haase, M., Weller, H. & Henglein, A. Photochemistry of Colloidal Semiconductors .20. Surface Modification and Stability of Strong Luminescing Cds Particles. *J Am Chem Soc* **109**, 5649-5655, doi:DOI 10.1021/ja00253a015 (1987).

47 Henglein, A. Small-Particle Research - Physicochemical Properties of Extremely Small Colloidal Metal and Semiconductor Particles. *Chemical reviews* **89**, 1861-1873, doi:DOI 10.1021/cr00098a010 (1989).

48 Brus, L. Electronic Wave-Functions in Semiconductor Clusters - Experiment and Theory. *J Phys Chem-Us* **90**, 2555-2560, doi:DOI 10.1021/j100403a003 (1986).

49 Brus, L. E. Electron Electron and Electron-Hole Interactions in Small Semiconductor Crystallites - the Size Dependence of the Lowest Excited Electronic State. *J Chem Phys* **80**, 4403-4409, doi:Doi 10.1063/1.447218 (1984).

50 Murray, C. B., Norris, D. J. & Bawendi, M. G. Synthesis and Characterization of Nearly Monodisperse Cde (E = S, Se, Te) Semiconductor Nanocrystallites. *J Am Chem Soc* **115**, 8706-8715, doi:DOI 10.1021/ja00072a025 (1993).

51 Steckel, J. S. *et al.* Blue luminescence from (CdS)ZnS core-shell nanocrystals. *Angew Chem Int Edit* **43**, 2154-2158, doi:10.1002/anie.200453728 (2004).

52 Sharma, S. N. *et al.* Single pot synthesis of composition tunable CdSe-ZnSe (core-shell) and ZnxCd1-xSe (ternary alloy) nanocrystals with high luminescence and stability. *Mater Res Innov* **14**, 62-67, doi:10.1179/143307510x12599329343286 (2010).

53 Zhong, X. H., Han, M. Y., Dong, Z. L., White, T. J. & Knoll, W. Composition-tunable ZnxCd1-xSe nanocrystals with high luminescence and stability. *J Am Chem Soc* **125**, 8589-8594, doi:10.1021/ja035096m (2003).

54 Bailey, R. E. & Nie, S. M. Alloyed semiconductor quantum dots: Tuning the optical properties without changing the particle size. *J Am Chem Soc* **125**, 7100-7106, doi:10.1021/ja035000o (2003).

55 Talapin, D. V. *et al.* A novel organometallic synthesis of highly luminescent CdTe nanocrystals. *J Phys Chem B* **105**, 2260-2263, doi:DOI 10.1021/jp003177o (2001).

56 Ahrenkiel, S. P. *et al.* Synthesis and characterization of colloidal InP quantum rods. *Nano Lett* **3**, 833-837, doi:10.1021/nl034152e (2003).

57 Nedeljkovic, J. M., Micic, O. I., Ahrenkiel, S. P., Miedaner, A. & Nozik, A. J. Synthesis and characterization of colloidal InP quantum rods and dots. *Abstr Pap Am Chem S* **225**, U510-U510 (2003).

58 Talapin, D. V. *et al.* Etching of colloidal InP nanocrystals with fluorides: Photochemical nature of the process resulting in high photoluminescence efficiency. *J Phys Chem B* **106**, 12659-12663, doi:10.1021/jp026380n (2002).

59 Cao, Y. W. & Banin, U. Growth and properties of semiconductor core/shell nanocrystals with InAs cores. *J Am Chem Soc* **122**, 9692-9702 (2000).

60 Hines, M. A. & Guyot-Sionnest, P. Bright UV-blue luminescent colloidal ZnSe nanocrystals. *J Phys Chem B* **102**, 3655-3657, doi:DOI 10.1021/jp9810217 (1998).

61 Shim, M. & Guyot-Sionnest, P. Organic-capped ZnO nanocrystals: Synthesis and n-type character. *J Am Chem Soc* **123**, 11651-11654, doi:10.1021/ja0163321 (2001).

62 Hines, M. A. & Scholes, G. D. Colloidal PbS nanocrystals with size-tunable near-infrared emission: Observation of post-synthesis self-narrowing of the particle size distribution. *Advanced materials* **15**, 1844-1849, doi:10.1002/adma.200305395 (2003).

63 Murray, C. B. *et al.* Colloidal synthesis of nanocrystals and nanocrystal superlattices. *Ibm J Res Dev* **45**, 47-56 (2001).

64 Wehrenberg, B. L., Wang, C. J. & Guyot-Sionnest, P. Interband and intraband optical studies of PbSe colloidal quantum dots. *J Phys Chem B* **106**, 10634-10640, doi:10.1021/jp021187e (2002).

65 Lifshitz, E. *et al.* Synthesis and characterization of PbSe quantum wires, multipods, quantum rods,and cubes. *Nano Lett* **3**, 857-862, doi:10.1021/nl0342085 (2003).

66 Lu, W. G., Fang, J. Y., Stokes, K. L. & Lin, J. Shape evolution and self assembly of monodisperse PbTe nanocrystals. *J Am Chem Soc* **126**, 11798-11799, doi:10.1021/ja0469131 (2004).

67 Sun, S. H., Murray, C. B., Weller, D., Folks, L. & Moser, A. Monodisperse FePt nanoparticles and ferromagnetic FePt nanocrystal superlattices. *Science* **287**, 1989-1992, doi:DOI 10.1126/science.287.5460.1989 (2000).

68 Sun, S. H. & Zeng, H. Size-controlled synthesis of magnetite nanoparticles. *J Am Chem Soc* **124**, 8204-8205, doi:10.1021/ja026501x (2002).

69 Yang, Y. A., Wu, H. M., Williams, K. R. & Cao, Y. C. Synthesis of CdSe and CdTe nanocrystals without precursor injection. *Angew Chem Int Edit* **44**, 6712-6715, doi:10.1002/anie.200502279 (2005).

70 Li, L. & Reiss, P. One-pot synthesis of highly luminescent InP/ZnS nanocrystals without precursor injection. *J Am Chem Soc* **130**, 11588-+, doi:Doi 10.1021/Ja803687e (2008).

71 Jana, N. R., Chen, Y. F. & Peng, X. G. Size- and shape-controlled magnetic (Cr, Mn, Fe, Co, Ni) oxide nanocrystals via a simple and general approach. *Chemistry of Materials* **16**, 3931-3935, doi:10.1021/cm049221k (2004).

72 Chen, Y. F., Johnson, E. & Peng, X. G. Formation of monodisperse and shape-controlled MnO nanocrystals in non-injection synthesis: Self-focusing via. *J Am Chem Soc* **129**, 10937-10947, doi:DOI 10.1021/ja073023n (2007).

73 Si, R., Zhang, Y. W., You, L. P. & Yan, C. H. Rare-earth oxide nanopolyhedra, nanoplates, and nanodisks. *Angew Chem Int Edit* **44**, 3256-3260, doi:10.1002/anie.200462573 (2005).

74 Yu, T. Y., Joo, J., Park, Y. I. & Hyeon, T. Large-scale nonhydrolytic sol-gel synthesis of uniform-sized ceria nanocrystals with spherical, wire, and tadpole shapes. *Angew Chem Int Edit* **44**, 7411-7414, doi:10.1002/anie.200500992 (2005).

75 Cao, Y. C. Synthesis of square gadolinium-oxide nanoplates. *J Am Chem Soc* **126**, 7456-7457, doi:10.1021/ja0481676 (2004).

76 Phillips, T. W., Lignos, I. G., Maceiczyk, R. M., deMello, A. J. & deMello, J. C. Nanocrystal synthesis in microfluidic reactors: where next? *Lab on a chip* **14**, 3172-3180, doi:10.1039/c4lc00429a (2014).

77 Nightingale, A. M. & de Mello, J. C. Microscale synthesis of quantum dots. *Journal of Materials Chemistry* **20**, 8454, doi:10.1039/c0jm01221a (2010).

78 Yang, H., Luan, W., Tu, S.-t. & Wang, Z. M. High-Temperature Synthesis of CdSe Nanocrystals in a Serpentine Microchannel: Wide Size Tunability Achieved under a Short Residence Time. *Crystal Growth & Design* **9**, 1569-1574, doi:10.1021/cg800425f (2009).

79 Yang, H. *et al.* Continuous Synthesis of Full-Color Emitting Core/Shell Quantum Dots via Microreaction. *Crystal Growth & Design* **9**, 4807-4813, doi:10.1021/cg900652y (2009).

80 Yang, H. W., Luan, W. L., Tu, S. T. & Wang, Z. M. High-Temperature Synthesis of CdSe Nanocrystals in a Serpentine Microchannel: Wide Size Tunability Achieved under a Short Residence Time. *Crystal Growth & Design* **9**, 1569-1574, doi:Doi 10.1021/Cg800425f (2009).

81 Baek, J., Allen, P. M., Bawendi, M. G. & Jensen, K. F. Investigation of indium phosphide nanocrystal synthesis using a high-temperature and high-pressure continuous flow microreactor. *Angewandte Chemie* **50**, 627-630, doi:10.1002/anie.201006412 (2011).

82 Yang, H., Luan, W., Tu, S. T. & Wang, Z. M. Synthesis of nanocrystals via microreaction with temperature gradient: towards separation of nucleation and growth. *Lab on a chip* **8**, 451-455, doi:10.1039/b715540a (2008).

83 Xie, L. S., Harris, D. K., Bawendi, M. G. & Jensen, K. F. Effect of Trace Water on the Growth of Indium Phosphide Quantum Dots. *Chemistry of Materials* **27**, 5058-5063, doi:10.1021/acs.chemmater.5b01626 (2015).

84 Edel, J. B., Fortt, R., deMello, J. C. & deMello, A. J. Microfluidic routes to the controlled production of nanoparticles. *Chemical communications*, 1136-1137, doi:Doi 10.1039/B202998g (2002).

85 Chan, E. M., Mathies, R. A. & Alivisatos, A. P. Size-controlled growth of CdSe nanocrystals in microfluidic reactors. *Nano Lett* **3**, 199-201, doi:Doi 10.1021/Nl0259481 (2003).

86 Yen, B. K. H., Stott, N. E., Jensen, K. F. & Bawendi, M. G. A continuous-flow microcapillary reactor for the preparation of a size series of CdSe nanocrystals. *Advanced materials* **15**, 1858-1862, doi:Doi 10.1002/Adma.200305162 (2003).

87 Krishnadasan, S., Tovilla, J., Vilar, R., deMello, A. J. & deMello, J. C. On-line analysis of CdSe nanoparticle formation in a continuous flow chip-based microreactor. *Journal of Materials Chemistry* **14**, 2655-2660, doi:Doi 10.1039/B401559b (2004).

88 Nakamura, H. *et al.* Application of a microfluidic reaction system for CdSe nanocrystal preparation: their growth kinetics and photoluminescence analysis. *Lab on a chip* **4**, 237-240, doi:Doi 10.1039/B310915a (2004).

89 Luan, W., Yang, H., Tu, S.-t. & Wang, Z. Open-to-air synthesis of monodisperse CdSe nanocrystals via microfluidic reaction and its kinetics. *Nanotechnology* **18**, 175603, doi:10.1088/0957-4484/18/17/175603 (2007).

90 Wan, Z., Yang, H. W., Luan, W. L., Tu, S. T. & Zhou, X. G. Facile Synthesis of Monodisperse CdS Nanocrystals via Microreaction. *Nanoscale Research Letters* **5**, 130-137, doi:Doi 10.1007/S11671-009-9454-Z (2010).

91 Marre, S. *et al.* Supercritical Continuous-Microflow Synthesis of Narrow Size Distribution Quantum Dots. *Advanced materials* **20**, 4830-+, doi:Doi 10.1002/Adma.200801579 (2008).

92 Gomez-de Pedro, S. *et al.* A ceramic microreactor for the synthesis of water soluble CdS and CdS/ZnS nanocrystals with on-line optical characterization. *Nanoscale* **4**, 1328-1335, doi:10.1039/c2nr11525e (2012).

93 Shestopalov, I., Tice, J. D. & Ismagilov, R. F. Multi-step synthesis of nanoparticles performed on millisecond time scale in a microfluidic droplet-based system. *Lab on a chip* **4**, 316-321, doi:Doi 10.1039/B403378g (2004).

94 Hung, L. H. *et al.* Alternating droplet generation and controlled dynamic droplet fusion in microfluidic device for CdS nanoparticle synthesis. *Lab on a chip* **6**, 174-178, doi:Doi 10.1039/B513908b (2006).

95 Wang, H. *et al.* Continuous synthesis of CdSe-ZnS composite nanoparticles in a microfluidic reactor. *Chemical communications*, 48-49, doi:10.1039/b310644f (2004).

96 Wang, H. Z. *et al.* Highly luminescent CdSe/ZnS nanocrystals synthesized using a single-molecular ZnS source in a microfluidic reactor. *Advanced Functional Materials* **15**, 603-608, doi:Doi 10.1002/Adfm.200400164 (2005).

97 Kikkeri, R., Laurino, P., Odedra, A. & Seeberger, P. H. Synthesis of Carbohydrate-Functionalized Quantum Dots in Microreactors. *Angew Chem Int Edit* **49**, 2054-2057, doi:Doi 10.1002/Anie.200905053 (2010).

98 Lee, C. G., Uehara, M., Nakamura, H. & Maeda, H. High Temperature Preparation of Core and Core/Shell Composite Nanocrystals in a Multiphase Microreactor. *J Chem Eng Jpn* **41**, 644-648, doi:Doi 10.1252/Jcej.07we116 (2008).

99 Uehara, M., Nakamura, H. & Maeda, H. Preparation of ZnS/CdSe/ZnS Quantum Dot Quantum Well by Using a Microfluidic Reactor. *J Nanosci Nanotechno* **9**, 577-583, doi:10.1166/jnn.2009.J050 (2009).

100 Luan, W., Yang, H., Fan, N. & Tu, S.-T. Synthesis of Efficiently Green Luminescent CdSe/ZnS Nanocrystals Via Microfluidic Reaction. *Nanoscale Research Letters* **3**, 134-139, doi:10.1007/s11671-008-9125-5 (2008).

101 Nightingale, A. M. & de Mello, J. C. Controlled Synthesis of III-V Quantum Dots in Microfluidic Reactors. *Chemphyschem : a European journal of chemical physics and physical chemistry* **10**, 2612-2614, doi:Doi 10.1002/Cphc.200900462 (2009).

102 Baek, J., Allen, P. M., Bawendi, M. G. & Jensen, K. F. Investigation of Indium Phosphide Nanocrystal Synthesis Using a High-Temperature and High-Pressure Continuous Flow Microreactor. *Angew Chem Int Edit* **50**, 627-630, doi:10.1002/anie.201006412 (2011).

103 Kwon, B. H., Kim, H., Kim, Y., Kang, D. & Young Jeon, D. Synthesis of ZnSe Quantum Dots Using a Continuous-Flow Microreactor and Their White Emission through Energy Transfer. *ECS Solid State Letters* **2**, R27-R30, doi:10.1149/2.005308ssl (2013).

104 Kwon, B. H. *et al.* Continuous in situ synthesis of ZnSe/ZnS core/shell quantum dots in a microfluidic reaction system and its application for light-emitting diodes. *Small* **8**, 3257-3262, doi:10.1002/smll.201200773 (2012).

105 Song, H., Chen, D. L. & Ismagilov, R. F. Reactions in droplets in microfluidic channels. *Angewandte Chemie* **45**, 7336-7356, doi:10.1002/anie.200601554 (2006).

106 Chan, E. M., Alivisatos, A. P. & Mathies, R. A. High-temperature microfluidic synthesis of CdSe nanocrystals in nanoliter droplets. *J Am Chem Soc* **127**, 13854-13861, doi:Doi 10.1021/Ja051381p (2005).

107 Nightingale, A. M. *et al.* A stable droplet reactor for high temperature nanocrystal synthesis. *Lab on a chip* **11**, 1221-1227, doi:10.1039/c0lc00507j (2011).

108 Yen, B. K. H., Gunther, A., Schmidt, M. A., Jensen, K. F. & Bawendi, M. G. A microfabricated gas-liquid segmented flow reactor for high-temperature synthesis: The case of CdSe quantum dots. *Angew Chem Int Edit* **44**, 5447-5451, doi:Doi 10.1002/Anie.200500792 (2005).

109 Yang, H. W., Luan, W. L., Tu, S. T. & Wang, Z. M. M. Synthesis of nanocrystals via microreaction with temperature gradient: towards separation of nucleation and growth. *Lab on a chip* **8**, 451-455, doi:Doi 10.1039/B715540a (2008).

110 Marre, S. *et al.* Supercritical Continuous-Microflow Synthesis of Narrow Size Distribution Quantum Dots. *Advanced materials* **20**, 4830-4834, doi:10.1002/adma.200801579 (2008).

111 Marre, S., Adamo, A., Basak, S., Aymonier, C. & Jensen, K. F. Design and Packaging of Microreactors for High Pressure and High Temperature Applications. *Industrial & Engineering Chemistry Research* **49**, 11310-11320, doi:Doi 10.1021/Ie101346u (2010).

112 Marre, S., Baek, J., Park, J., Bawendi, M. G. & Jensen, K. F. High-Pressure/High-Temperature Microreactors for Nanostructure Synthesis. *Journal of the Association for Laboratory Automation* **14**, 367-373, doi:10.1016/j.jala.2009.06.005 (2009).

113 Ippen, C. *et al.* Large-scale synthesis of high quality InP quantum dots in a continuous flow-reactor under supercritical conditions. *Nanotechnology* **26**, doi:Artn 08560410.1088/0957-4484/26/8/085604 (2015).

114 Toyota, A. *et al.* Combinatorial Synthesis of CdSe Nanoparticles Using Microreactors. *J Phys Chem C* **114**, 7527-7534, doi:Doi 10.1021/Jp911876s (2010).

115 Krishnadasan, S., Brown, R. J., deMello, A. J. & deMello, J. C. Intelligent routes to the controlled synthesis of nanoparticles. *Lab on a chip* **7**, 1434-1441, doi:10.1039/b711412e (2007).

116 Nightingale, A. M. *et al.* Large-scale synthesis of nanocrystals in a multichannel droplet reactor. *Journal of Materials Chemistry A* **1**, 4067, doi:10.1039/c3ta10458c (2013).

117 Kim, K., Jeong, S., Woo, J. Y. & Han, C. S. Successive and large-scale synthesis of InP/ZnS quantum dots in a hybrid reactor and their application to white LEDs. *Nanotechnology* **23**, doi:Artn 06560210.1088/0957-4484/23/6/065602 (2012).

118 Norris, D. J., Efros, A. L. & Erwin, S. C. Doped nanocrystals. *Science* **319**, 1776-1779, doi:10.1126/science.1143802 (2008).

119 Anikeeva, P. O., Halpert, J. E., Bawendi, M. G. & Bulovic, V. Quantum Dot Light-Emitting Devices with Electroluminescence Tunable over the Entire Visible Spectrum. *Nano Lett* **9**, 2532-2536, doi:10.1021/nl9002969 (2009).

120 Shiang, J. J., Kadavanich, A. V., Grubbs, R. K. & Alivisatos, A. P. Symmetry of Annealed Wurtzite Cdse Nanocrystals - Assignment to the C-3v Point Group. *J Phys Chem-Us* **99**, 17417-17422, doi:DOI 10.1021/j100048a017 (1995).

121 Hines, M. A. & Guyot-Sionnest, P. Synthesis and characterization of strongly luminescing ZnS-Capped CdSe nanocrystals. *J Phys Chem-Us* **100**, 468-471, doi:DOI 10.1021/jp9530562 (1996).

122 Manna, L., Milliron, D. J., Meisel, A., Scher, E. C. & Alivisatos, A. P. Controlled growth of tetrapod-branched inorganic nanocrystals. *Nature materials* **2**, 382-385, doi:10.1038/nmat902 (2003).

123 Manna, L., Scher, E. C. & Alivisatos, A. P. Synthesis of soluble and processable rod-, arrow-, teardrop-, and tetrapod-shaped CdSe nanocrystals. *J Am Chem Soc* **122**, 12700-12706, doi:10.1021/ja003055+ (2000).

124 Schapotschnikow, P., Hommersom, B. & Vlugt, T. J. H. Adsorption and Binding of Ligands to CdSe Nanocrystals. *J Phys Chem C* **113**, 12690-12698, doi:10.1021/jp903291d (2009).

125 Bahrig, L., Hickey, S. G. & Eychmuller, A. Mesocrystalline materials and the involvement of oriented attachment - a review. *Crystengcomm* **16**, 9408-9424, doi:10.1039/c4ce00882k (2014).

126 Kwon, S. G. & Hyeon, T. Formation Mechanisms of Uniform Nanocrystals via Hot-Injection and Heat-Up Methods. *Small* **7**, 2685-2702, doi:Doi 10.1002/Smll.201002022 (2011).

127 Marre, S. & Jensen, K. F. Synthesis of micro and nanostructures in microfluidic systems. *Chemical Society reviews* **39**, 1183-1202, doi:10.1039/b821324k (2010).

CHAPTER 2

HIGH TEMPERATURE CONTINUOUS FLOW SYNTHESIS OF MULTILAYERED CADMIUM-BASED CORE-SHELL NANOCRYSTALS*

2.1. Introduction

Cadmium-based semiconductor nanocrystals have been the subject of intense study for their fluorescent properties.[1,2] These nanocrystals have many applications including solid-state lighting, displays, and fluorescence tagging.[1-3] Traditionally, Cd-based nanocrystals are based around CdSe for emission at green to red wavelengths or CdS for violet-blue emission.[3] Growth of a passivating ZnS shell substantially increases quantum yield for both CdSe and CdS;[3-8] CdSe/CdS/ZnS or CdSe/ZnSe/ZnS particles have the passivating benefits of ZnS combined with lower lattice strain between CdSe and the intermediate layer.[6]

Scalable quantum dot synthesis is hampered by several challenges. Quantum dots are typically synthesized using a hot injection method, where a burst of nucleation from relatively rapid mixing is used to create a large number of nanoparticles. However, this method is difficult to scale into large batches due to mixing issues; in addition, batch reactions have the intrinsic disadvantage of loading and unloading times.[3] Non-injection syntheses (also known as the "heating-up method"[9]), where the reactants are mixed at room temperature and then heated gradually to the target temperature, are more scalable, but still suffer from the general disadvantages of batch reactions. Additionally, batch reactions often employ dropwise addition

---

* This chapter has been adapted from the following publication: M.S. Naughton, V. Kumar, Y. Bonita, K. Deshpande, P.J.A. Kenis, "High Temperature Continuous Flow Synthesis of CdSe/CdS/ZnS, CdS/ZnS, CdSeS/ZnS nanocrystals", *Nanoscale,* **2015***, 7,* 15895-15903, DOI: 10.1039/C5NR04510J.

of Zn for shell growth, which is very difficult to directly translate to a flow reactor.[10] Direct imitation of dropwise addition in a flow reactor would require fast mixing of droplets added at regular residence time intervals, greatly increasing reactor complexity and pressure drop. The alternative shell growth method using successive ion layer adhesion and reaction (SILAR) shows promise, but requires two injections per monolayer[6] which poses reactor design challenges for large shells.

More recently, quantum dot synthesis in microfluidic flow reactors has demonstrated promise for scalable synthesis.[11,12] Microfluidic reactors have the advantage of rapid heating/cooling and offer higher throughput than hot injection batch systems.[3,10,13-15] The addition of high quality microfluidic mixers can offer mixing times of less than a second at the cost of increased pumping losses due to pressure drop. Microfluidic tube reactors using PTFE or steel tubes have been shown to produce quality Cd-based nanocrystals with quantum yields of up to 78%.[3,10] With a more complex emulsion-based microreactor, CdSe particles with full width at half maximum (FWHM) of 27 nm were successfully generated.[13] Use of a microreactor can also narrow particle size distribution.[16]

However, with limited exceptions, many microreactor synthesis methods are constrained by lower reactant throughput.[14,15] The relatively low volumetric flow rates (on the order of μL/min) used with these designs limits the mass production rate of the quantum dots.[17] Microreactor channel diameters are in the range of 0.3 mm,[3] which causes high pumping losses and may cause challenges when scaling out to multi-channel configurations for large-scale production. Emulsion-based systems have the potential added disadvantages of an additional separation step, narrower flow rate range for emulsions, potential contamination issues[18], and increased pumping losses from the carrier liquid and smaller diameters for the reactants.[13] The carrier liquid can

also affect the course of the reaction; common inert fluorocarbon carrier liquids can contain large amounts of dissolved gases, which may affect the reaction near the boundaries of the emulsion.[18]Despite these limitations, synthesis of up to 150 g/day of CdTe was demonstrated in a robust emulsion-based reactor with the ability to generate CdSe or CdSeTe alloy particles, which is a significant demonstration of microreactor viability.[14,15,19] However, the lower flow rate of the reagent in droplet-based reactors reduces throughput for a given size of reactor and the particles synthesized did not cover the purple-blue region.

In this work, we demonstrate a streamlined "heat injection" continuous flow system for core-multishell quantum dot synthesis. This reactor uses liquid-phase chemistry that is not mixing-sensitive at room temperature, eliminating the need for any preheating or in-line mixing, and has channels that are less than 1 mm in diameter, thus suitable for rapid heating/cooling. Shell growth is conducted with a single mixing step or even no additional steps, in the case of CdSe/CdS; this methodology eliminates the need for the multiple injections required to simulate dropwise addition. We apply this millifluidic reactor to the known systems of CdSe/CdS/ZnS and CdS/ZnS. In addition, we demonstrate the ability to synthesize CdSeS/ZnS alloy nanoparticles which to our knowledge has not been shown previously in a continuous flow system.

2.2 Experimental

Reactor Design. The reactor is a stainless steel coil with an inner diameter of 2.2 mm and an outer diameter of 3.2 mm. The total volume was 7.24 ml for the CdSe synthesis or 16.8 ml for the CdS and CdSeS syntheses, indicating millifluidic dimensions. With the flow rates used in this paper, the Reynolds number was smaller than 200, indicating laminar flow; thus, the premixing is the dominant source of mixing. Furthermore, mixing inside the reactor occurs

through diffusive mixing. The results between the two reactors were compared by running an identical trial in each reactor and determined to be the same for constant residence times, which is supported by literature.[17] The temperature of the reactor is held constant using an oil bath full of Dynalene HT (Dynalene Inc.), which has a boiling point >385 °C that is well above the 270 °C temperature used here. The oil bath was heated using an EchoTherm HP40 hot plate (Torrey Pines Scientific) and the temperature was measured using a stainless steel immersion probe (Torrey Pines Scientific). The reactants were supplied by a PHD 2000 syringe pump (Harvard Apparatus), which was connected to the reactor using PTFE tubing. The effluent from the reactor was collected in open air in glass vials; the length of the outlet tubing ensured that the reactants were cooled below the 250 °C auto ignition temperature of octadecene.

Synthesis Chemistry. Cadmium oxide (99.5%), selenium (99.99%), sulfur (99.98%), oleic acid (90%), oleylamine (70%), octadecene (ODE) (90%), trioctylphosphine (TOP) (90%), and zinc diethyldithiocarbamate ($ZnDDTC_2$) (97%) were ordered from Sigma-Aldrich. Unless stated otherwise, the quantum dot synthesis used 0.0663 g CdO (0.51 mmol) dissolved in 3.1 mL of oleic acid at 200 °C forming a clear solution. For CdSe, TOP-Se solution was created by mixing 0.041 g Se with 4.8 mL ODE and 0.34 mL TOP and heating to 100 °C for 10 minutes under nitrogen. For CdS, ODE-S solution was created by mixing 0.0167 g S (0.51 mmol) with 5.1 mL ODE and heating to 70 °C in air. For CdSeS, the anion solution was the same 5.1 mL volume and was composed of 50 vol% TOP-Se solution and 50 vol% ODE-S solution. For a standard synthesis, 3.1 mL of the Cd oleate solution (0.16 M Cd) and 5.1 mL of the anion solution (0.1 M Se or S) was mixed with 51 mL ODE for approximately one minute and pumped through the tube reactor, which was held at 270 °C with standard residence times (reactor volume / volumetric flow rate) of three minutes.

For shell growth, a standard stock solution of 0.058 g $ZnDDTC_2$ dissolved in 1.6 mL of TOP (0.1 M $ZnDDTC_2$) was used. Standard shell addition amounts were 1.6 mL of the $ZnDDTC_2$ solution in TOP mixed with 1.6 mL of oleylamine (as a sacrificial amine for the $ZnDDTC_2$ decomposition) and 10 mL of reacted core solution. The amount of $ZnDDTC_2$ added roughly corresponds to 2 monolayers, which is within the optimal range for CdSe/ZnS.[20] The reactants were mixed and pumped through the tube reactor at 140 °C for five minutes for CdSe; for CdS and CdSeS, an improved shell growth procedure of 110 °C for 30 minutes was used instead. The reactor was flushed with ODE after each run; examination of the flushed ODE under UV light did not show fluorescence, indicating that there was not a significant buildup of quantum dots remaining in the reactor. In addition, a reactor was cut open after ~50 runs and showed no apparent buildup (**Figure 2.10**).

Characterization. The solutions were typically diluted 1:40 in chloroform to obtain absorbance between 0.02 and 0.1 absorbance units (substantial additional dilution was required for CdS and sometimes for other samples) and were imaged in solution without additional purification or size selection. Fluroescence results from a common purification process (mix with methanol and ethanol in a 5:1 alcohol:effluent ratio, shake to generate an emulsion, centrifuge at 3,000 rpm for 5 minutes, pour off liquid, suspend in hexane) were within 90-110% of the values obtained from the as-synthesized solution.[14] Absorption spectra were obtained from an 8453 UV-Vis Diode Array System spectrophotometer (Agilent) and fluorescence spectra were obtained from a Jobin-Yvon Fluoromax-3 spectro-fluorimeter (Horiba); a 490 nm excitation wavelength was used for CdSe and excitation at 350 nm was used for CdS and CdSeS. Quantum yields (QY) were determined by comparing to a quinine sulfate solution in 0.1 M H_2SO_4 (58% quantum yield).[21] For CdSe, this method had questionable applicability due to the different

excitation wavelength; therefore, quantum yield was also determined using a Quantamaster 40 spectrophotometer (Photon Technology International) at the Midland research facility of The Dow Chemical Company, which was found to agree with the value relative to quinine sulfate within 5%.

2.3 Results and Discussion

Mixing Time Sensitivity. Among the different operational parameters, we explored the possible effect of mixing time first. For these experiments solutions of the Cd^{2+} cation and Se (or S) precursors where mixed in less than 1 min in a beaker, so offline. Subsequently, the experiment was conducted by using a syringe pump to introduce the mixture into the reactor. Other reactor setups reported in the literature[3] incorporate inline mixing where a Cd stream is mixed with a Se stream at low temperature, then heated in the reactor. For these chemistries, the reactants appear to have minimal sensitivity to mixing time at room temperature; spectra of a Cd + Se reagent mixture left overnight at room temperature yielded no fluorescence or particle formation. Based on this result, mixing could be done on a larger scale over the course of hours, simplifying reactor design and minimizing the need for microscale inline mixers. For the purposes of this study, cold offline mixing appears equivalent to cold inline mixing, allowing for the heat injection setup where the premixed reactants are rapidly heated to the reaction temperature. Other parameters such as time, temperature, and shell thickness were explored in experiments specific to the reactant system.

Synthesis of CdSe Nanoparticles. The initial goal for these experiments was to make CdSe nanoparticles using a relatively air-insensitive procedure. Many literature procedures use trioctylphosphine oxide (TOPO) as a solvent, which has the disadvantage of being solid at room temperature, and/or use dimethyl cadmium or hydrogen selenide/sulfide, which are highly toxic

gases. Here, we focus on a lower cost and less hazardous CdSe synthesis, using CdO reacted with bioavailable oleic acid and Se reacted with TOP in a solvent primarily composed of ODE. This system is entirely liquid phase, making it suitable for pumping at low temperature. The initial Cd:Se molar ratio was 1.44 with a Cd concentration of 0.008 M.

Initial studies explored the effects of temperature on particle fluorescence. Initial tests were conducted at 220 °C and 270 °C, along with a batch experiment conducted at 180 °C. The highest temperature of 270 °C gave substantially higher fluorescence than the other samples, which is likely due to reduced defects at higher temperature along with greater conversion and is consistent with literature results. The FWHM, which is correlated to the size dispersion of the particles, is 38 nm at 270 °C, 35 nm at 225 °C, or 130 nm at 180 °C (in batch). These FWHMs are relatively wide and indicative of breadth of nanoparticle sizes, which may be due to several process factors. Some possibilities are lower temperature as compared to other procedures, which may be 300 °C or higher, or use of a non-coordinating solvent, since ODE is the bulk of the system and does not act as a capping agent to slow growth. Additionally, using a constant temperature zone instead of higher temperature injection followed by lower temperature growth could also broaden particle size distribution. Broader particle size distribution may also be caused by axial dispersion in the reactor. Based on these trials, 270 °C was used for subsequent experiments due to its higher fluorescence and adequate FWHM.

ZnS Shell Growth over CdSe. The standard procedure in the literature is to grow a shell, typically ZnS, over the CdSe cores to passivate the particle and thus enhance fluorescence. However, literature methods often use dropwise addition of Zn precursors, which is not possible to simulate in the present reactor and would cause scaling challenges. An alternate method

mentioned in several studies[4,5,10] is to use a single source precursor, zinc diethyldithiocarbamate (Zn $DDTC_2$), which thermally decomposes into ZnS[5] according to Equations 1-2:

$$Zn(S_2CNEt_2)_2 + 2NH_2R \rightarrow ZnS + H_2S + 2S{=}C(NEt_2)(NHR) \quad (1)$$

$$S{=}C(NEt_2)(NHR) + NH_2R \rightarrow S{=}C(NHR)_2 + NHEt_2 \quad (2)$$

Use of this precursor allows for premixing of the reactants without any intermediate purification steps, consistent with the core synthesis method and compatible with potential addition of inline mixing. The amount of ZnS precursor added was calculated to be ~2 monolayers based on literature correlations.[20] TOP was used to solubilize and stabilize the $ZnDDTC_2$ to create a 0.1 M concentration of $ZnDDTC_2$ in TOP. Oleylamine was also added as the sacrificial amine in large molar excess at a volumetric ratio of 1.6 ml oleylamine / 10 ml core solution; oleylamine may have also acted as a secondary capping agent. The resulting mixture remained liquid and was straightforward to pump at room temperature.

The resulting CdSe/ZnS quantum dots were substantially more fluorescent than the CdSe cores, as shown in **Figure 2.2**. The absorption of the core-shell particles increased with shell growth by a factor of 1.2; by contrast, the fluorescence of the particles, shown here normalized to the maximum for the core particles, increased by a factor of 5 for a three minute residence time or a factor of 6 for an eight minute residence time. These results show substantial fluorescence improvement for the core-shell particles even when considering the increase in absorption. Another test for the core-shell particle enhancement involved mixing the particles with pyridine in a 1:1 volumetric ratio. Pyridine is an alternate ligand that can quench the fluorescence of core particles due to incomplete ligand exchange from mixing at room temperature. Mixing with pyridine quenched CdSe particles synthesized in the flow reactor. The fluorescence results

demonstrate minimal quenching from the presence of pyridine, further demonstrating successful shell growth. The FWHM of the particles increased by 5 nm while the peak location red-shifted by 10 nm, from 587 nm to 597 nm, during shell growth.

The quantum yield of the samples was measured versus quinine sulfate; an integrated sphere was used to verify that the relative quantum yields obtained were accurately translated into absolute quantum yield. The quantum yield was calculated using the standard method of determining absorbance-normalized fluorescence output relative to the dye, then multiplying by the quantum yield of the quinine sulfate dye (58%). Quinine sulfate was used instead of Rhodamine to enable better comparison with CdS and CdSeS particles. The quantum yield calculated from the results was 2% for the core particles and 12% for the core-shell particles, which is low compared to results reported in the literature.[10,16] The throughput was 10-15x higher than a similar synthesis also conducted in a stainless steel tube reactor due to the ability to use higher reagent concentrations in this millifluidic reactor. However, the quantum yield was lower than the 28% reported in the literature, indicating that improved quantum yield was the next goal.[17] To improve performance, the synthesis procedure was changed to use 1:1 stoichiometry and a longer shell growth time of five minutes; the quantum yield increased to 20%, but this performance was still relatively low.

Synthesis of CdSe/CdS/ZnS Nanoparticles. To further improve the performance of the CdSe particles, an alternate shell was used to minimize lattice strain. CdS has a lattice constant similar to CdSe with a lattice mismatch of only 4% as compared to the ZnS mismatch of 12%; this property demonstrates that CdS can be a shell material that will cause fewer defects and traps from the lattice mismatch.[6,7] Although there are several methods to synthesize a CdS shell (dropwise addition of Cd or S, Cd diethyldithiocarbamate decomposition, SILAR synthesis of

CdS layer(s)), a simpler method was tested where TOP-S was used in place of a fraction of the TOP-Se. Since Se has a higher reactivity than S, the CdSe cores nucleate first followed by CdS overgrowth within a single reactor stage. This theory is supported by the fluorescence results in **Figure 2.3**, where the core-shell particles are substantially blue-shifted relative to the core-shell particles using only Se in the initial step. Similar peak locations to the 10:90 Se:S particles were obtained with particles using a 10% Se concentration with the same concentration of Cd, indicating the CdSe core has a similar size independent of the presence of S. The quantum yield of these CdSe/CdS particles was 20%, which is similar to the previous CdSe/ZnS results, indicating that CdS shell growth was successful.

To combine the lower lattice strain from CdS with the superior passivation of ZnS, a ZnS shell was overgrown over the CdSe/CdS particles. Particles were synthesized using this method from identical cores using three shell growth methods. One set of particles was created using the standard $ZnDDTC_2$ decomposition at 140 °C. In an alternate procedure to give more time for Zn adsorption, a five minute adsorption step of 110 °C was followed by a $ZnDDTC_2$ decomposition step at 160 °C, similar to a literature method.[22] A third procedure used a S overgrowth step at 220 °C for five minutes followed by the standard 140 °C $ZnDDTC_2$ decomposition step; the S overgrowth was essentially a half-SILAR step meant to promote Zn^{2+} cation adsorption by coating the nanocrystal with a half-monolayer of S. The fluorescence results in **Figure 2.4** show similar fluorescence for the three shell growth procedures. The CdS/S/ZnS and 110 → 160 °C structures show a modest improvement in QY versus the standard procedure (44% versus 37% for standard CdSe/CdS/ZnS). Despite passivation, photobleaching did occur over the course of hours when the quantum dots were dispersed on a polymer surface from a hexane solution[23].

Another goal for these CdSe/CdS/ZnS particles was to achieve longer wavelength emissions in the orange-red region (>590 nm). Longer emission wavelengths were achieved simply by using a longer residence time of 15 minutes for the CdSe/CdS synthesis. Subsequently, ZnS was overgrown using an 110 → 140 °C shell growth procedure in ~2 monolayer increments. **Figure 2.5** shows the absorbance and fluorescence spectra for the CdSe/CdS/ZnS particles, which show orange fluorescence peaks at 604, 614, and 618 nm as more ZnS is grown causing a redshift. The quantum yield decreases sharply from a maximum of 60% with ~2 monolayers (1 addition) to 32%, then 27% with further additions of the $ZnDDTC_2$ precursor. This result is consistent with literature knowledge for CdSe that 1-2 monolayers of ZnS is optimal before lattice strain starts to reduce quantum yield.[6] The FWHM for the particles increased from 48 nm with ~2 monolayers of ZnS to 55 nm with ~6 monolayers of ZnS. These results show that ~2 monolayers of ZnS is optimal for these particles from both a performance and process standpoint.

Synthesis of CdS/ZnS nanoparticles. To achieve shorter wavelength emission, CdS was used in place of CdSe. CdS has a larger band gap which enables purple-blue emission for particles that are much larger than the equivalent emission CdSe particles, allowing for easier synthesis and higher reaction temperatures. Preliminary studies focused on synthesizing CdS/ZnS particles using TOP-S in place of TOP-Se in a procedure otherwise identical to that used for CdSe/ZnS. The initial CdS particles had quantum yield of 17% and FWHM of only 28 nm (**Figure 2.6**), showing that use of the less reactive TOP-S reduces size dispersion relative to use of TOP-Se. The peak was centered at 443 nm, which is near the boundary between purple and

blue emission. Unfortunately, ZnS shell growth over these particles almost entirely quenched the fluorescence and caused orange trap emission to be the dominant product (**Figure 2.6**). The fluorescence was greatly reduced, with the new particles producing <1% QY overall. However, small signs of a core-shell peak appeared at 460 nm, consistent with shell growth causing a red shift. Based on this result, a hypothesis was generated that the poor shell growth was due to improper ZnDDTC2 adsorption on the particle surface; partial ZnS overgrowth would disrupt the surface and create sites for traps. To improve ZnDDTC2 adsorption, a core growth procedure was developed that removed the passivating ligand TOP from the reaction mixture. This simplified procedure dissolved the same amount of S in ODE using the terminal double bond as a ligand to bind S and removed the need to use a glove box with the S binding. The cores produced from this procedure are similar in quality to the CdS cores formed with TOP-S. However, the quantum yield after ZnS overgrowth was much higher than when using TOP-S and yielded minimal trap emission (**Figure 2.7**). A quantum yield of 23% was achieved with a FWHM of 31 nm, which was considerably narrower than the CdSe/ZnS particles. The ZnS added was approximately 2 monolayers; additions to grow the particles to approximately 4 or 6 monolayers decreased quantum yield without significantly changing FWHM or peak location. The purple-blue emission (431 nm) obtained from these particles substantially increases the range of colors possible from the flow reactor, although the quantum yield is not substantially higher than the core particles.

Due to concerns about the low reactivity of the S-rich surface, an alternate core-shell synthesis focused on forming CdS with a small amount of CdSe (9:1 ODE-S:TOP-Se ratio) to promote ZnDDTC2 adsorption. This procedure was intended to use the larger band gap of CdS to achieve purple emission while utilizing the higher reactivity of Se to promote ZnS attachment

and shell growth. **Figure 2.8a** shows the absorbance at 1/40 concentration for the 10:90 Se:S CdSeS particles, which have behavior similar to that of the CdS particles. After the absorbance was diluted to obtain absorbance values below 0.1 at 350 nm, in accordance with our standard procedure, the quantum yield of CdSeS/ZnS particles with two monolayers of ZnS was 38% while CdSeS/ZnS particles with three monolayers of ZnS had quantum yield of 40% (**Figure 2.8c**). This result differs from the ZnS shell results for CdSe due to the lower lattice strain between CdS and ZnS; further ZnS overgrowth did decrease performance possibly due to defect site accumulation.

The higher absorbance of CdSeS and CdS particles can cause higher effective fluorescence output relative to CdSe. Both 10:90 Se:S CdSeS and CdS particles have substantially higher absorbance (0.3-0.42) at the excitation wavelength of 350 nm than CdSe particles, which have absorbance around 0.05 at the excitation wavelength of 490 nm. Since fluorescence is proportional to absorbance, the CdSeS and CdS particles in a given volume produce higher total fluorescence relative to CdSe even when considering the higher quantum yield from CdSe particles.

Synthesis of CdSeS/ZnS nanoparticles. CdSeS particles have the ability to generate fluorescence peaks intermediate between CdS and CdSe, making them desirable to target specific wavelengths. To generate alloy nanoparticles, Se and S precursors with similar reactivity are generally required. Although there is literature work showing that TOP-Se:TOP-S ratios of 1:7 or lower can yield alloy nanocrystals, this method results in large amounts of excess sulfur, which can interfere with subsequent synthesis steps and leaves excess reactants in the mixture.[24] The large excess of sulfur is required due to the lower reactivity of sulfur as compared to selenium. Here, TOP-Se was combined in a 50:50 molar ratio with ODE-S, which

is more reactive than TOP-S. The resulting cores showed appropriate alloy behavior intermediate between the CdS and CdSe behavior with a peak location of 483 nm (**Figure 2.9**). CdS particles in this emission range would be considerably larger, reducing their stability in a colloidal mixture, while CdSe particles in this emission range would be very small and difficult to synthesize. Increased residence time to 15-18 minutes resulted in lower quantum yield for the cores (2% for 15-18 minutes vs 5% for three minutes) and a red-shifted peak location of 502 nm. Changing the residence time offers a simple way to tune the peak location, but very large particles would be better replaced by CdSe particles. At 3 minute residence times, the capability for high throughput particle production compares favorably to literature focused on high throughput due to higher flow rates (5-10 ml/min of reagent in this system vs 3 ml/min through five parallel channels) and the omission of an overnight aging step post-mixing.14

ZnS was overgrown over the CdSeS cores synthesized with a three minute residence time to make CdSeS/ZnS particles with shells of 2, 4, and 6 monolayers (1, 2, or 3 $ZnDDTC_2$ additions of ~2 monolayers each). The resulting quantum yields were 49%, 46%, and 30% respectively, with peak locations in the range of 490-493 nm. These results indicate that growing 4 or more ZnS monolayers decreased the quantum yield; however, this decrease was not as sharp as the decline observed with the 20:80 Se:S CdSe/CdS/ZnS particles. This shell growth behavior supports the hypothesis that CdSeS alloy formation occurred, as opposed to small CdSe particles with a CdS shell. The peak location of the CdSeS is also blue-shifted relative to the 20:80 CdSe despite the presence of more Se in the CdSeS, which would normally create larger particles and cause a redshift. Thus, these results demonstrate the successful synthesis of CdSeS/ZnS particles with good quantum yield.

2.4 Conclusions

In summary, we reported the liquid phase heat injection synthesis of CdSe, CdS, and CdSeS (alloy) quantum dots in single step procedures that did not require in-line mixing. Quantum yields of up to 60% were achieved by overgrowing ZnS shell or CdS shells with only one added reaction step in the case of CdSe or CdSeS. These syntheses also focused on stoichiometric chemistry, reducing wasted reagents and increasing the viability of solvent recycling. The entire visible spectrum ranging from purple-blue to orange was covered, indicating the versatility of the reactant system, and flow rates were higher (on the order of 10 mL/min) than comparable flow reactors also used to synthesize quantum dots.

Future work in this area could focus on further improving quantum yield, reducing photobleaching, and reactor throughput. Improved quantum yield is always desirable for fluorescence and could be examined by optimizing shell growth in smaller increments and changing reagent concentration. Reduced photobleaching could be achieved via thicker shell growth. Improved throughput could be achieved with higher flow rates while keeping the residence time constant or by scaling out, that is creating multi-channel reactors.

Acknowledgements

We gratefully acknowledge financial support from the Dow Chemical Company for research agreement #226772AC and a graduate fellowship to MSN. We thank Steven Warren for assistance with TEM imaging as well as Dr. Pete Trefonas, Dr. Jieqian Zhang, Dr. Jong Park, You “Andy” Zhai, and Nuri Oh for stimulating discussions.

2.5. Figures

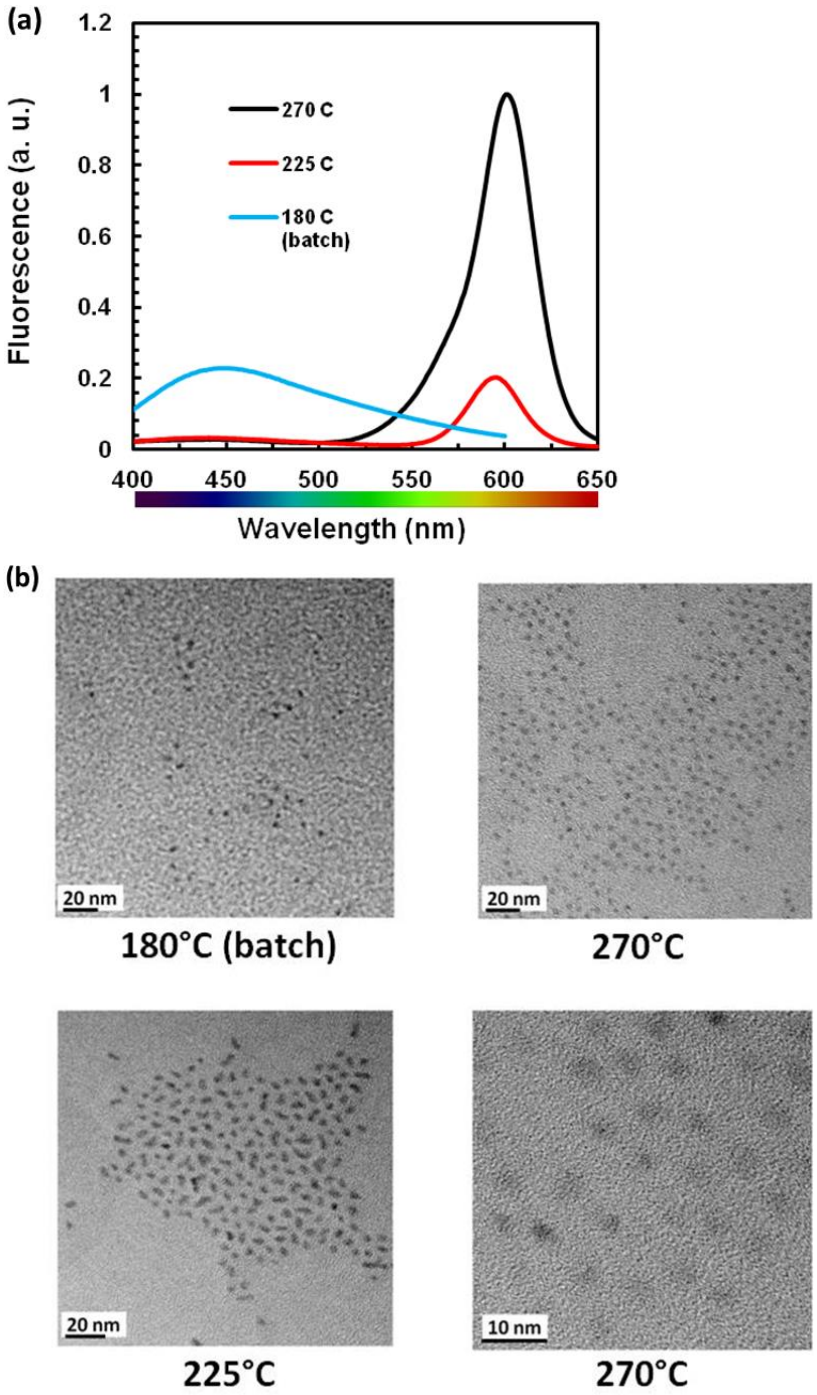

Figure 2.1. (a) Fluorescence spectra of CdSe particles synthesized at varying temperatures and **(b)** corresponding TEM images showing wide particle size distribution for 180°C and 225°C. Fluorescence values are normalized where the peak value for 270°C = 1. Excitation: 350 nm.

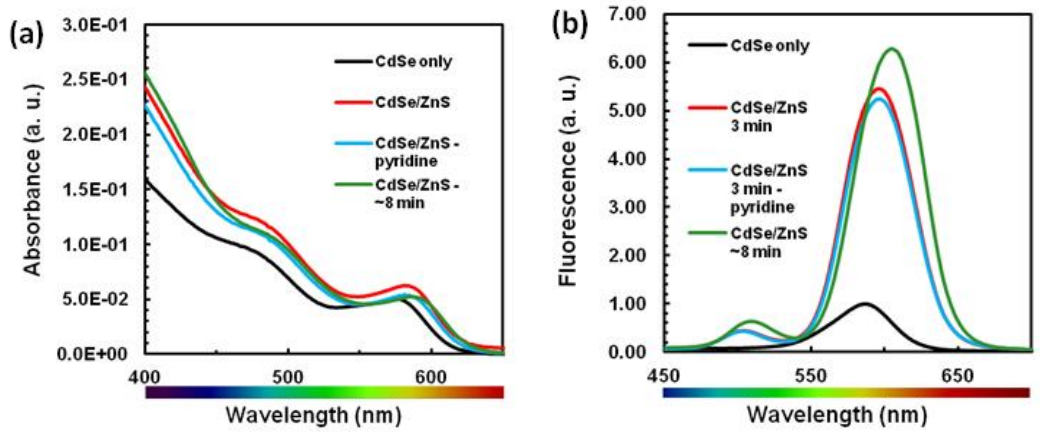

Figure 2.2. (a) Absorbance and **(b)** fluorescence spectra of CdSe/ZnS quantum dots in arbitrary units with varying residence time and pyridine treatment. The pyridine-treated sample was diluted 1:1 with pyridine and then diluted to the same concentration as the standard CdSe/ZnS dots.

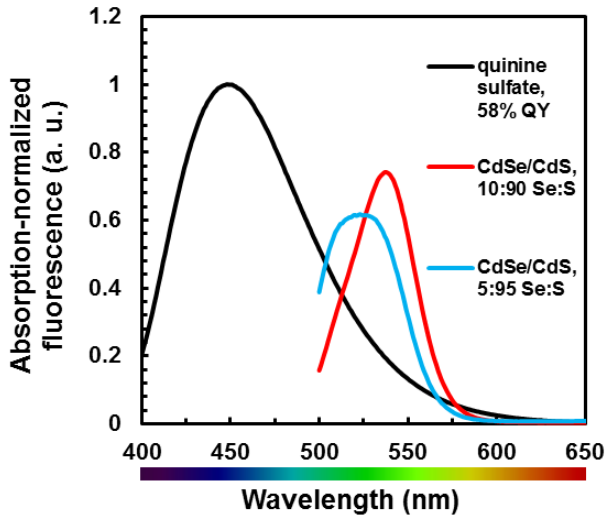

Figure 2.3 Absorption-normalized fluorescence for CdSe/CdS particles as a function of Se:S ratio. Excitation: 490 nm. Fluorescence below 500 nm is not shown due to proximity to the excitation signal.

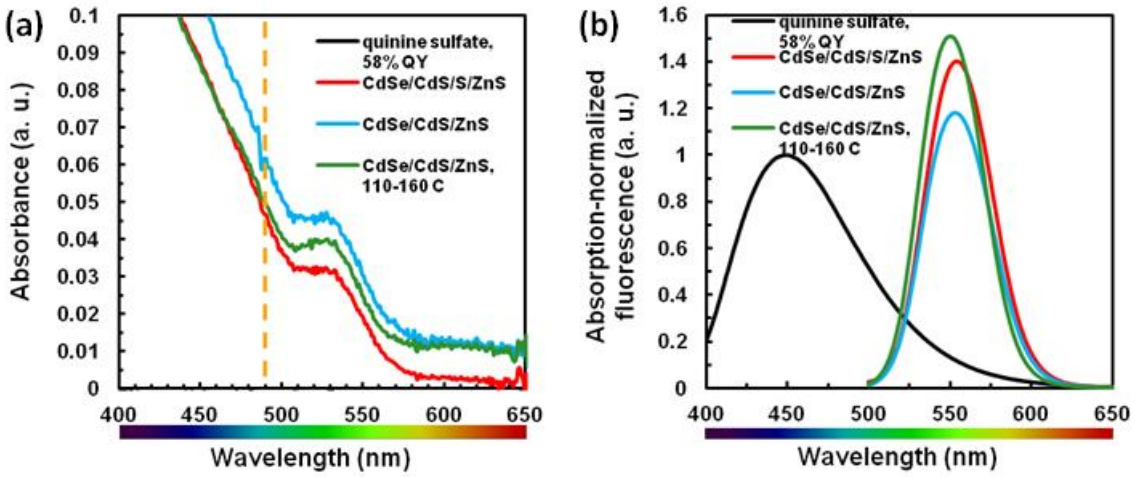

Figure 2.4. (a) Absorbance and **(b)** fluorescence spectra of CdSe/CdS/ZnS quantum dots in arbitrary units with varying shell growth procedure. Excitation: 490 nm.

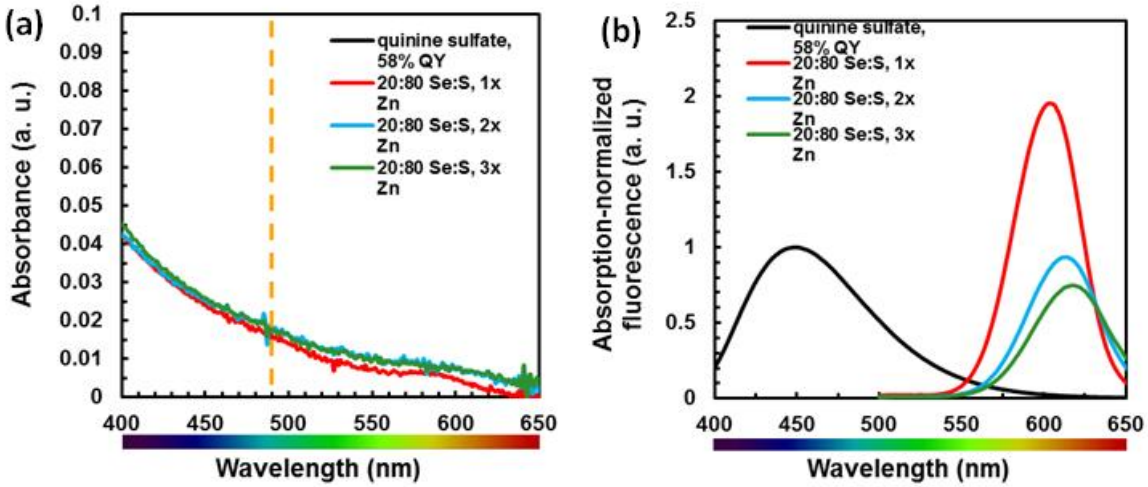

Figure 2.5. (a) Absorbance and **(b)** fluorescence spectra of CdSe/CdS/ZnS quantum dots in arbitrary units with varying ZnS shell growth amount. 1, 2, or 3 additions corresponds to ~2, 4, or 6 monolayers. Excitation: 490 nm.

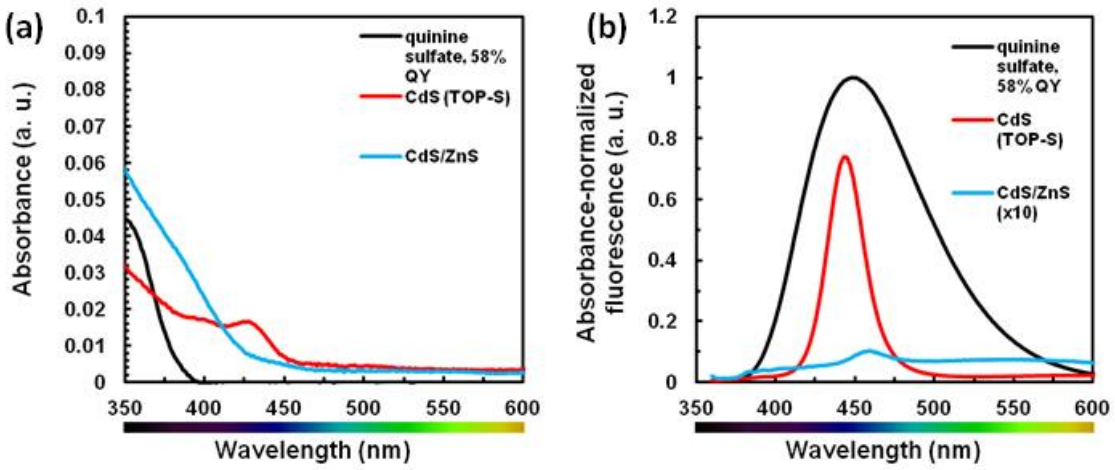

Figure 2.6. (a) Absorbance and **(b)** fluorescence spectra of CdS/ ZnS quantum dots in arbitrary units with and without shell growth. CdS/ZnS fluorescence is shown 10 times higher than measured to show the peak location. Excitation: 490 nm.

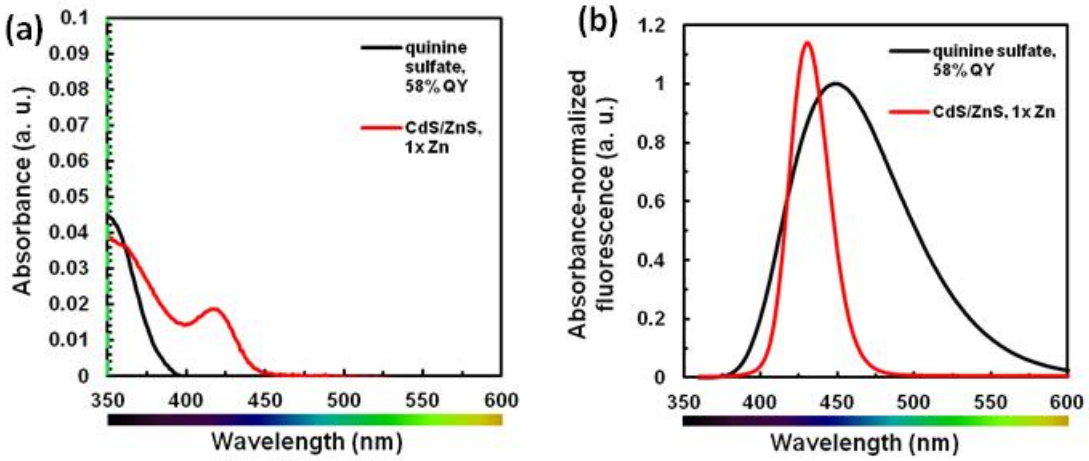

Figure 2.7. (a) Absorbance and **(b)** fluorescence spectra of CdS/ZnS quantum dots in arbitrary units. Excitation: 490 nm.

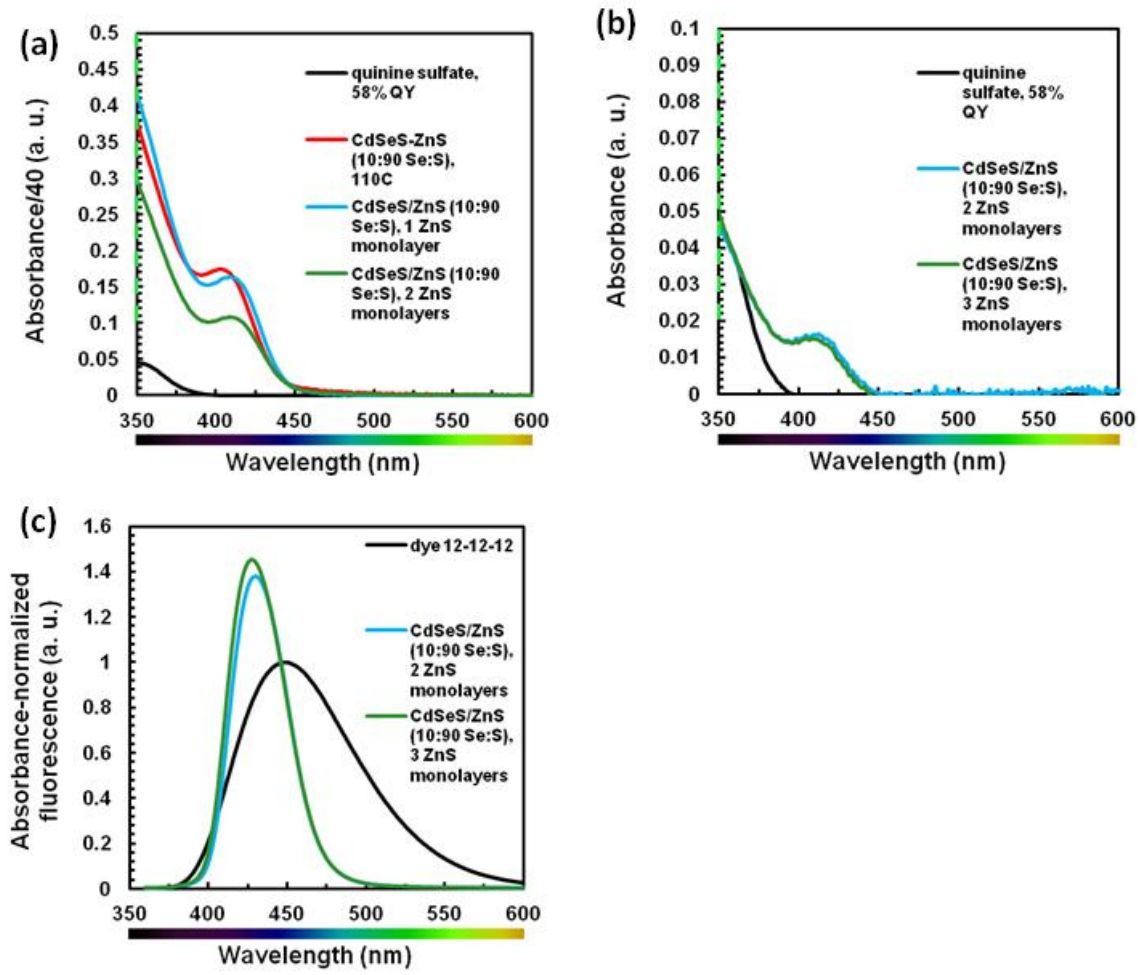

Figure 2.8. **(a)** Absorbance at 1/40 dilution, **(b)** absorbance in arbitrary units, and **(c)** absorption-normalized fluorescence in arbitrary units for CdSeS/ZnS particles with varying ZnS monolayers.

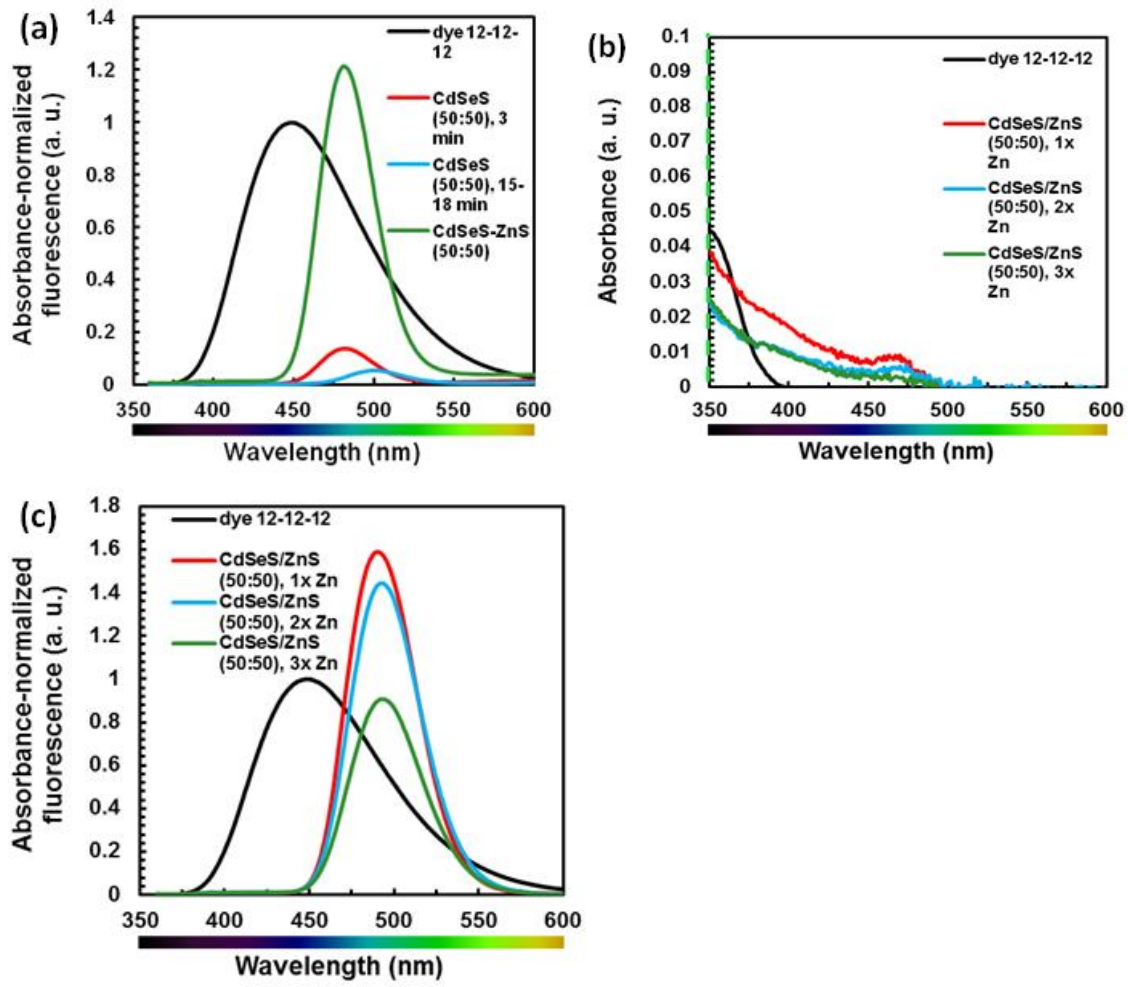

Figure 2.9. (a) Absorbance-normalized fluorescence of CdSeS cores, **(b)** absorbance, and **(c)** absorbance-normalized fluorescence spectra of CdSe/CdS/ZnS quantum dots in arbitrary units with varying shell growth procedure. Excitation: 490 nm.

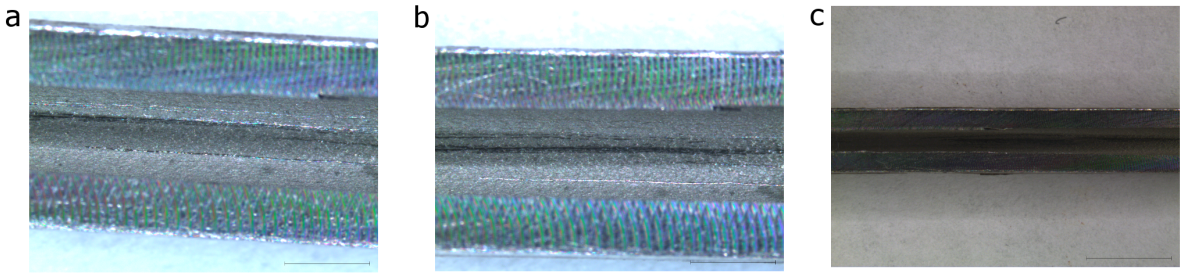

Figure 2.10. (a) and **(b)** show the images of a single "cut-open" section of the reactor at two different positions. Scale bar = 1 mm **(c)** shows another "cut-open" section of the reactor different from (a) and (b). Scale bar = 2 mm. All the above images show no signs of deposition of quantum dots on the inside walls of the reactor.

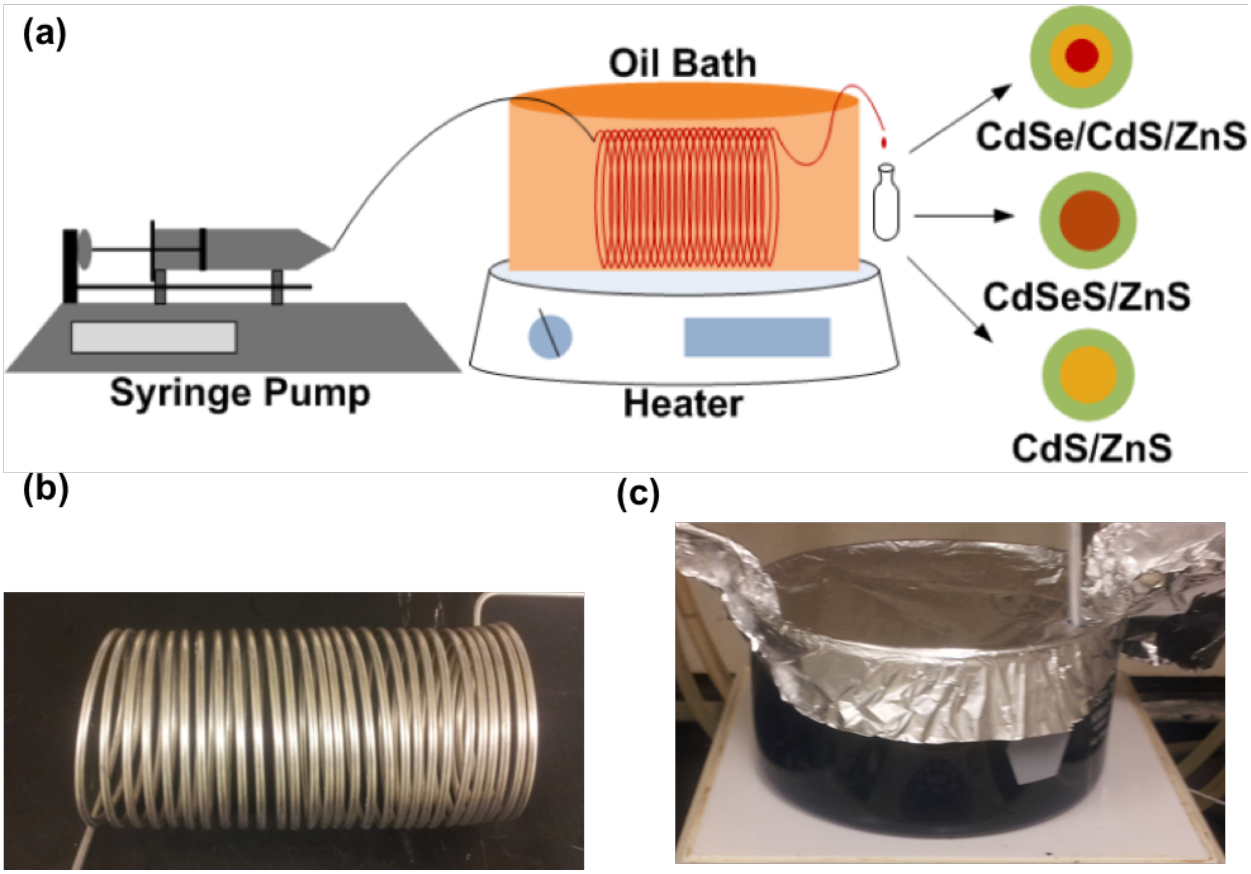

Figure 2.11. (a) Schematic of the continuous flow reactor setup used for synthesis of multi-layered Cd-based quantum dots discussed in this work. The premixed precursors are loaded in the syringe and pumped into the reactor at a set flow rate using a syringe pump. The reactor is maintained at the required temperature using temperature controlled oil bath. The product exiting the reactor is finally collected in an air-tight collection vial. **(b)** The continuous flow reactor fabricated out of a stainless steel coil with an ID of 2.2 mm. **(c)** The continuous flow reactor setup comprising the stainless steel flow reactor immersed in an oil bath. 5

2.6. References

1 Bera, D., Qian, L., Tseng, T.-K. & Holloway, P. H. Quantum Dots and Their Multimodal Applications: A Review. *Materials* 3, 2260-2345 (2010).

2 West, J. L. & Halas, N. J. Engineered Nanomaterials for Biophotonics Applications: Improving Sensing, Imaging, and Therapeutics. *Annual Review of Biomedical Engineering* 5, 285-292, doi:doi:10.1146/annurev.bioeng.5.011303.120723 (2003).

3 Yang, H., Luan, W., Wan, Z., Tu, S.-t., Yuan, W.-K. & Wang, Z. M. Continuous Synthesis of Full-Color Emitting Core/Shell Quantum Dots via Microreaction. *Crystal Growth & Design* 9, 4807-4813, doi:10.1021/cg900652y (2009).

4 Trindade, T., O'Brien, P. & Zhang, X.-m. Synthesis of CdS and CdSe Nanocrystallites Using a Novel Single-Molecule Precursors Approach. *Chemistry of Materials* 9, 523-530, doi:10.1021/cm960363r (1997).

5 Dethlefsen, J. R. & DÃ¸ssing, A. Preparation of a ZnS Shell on CdSe Quantum Dots Using a Single-Molecular ZnS Precursor. *Nano Letters* 11, 1964-1969, doi:10.1021/nl200211n (2011).

6 Xie, R., Kolb, U., Li, J., BaschÃ©, T. & Mews, A. Synthesis and Characterization of Highly Luminescent CdSeâˆ’Core CdS/Zn0.5Cd0.5S/ZnS Multishell Nanocrystals. *Journal of the American Chemical Society* 127, 7480-7488, doi:10.1021/ja042939g (2005).

7 Reiss, P., Bleuse, J. l. & Pron, A. Highly Luminescent CdSe/ZnSe Core/Shell Nanocrystals of Low Size Dispersion. *Nano Letters* 2, 781-784, doi:10.1021/nl025596y (2002).

8 Laurino, P., Kikkeri, R. & Seeberger, P. H. Continuous-flow reactor-based synthesis of carbohydrate and dihydrolipoic acid-capped quantum dots. *Nat. Protocols* 6, 1209-1220 (2011).

9 Kwon, S. G. & Hyeon, T. Formation Mechanisms of Uniform Nanocrystals via Hot-Injection and Heat-Up Methods. *Small* 7, 2685-2702, doi:Doi 10.1002/Smll.201002022 (2011).

10 Wang, H., Nakamura, H., Uehara, M., Yamaguchi, Y., Miyazaki, M. & Maeda, H. Highly Luminescent CdSe/ZnS Nanocrystals Synthesized Using a Single-Molecular ZnS Source in a Microfluidic Reactor. *Advanced Functional Materials* 15, 603-608, doi:10.1002/adfm.200400164 (2005).

11 Pan, J., El-Ballouli, A. O., Rollny, L., Voznyy, O., Burlakov, V. M., Goriely, A., Sargent, E. H. & Bakr, O. M. Automated Synthesis of Photovoltaic-Quality Colloidal Quantum Dots Using Separate Nucleation and Growth Stages. *ACS Nano* 7, 10158-10166, doi:10.1021/nn404397d (2013).

12 Yen, B. K. H., Günther, A., Schmidt, M. A., Jensen, K. F. & Bawendi, M. G. A Microfabricated Gas–Liquid Segmented Flow Reactor for High-Temperature Synthesis: The Case of CdSe Quantum Dots. *Angewandte Chemie* 117, 5583-5587, doi:10.1002/ange.200500792 (2005).

13 Nightingale, A. M., Krishnadasan, S. H., Berhanu, D., Niu, X., Drury, C., McIntyre, R., Valsami-Jones, E. & deMello, J. C. A stable droplet reactor for high temperature nanocrystal synthesis. *Lab on a Chip* 11, 1221-1227, doi:10.1039/c0lc00507j (2011).

14 Nightingale, A. M., Bannock, J. H., Krishnadasan, S. H., O'Mahony, F. T. F., Haque, S. A., Sloan, J., Drury, C., McIntyre, R. & deMello, J. C. Large-scale synthesis of nanocrystals in a multichannel droplet reactor. *Journal of Materials Chemistry A* 1, 4067, doi:10.1039/c3ta10458c (2013).

15 Phillips, T. W., Lignos, I. G., Maceiczyk, R. M., deMello, A. J. & deMello, J. C. Nanocrystal synthesis in microfluidic reactors: where next? *Lab on a Chip* 14, 3172-3180, doi:10.1039/c4lc00429a (2014).

16 Omata, T., Nose, K., Otsuka-Yao-Matsuo, S., Nakamura, H. & Maeda, H. Synthesis of CdSe Quantum Dots Using Micro-Flow Reactor and Their Optical Properties. *Japanese Journal of Applied Physics* 44, 452 (2005).

17 Moghaddam, M., Baghbanzadeh, M., Sadeghpour, A., Glatter, O. & Kappe, C. O. Continuous-Flow Synthesis of CdSe Quantum Dots: A Size-Tunable and Scalable Approach. *Chemistry – A European Journal* 19, 11629-11636, doi:10.1002/chem.201301117 (2013).

18 Phillips, T. W., Lignos, I. G., Maceiczyk, R. M., deMello, A. J. & deMello, J. C. Nanocrystal synthesis in microfluidic reactors: where next? *Lab on a chip* 14, 3172-3180, doi:10.1039/c4lc00429a (2014).

19 Nightingale, A. M. & de Mello, J. C. Microscale synthesis of quantum dots. *Journal of Materials Chemistry* 20, 8454, doi:10.1039/c0jm01221a (2010).

20 Yu, W. W., Qu, L., Guo, W. & Peng, X. Experimental Determination of the Extinction Coefficient of CdTe, CdSe, and CdS Nanocrystals. *Chemistry of Materials* 15, 2854-2860, doi:10.1021/cm034081k (2003).

21 Bhunia, S. K., Saha, A., Maity, A. R., Ray, S. C. & Jana, N. R. Carbon Nanoparticle-based Fluorescent Bioimaging Probes. *Sci. Rep.* 3 (2013).

22 Chen, D., Zhao, F., Qi, H., Rutherford, M. & Peng, X. Bright and Stable Purple/Blue Emitting CdS/ZnS Core/Shell Nanocrystals Grown by Thermal Cycling Using a Single-Source Precursor. *Chemistry of Materials* 22, 1437-1444, doi:10.1021/cm902516f (2010).

23 See, G. G., Xu, L., Naughton, M. S., Tang, T. T., Bonita, Y., Joo, J., Trefonas, P., Deshpande, K., Kenis, P. J. A., Nuzzo, R. G. & Cunningham, B. T. Region specific enhancement of quantum dot emission using interleaved two-dimensional photonic crystals. *Appl Optics* 54, 2302-2308, doi:10.1364/Ao.54.002302 (2015).

24 Jang, E., Jun, S. & Pu, L. High quality CdSeS nanocrystals synthesized by facile single injection process and their electroluminescence. *Chemical Communications*, 2964-2965, doi:10.1039/b310853h (2003).

CHAPTER 3

CONTINUOUS FLOW SYNTHESIS OF ANISOTROPIC CADMIUM SELENIDE AND ZINC SELENIDE NANOPARTICLES*

3.1. Introduction

Abstract. Anisotropic semiconductor nanoparticles find use in various applications ranging from electronics (light emitting diodes, photovoltaics) to photocatalysis, biolabeling. Typically, these particles are produced via batch synthesis routes that are hampered by issues such as slow mixing, slow heating/cooling, and lack of batch-to-batch reproducibility. These issues escalate further when attempting to scale up for production. Here, we report a modular continuous flow reactor that can overcome some of the challenges encountered in a batch process. The flow reactor configuration enables air-sensitive syntheses at temperatures as high as 750 °C, supports rapid heating and cooling times (~1 s or less), and enables syntheses that involve reagents that are viscous or even solid at room temperature. To validate the modular continuous flow reactor setup, we pursued two nanomaterial systems: the synthesis of (i) CdSe nanorods and bipods, and of (ii) ZnSe nanorods. Uniform nanoparticles with low variance in quantum confined dimension (width) – 11% for ZnSe and 16% for CdSe nanorods – were obtained. For comparison, the same products were also synthesized using two batch-type approaches, hot-injection and heat-up, under similar conditions. The products synthesized via these batch processes were less uniform (variance in quantum confined dimension about 30%). Furthermore, the lack of precise

* This chapter has been adapted from the following manuscript in preparation: V. Kumar, H. A. Fuster, N. Oh, Y. Zhai, K. Deshpande, M. Shim, P.J.A. Kenis, "Continuous Flow Synthesis of Anisotropic Cadmium Selenide and Zinc Selenide Nanoparticles".

temperature control in the batch processes resulted in CdSe nanorods with irregular shaped, jagged branches whereas the CdSe from the continuous process produced uniform, straight branches. The modular continuous flow reactor design is also well suited for scale up allowing working flow rates as high as ~10 mL/min, which, for example, translate into a production rate of ~158 g per day for CdSe.

Anisotropic, rod-shaped semiconductor nanocrystals possess interesting electronic properties that depend on their size, aspect ratio and chemical composition. These nanoparticles find use in important applications such as light emitting devices[1-4], photocatalysis[5], optically induced light modulation[3,6], photovoltaics[7-12], wavefunction engineering[13], biolabeling[14], and optical memory elements[15]. In general, anisotropic semiconductor nanoparticles are considered to expand the uses of spherical nanocrystals (quantum dots) in all the aforementioned applications in which the elongated shape could in principle add new or improved properties.

In general, batch synthesis (especially hot-injection) of nanoparticles is hampered by slow mixing and heating, and suffers from batch-to-batch reproducibility[16-18]. These issues magnify further when scaling up. The desire for high throughput and superior control over particle size and quality has led to an increase in the use of continuous reactors for synthesis of these nanoparticles[17,18]. A recent review concluded that to date the majority of the literature on continuous flow synthesis of semiconductor nanoparticles has focused on Cadmium (Cd) based quantum dots[17], whereas to our knowledge work on continuous synthesis of anisotropic semiconductor nanoparticles has only been reported once[17]. The synthesis of anisotropic nanoparticles frequently requires reactants that are expensive, solid at room temperature (Trioctylphosphine oxide – TOPO and Octadecylphosphonic acid - ODPA), and/or toxic (especially Dimethyl cadmium, ODPA)[19,20]. These syntheses often also require inert conditions

for all steps - precursor preparation, precursor transfer (to the reactor), reaction, and product collection. These stringent requirements, as well as the need to heat well above the temperature typically attained with oil baths, have hindered the development of suitable continuous flow reactor systems for the synthesis of anisotropic semiconductor nanomaterials.

Previously, we have shown synthesis of multilayered Cd-based core-shell particles in an oil-bath based continuous flow reactor [21]. Although there are numerous notable works on continuous flow synthesis of anisotropic metal nanoparticles, only one account on continuous flow synthesis of semiconductor nanomaterials exists in the literature. Jin *et al.* have reported on continuous flow synthesis of SnTe nanorods[4]. However, the proposed reactor configuration in the work is not suitable for inert reactions that involve solid/viscos reactants. The operating flow rates are of the order of 0.1 mL/min that is too low for any scalable synthesis. The reactor setup uses an oil-bath that is limited by the decomposition temperature of the oil.

In this work, we demonstrate the ability to synthesize anisotropic CdSe and ZnSe nanocrystals using a modular continuous flow reactor. To overcome the challenges associated with anisotropic semiconductor nanoparticles synthesis via batch methods, we designed a modular continuous flow reactor that can withstand temperatures up to 750 °C. The reactor enables air-sensitive reactions and solid/viscous reactants as will be shown for the synthesis of ZnSe nanorods. Additionally, millifluidic dimensions allow the reactor to operate at high flow rates while maintaining rapid heating/cooling times (~1 s). Furthermore, we report on a liquid-phase synthesis procedure for the synthesis of CdSe nanorods that is not mixing-sensitive at lower temperatures, eliminating the need for preheating or in-line mixing.

The modular reactor configuration reported here can be customized easily with respect to the addition of extra reactor and cooling modules for multi-step syntheses.

Additionally, the new chemistry uses precursors that do not solidify at room temperature. The modular continuous flow reactor was also used to synthesize ZnSe nanorods using a two-step procedure which involves solid reactants, thereby exhibiting enough robustness to accommodate different syntheses.

3.2 Reactor module design, fabrication, and operation

The reactor module consists of a x-cm long stainless steel (SS) tube with an inner diameter of 2.16 mm and an outer diameter of 3.20 mm coiled tightly around a cylindrical graphite core that has a slot for a cartridge heater in its center (**Figure 3.1**). The SS coil - graphite core assembly is encased within a SS cylindrical shell, which contains three symmetrically placed slots for cartridge heaters. The cartridge heaters run through the entire length of the casing in order to ensure uniform heating. Two "end-caps" keep the SS coil in place and under tension, and thus in tight contact with the graphite core and SS casing, to ensure effective heat transfer during operation. The graphite core and the stainless steel housing were fabricated using conventional machining, thus side-stepping the tedious procedures and associated specialized facilities needed for the fabrication of previously reported silicon-glass[22], glass[23,24], and ceramic[25] continuous flow reactors.

This reactor design with a total reactant volume of 8.5 mL, allows the reactants to be heated from 25 °C to 270 °C in less than 1 s (see supporting information), which is a major improvement over conventional batch synthesis. The entire reactor module is insulated using a layer of ceramic wool and a layer of ceramic roll (Unifrax LLC). The use of long cartridge heaters that run through the entire length of the reactor, and double insulation layers prevent any hotspots in the reactor, indicated by low Biot number (10^{-6}) for the system (see SI). The temperature of the reactor is controlled via a PID controller (CSi-32k, Omega). The fabricated

reactor module was used in a configuration (**Figure 3.2**) that allows for the synthesis of anisotropic semiconductor nanoparticles involving air-sensitive reagents, as well as the use of reagents that are solid at room temperature.

For all the syntheses, the precursors were first pre-mixed in a 3-neck flask that is connected to a schlenk line. The entire setup was then brought under inert conditions by flushing the setup with nitrogen for about an hour. The precursors were then pushed in to the syringes by pressurizing the 3-neck flask via the schlenk line. The SS lines (shown in red in **Figure 3.2**) carrying the reactants to the syringe and the reactor are heated using rope heaters. The temperature of these lines is closely monitored and controlled using PID controllers (CSi-32k) and thermocouples positioned at various places along the lines. 50 mL SS syringes (KD Scientific) are used in the syntheses. PHD 2000 syringe pumps (Harvard Apparatus) are used to dispense reactants into the reactor at a set flow rate. Once the syringes were full, the precursors were then flowed through the reactor at a set flow rate ranging from 1.7 mL/min to 17 mL/min for CdSe synthesis and 0.14 mL/min to 2.4 mL/min for the synthesis of ZnSe nanorods. The reactor was run at different temperatures ranging from 190 °C to 240 °C for the synthesis of CdSe and 160 °C to 260 °C. We also varied the concentrations and relative ratios of the reagents.

The product leaving the reactor at the temperature of operation, generally above 200 °C as mentioned above, enters the cooling unit that cools the product down to a temperature in the range of 80 °C – 100 °C. The cooling module was designed to optimally cool down reaction products to a temperature such that the residual reactions are stalled, whilst simultaneously preventing any solidification of the products in the line. The module is designed along the lines of a parallel-flow heat exchanger; width and distance between the coolant (water at room temperature) and product channels were accurately determined using simulations on COMSOL

for flow rates used in the syntheses (see supporting information). The cooling module is made of copper due to its high thermal conductivity (k ~385 W/mK). A thermocouple placed close to the outlet in the cooling modules measures the temperature of the reactants as they exit the module. The product is finally collected in an air-tight. Depending on the specific synthesis being performed, this product is analyzed as is, or further purified before characterization (see below).

3.3 Continuous flow synthesis of anisotropic CdSe nanoparticles

Our initial goal was to test our continuous flow reactor in the synthesis of anisotropic CdSe nanoparticles using a non-air-sensitive procedure. Conventionally, anisotropic CdSe chemistries use Trioctylphosphine oxide (TOPO) and Octadecylphosphonic acid (ODPA) as reagents, which have the disadvantage of being toxic and solid at room temperature. Instead, we decided to use Trioctylamine (TOA) as the solvent, because it is less toxic and a liquid at room temperature, thus avoiding any solid handling or pumping issues. The precursors are comprised of Cadmium oxide (CdO) reacted with oleic acid, and Se reacted with trioctylphosphine (TOP). Stock solutions of these two precursors are prepared separately, and then appropriate amounts are introduced and mixed in the TOA solvent in the three-neck flask (**Figure 3.2**).

The Cd:Se molar ratio was kept 1 for all the syntheses in this work. The reaction conditions were varied in terms of the concentration of Cd and Se, the reaction temperature, and the residence time as discussed later. The base reaction concentration was obtained by dissolving 8 mmol of Cd and Se each in the solvent resulting in a total volume of 40 mL. The base reaction temperature and residence time were 230 °C and 3 min respectively.

TEM analysis of anisotropic CdSe particles synthesized at 230 °C and a residence time of 3 minutes (**Figure 3.4a**) shows a mixture of rods, bipods, and a few tripods and tetrapods with highly uniform arm length and width of 17±1 nm and 2.5±0.4 nm. The absorption and emission spectra for CdSe particles coated with a ZnS shell (**Figure 3.4c-d**) indicate a red shift upon the increase in the residence time, indicating the formation of bigger particles. The HRTEM image of anisotropic CdSe in **Figure 3.4b** shows lattice fringes of the synthesized CdSe bipods with fringe spacing of 0.34 nm, corresponding to the (002) planes associated with the wurtzite structure of CdSe[26]. Further, the crystal structure of CdSe rods was verified using powder X-ray diffraction analysis (**Figure 3.4e**). All the diffraction peaks match with the wurtzite crystal phase of CdSe, clearly verifying the wurtzite structure. Additionally, the sharp feature of the (002) plane in the XRD data corroborates the direction of long axis of these nanoparticles. To enhance the fluorescence output of CdSe particles, ZnS shell was grown on anisotropic CdSe nanoparticle. An effective method to grow ZnS shell [27-29] is to use a single source precursor, zinc diethyldithiocarbamate (Zn $DDTC_2$), which thermally decomposes into ZnS[28]. Use of this precursor allows for premixing of the reactants without any intermediate purification steps, consistent with the core synthesis method and compatible with potential addition of inline mixing. The amount of ZnS precursor added was calculated to be ~2 monolayers based on literature correlations[30]. TOP was used to solubilize and stabilize $ZnDDTC_2$ to create a 0.1 M concentration of $ZnDDTC_2$ in TOP. The highest photoluminescence quantum yield (PL QY) achieved after passivation was ~33% with a narrow full width at half maximum (FWHM) of 31 nm for a residence time of 2.5 minute and temperature of 230 °C. Furthermore, we noticed a large population of bipods in the product that is generally not seen in batch synthesis. The analysis of the TEM images revealed that on average ~44% of the particles are bipods, ~45%

nanorods, and ~11% tripods/tetrapods. Details of the shape analysis are mentioned in the Supplementary Information. To compare the quality of the products with comparable conventional batch synthesis techniques, we performed hot-injection and heat-up syntheses at similar conditions (230 °C, 3 min) and precursor concentrations in a batch reactor (10 mL). We found that the heat-up synthesis had the worst size distribution (length: 12.35±4.13 nm, width: 1.9±0.7 nm). Hot injection technique with a length and width distribution of 19.28±3.7 nm and 1.8±0.53 nm produced more uniform particles than heat-up method. Continuous flow reactor produced the most uniform product amongst the three synthesis techniques. We attribute such a tight control on product size in our continuous flow reactor to precise temperature control including fast heating/cooling times and temporally stable temperature within the reactor compared to batch reactors. Even in the case of the hot-injection technique, the solution temperature fluctuates by ~10 °C after the injection of cold precursor in the hot bath for a long time before coming to a constant (SI) as shown in **Figure 3.3**. Furthermore, we observed that the proportion of bipods in the product was the highest in the continuous flow reactor, followed by hot- injection and heat-up methods. This leads us to believe that the final morphology of the nanoparticles is affected by the heating time of the reagents, which is the fastest in the continuous flow reactor followed by hot-injection and heat-up techniques[31,32]. Faster heating times in the flow reactor lead to smaller zinc-blende cores (< 1 nm). Small cores allow for not more than 2 branches to grow due to steric hindrance[33]. Therefore, rapid heating times in the continuous flow reactor enables us to synthesize kinetic products that is not possible with comparable batch reactors. Additionally, we noticed jagged branches in the hot-injection synthesis products as opposed to uniform straight branches synthesized in the continuous flow reactor. Dominance of anisotropic particles in reactions conducted at lower temperature implies

a change from predominantly thermodynamic control to predominantly kinetic control at the temperature range around 230-250^{o}C[34-36]. Therefore, the presence of jagged branches in the hot-injection method can be attributed to the formation of alternate sections of zinc blende[37] and wurtzite due to temperature fluctuations of around 10 °C. Therefore, stable temperature in the continuous flow reactor aids formation of more uniform products compared to similar batch synthesis techniques. To demonstrate the control on emission wavelengths, we varied the process parameters including, temperature, residence time, and concentration of the precursors. **Figure 3.5** shows the effect of temperature, residence time, and concentration of the reagents on the photoluminescence quantum yield (PL QY) and the emission peak position of the synthesized CdSe nanoparticles. As expected, the emission wavelength of the products red-shifted with an increase in the reaction temperature, indicating bigger particle size. However, PL QY remained relatively unaffected by the reaction temperature post 210 °C. The higher residence times resulted in bigger particles that is reflected by the red-shift of the peaks. However, an increase in the residence time was accompanied by a steady decrease in PL QY. In addition, PL QY was found to be relatively independent of the reagent concentration at low concentrations but dropped drastically at high concentrations. Higher concentrations led to particles with smaller diameter in the final product as indicated by the blue-shifted emission peaks. This trend can be explained using the fact that a higher concentration of precursors leads to a higher concentration of nuclei. Higher the number of nuclei, lesser is the amount of precursor available to each nuclei for growth and hence the smaller size of the final product[31,38]. Note that 1x denotes the base concentration mentioned in the experimental section. The notation #x (**Figure 3.5c**) denotes that the concentration of both the cationic and the anionic reagents used in the synthesis was # times the base concentration.

Reactor yields: Reactor yields are seldom reported in the literature. However, we believe that such a metric will be particularly useful when considering scale-up options for continuous reactors. We developed a protocol to accurately estimate the reactor yield using Inductively Coupled Plasma-Optical Emission Spectrometry (Supporting Information). The highest conversion of about 81% was found for a reaction temperature of 240 °C and a residence time of 3 min. Based on this result, we calculated that our reactor can produce about 158 g of anisotropic CdSe nanoparticles per day (24 h)[39]. However, reactor yield can be further improved by optimizing concentration, temperature, and residence time. To demonstrate the wide range of applicability of the reactor, we shifted our focus to Cd-free anisotropic nanomaterials that require high-temperature syntheses involving inert conditions and solid/viscous reactants. ZnSe (nanorods) was an obvious choice since there is no account of the synthesis of ZnSe nanorods in a continuous flow reactor.

3.4 Continuous flow synthesis of ZnSe nanorods

ZnSe nanorods were synthesized using a two-step synthesis suggested by Acharya *et al.*[40]. In the first step, ZnSe nanowires were synthesized. The nanowires were then ripened at a higher temperature to yield nanorods. Transformation of nanowires to nanorods takes place as a consequence of inter and intra particle ripening[40,41]. Monomers from the tips of the nanowires preferentially dissolve into the solution and get re-deposited on sides. This effective redistribution of material happens due to the fact that the end facets of the long axis are the least stable regions in a nanowire[42,43]. We found that an intermediate purification step between the nanowire and the nanorod steps resulted in the reduction of the unconverted nanowires (**Figure 3.6a-b**). This is explained by the fact that excess monomers in the solution hinder the ripening step that is required for the formation of the nanorods[41,44]. HRTEM image of a ZnSe nanorod in

Figure 3.6b shows lattice fringes of the synthesized ZnSe nanorods with a fringe spacing of 0.31 nm, corresponding to the (002) plane associated with the wurtzite structure. The absorption spectrum for ZnSe nanowires (**Figure 3.6c**) contains dual peaks at 327 nm and 345 nm that are indicative of magic sized ZnSe nanowires[2,45-47]. The absorption peak for the nanorods (**Figure 3.6d**) red-shifted to around 405 nm. These absorption spectra confirm the presence of ZnSe nanowires and nanorods[2,40,41,46]. Synthesizing ZnSe nanonrods of uniform length is challenging especially since the ripening process, by its very nature, is size defocusing. Furthermore, fragmentation of nanowires takes place in the high temperature ripening stage that leads to formation of non-uniform strands of ZnSe nanorods[41]. The synthetic approach produced nearly monodisperse ZnSe nanorods with an average width and length of 2.3±0.2 nm and 13.4±1.7 nm, respectively (**Figure 3.6e-f**). A different set of conditions was tested by varying both the residence time and the temperature of the ripening stage. High temperatures or high residence times alone led to over ripening of nanowires producing big particles of irregular shapes. Additionally, a combination of high temperatures and long residence times led to decomposition of ZnSe nanowires. Similarly, the combination of short residence times and low temperatures yielded under-ripened nanowires resulting in many unconverted nanowires in the final product. A fine balance between both process parameters, i.e. temperature and residence time, is required to produce monodisperse ZnSe nanorods. Results from ICP-OES indicated a Se-rich product with Se/Zn ratio slightly greater than 1 (Supplementary information). Details about the operation of the inert setup are outlined in the Supporting Information.

3.5 Conclusions

In summary, we reported the first instance of continuous flow synthesis of anisotropic CdSe and ZnSe (Cd-free) nanoparticles in a millifluidic continuous flow reactor. CdSe nanoparticles were

synthesized at an estimated high throughput of 158 g/day. No glove box or schlenk line is required for the preparation of anisotropic CdSe nanoparticles. Additionally, the synthesis developed here has an advantage of being an all-liquid chemistry at room temperature that is much easier to implement on a continuous flow reactor. Furthermore, the synthesis does not involve any toxic and expensive reagents like TOPO and ODPA. The millifluidic reactor allowed us to operate at flow rates of higher than 10 mL/min (more suitable for scaling up) without incurring high pressure drop.

The millifluidic reactor setup was further modified to enable high temperature, air-sensitive reactions involving solid/viscous reactants, thereby making the reactor robust enough to accommodate a wide range of chemistries. We demonstrated the capability by synthesizing ZnSe nanorods on the modified reactor setup. All the steps, including precursor preparation, transfer, and the reaction, were carried out under inert conditions. Additionally, the new setup eliminated any hassle of manually loading or unloading syringe carefully with air-sensitive reactants, which makes the process suitable for scaling out. We were therefore able to overcome the challenges associated with the conventional flow reactors to successfully synthesize monodisperse ZnSe on a continuous scale for the first time.

Future work in the area of anisotropic CdSe nanoparticles would focus on improving quantum yield and obtaining optimized process conditions to attain higher shape selectivity. Easy fabrication process will enable quick and fast manufacturing of custom reactors that will be extremely beneficial in scaling up the production process of nanoparticles In the area of ZnSe nanorods, future efforts would focus on obtaining a more monodisperse final product. The current strategy banks on transforming nanowires to nanorods via an Ostwald ripening process.

The method, by its very nature is unsuitable for achieving high size uniformity. Any alternate synthesis procedure that by passes the ripening step may enhance product size dispersity greatly.

.

3.6 Materials and Methods

Cadmium oxide (99.5%), selenium (99.99%), oleic acid (90%), oleylamine (70%), trioctylphosphine (TOP) (90%), trioctylamine (98%), zinc stearate (technical grade), and zinc diethyldithiocarbamate ($ZnDDTC_2$) (97%) were purchased from Sigma-Aldrich and used as received. Unless otherwise stated, the CdSe nanorod synthesis used 0.1028 g CdO (0.8 mmol) dissolved in 2.0 mL of oleic acid at 200°C forming a clear solution. For synthesis of CdSe nanorods, TOP-Se solution was created by mixing 1.1844 g Se with 15 mL TOP in a glovebox before dissolving via sonication. For a standard synthesis, the Cd oleate solution (0.4 M Cd) and 0.8 mL of the anion solution (1 M Se) was mixed with 40 mL TOA and pumped through the reactor, which was held at 220 °C with standard residence times (reactor volume / volumetric flow rate) of two and one half minutes (base case conditions).

For ZnS shell growth on CdSe, a standard stock solution of 0.0724 g $ZnDDTC_2$ dissolved in 20 mL of TOP was used. Standard shell addition amounts were 0.7 mL of the $ZnDDTC_2$ solution in TOP mixed with 1.6 mL of oleylamine (as a sacrificial amine for the $ZnDDTC_2$ decomposition) and 10 mL of reacted nanorod solution. The reactants were mixed in a three-necked flask under nitrogen and pumped through the tube reactor at 110°C for thirty minutes.

Unless otherwise stated, Zinc selenide nanorod synthesis used the method suggested by Acharya *et al.*[45]. Nanowires were synthesized using 0.2035 g of selenium dissolved in 26 mL of oleylamine, which was subjected to three cycles of vacuum and nitrogen purges for about 1 hour

at room temperature to remove oxygen. This selenium precursor solution was then heated to 200 °C under nitrogen forming a clear solution and subsequently cooled to around 70 °C. Zinc stearate solution used as the zinc precursor was made by dissolving 0.8407 g of zinc stearate in 13 mL of oleylamine at 150 °C. The zinc stearate solution was mixed with the selenium solution under nitrogen at 60 °C. The nanowire synthesis was performed at 160 °C with a residence time of thirty minutes. Purification was performed following the nanowire synthesis by centrifugation with a solution of 70:30 ethanol:methanol mixture. Following purification, the purified nanowire solution was diluted to its original volume with additional oleylamine. Nanorod synthesis occurred by running the purified nanowire solution through the reactor at a temperature of 260 °C and a residence time of 3 minutes.

Mixing sensitivity. The mixing for CdSe experiments was done offline by mixing the Cd and Se precursors in a three-neck flask; subsequently, the experiment was conducted by using a syringe pump to pump the mixture. For this synthesis, the reactants appear to have minimal sensitivity to mixing time at room temperature; spectra of a Cd + Se reagent mixture left overnight at room temperature yielded no fluorescence or particle formation. Based on this result, mixing could be done on a larger scale over the course of hours, simplifying reactor design and minimizing the need for inline mixers. For the purposes of this study, cold offline mixing appears equivalent to cold inline mixing, allowing for the heating up method where the premixed reactants are rapidly heated to the reaction temperature.

Characterization. The solutions were typically diluted 1:40 in chloroform to obtain absorbance between 0.02 and 0.05 absorbance units (substantial additional dilution was required for some samples) and absorption/PL spectra were measured in solution without additional purification or

size selection. Absorption spectra were obtained from an Agilent 8453 UV-Vis Diode Array System spectrophotometer and PL spectra were obtained from a Horiba Jobin-Yvon Fluoromax-3 spectrofluorimeter. A 490 nm excitation wavelength was used for CdSe particles and 350 nm for ZnSe particles for PL measurements. Relative PL QYs were determined by comparing to a quinine sulfate solution in 0.1 M H_2SO_4 (58% quantum yield). For TEM, ICP-OES and XRD measurements, the reaction products were thoroughly washed with 70:30 ethanol:methanol mixture and the precipitate was collected using a centrifuge. The purified products were then redissloved in choloroform for TEM imaging. Also, parts of the redissolved products were dried for ICP-OES and XRD measurements. ICP-OES were obtained on a PerkinElmer 2000DV optical emission spectrometer. Powder X-ray diffraction patterns were collected using a Bruker D8 Venture equipped with a four-circle κ diffractometer and a photon 100 detector.

Acknowledgements

The manuscript was written through contributions of all authors. All authors have given approval to the final version of the manuscript. We gratefully acknowledge financial support from the Dow Chemical Company for research agreement #226772AC and a graduate fellowship to VK. We thank Dr. Pete Trefonas, Dr. Jieqian Zhang, Dr. Jong Park, Dr. Kevin Howard for stimulating discussions. We also acknowledge Mike Harland for providing critical inputs on designing and fabrication of the reactor setup.

3.7 Figures

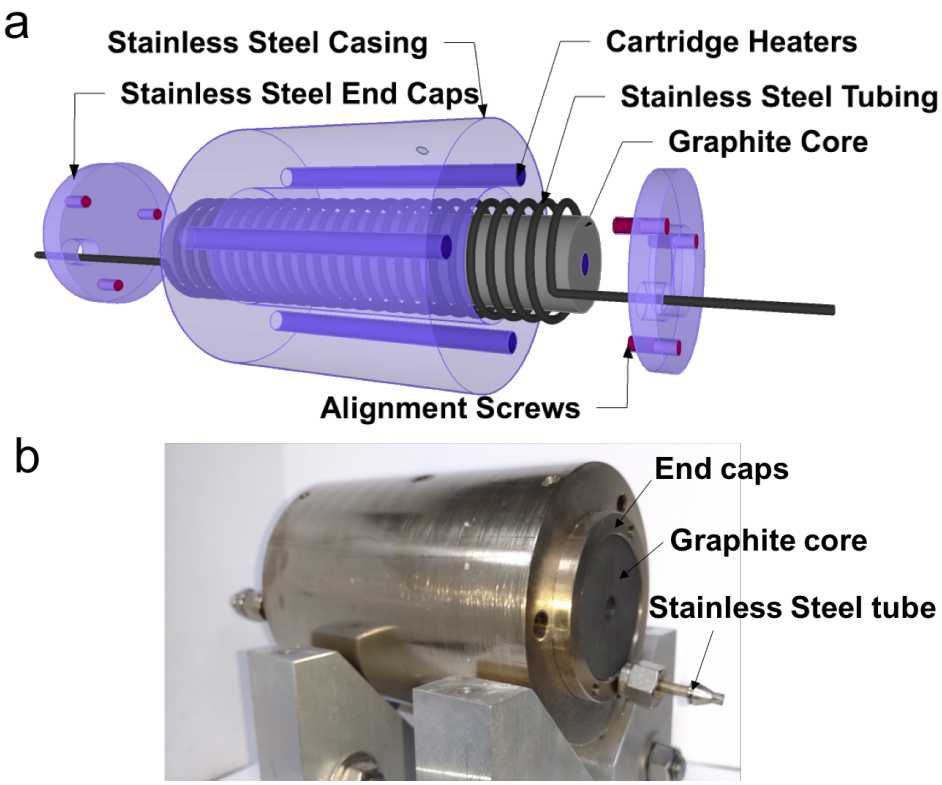

Figure 3.1. (a) Schematic of the reactor module (not drawn to scale), which consists of a stainless steel coil, wrapped around a graphite core, which is inserted into a stainless steel housing that hosts three symmetrically placed cartridge heaters. The fourth cartridge heater goes through the middle of the graphite core. End caps hold the stainless steel coil in place and under tension during operation. **(b)** Photograph of the stainless steel reactor module.

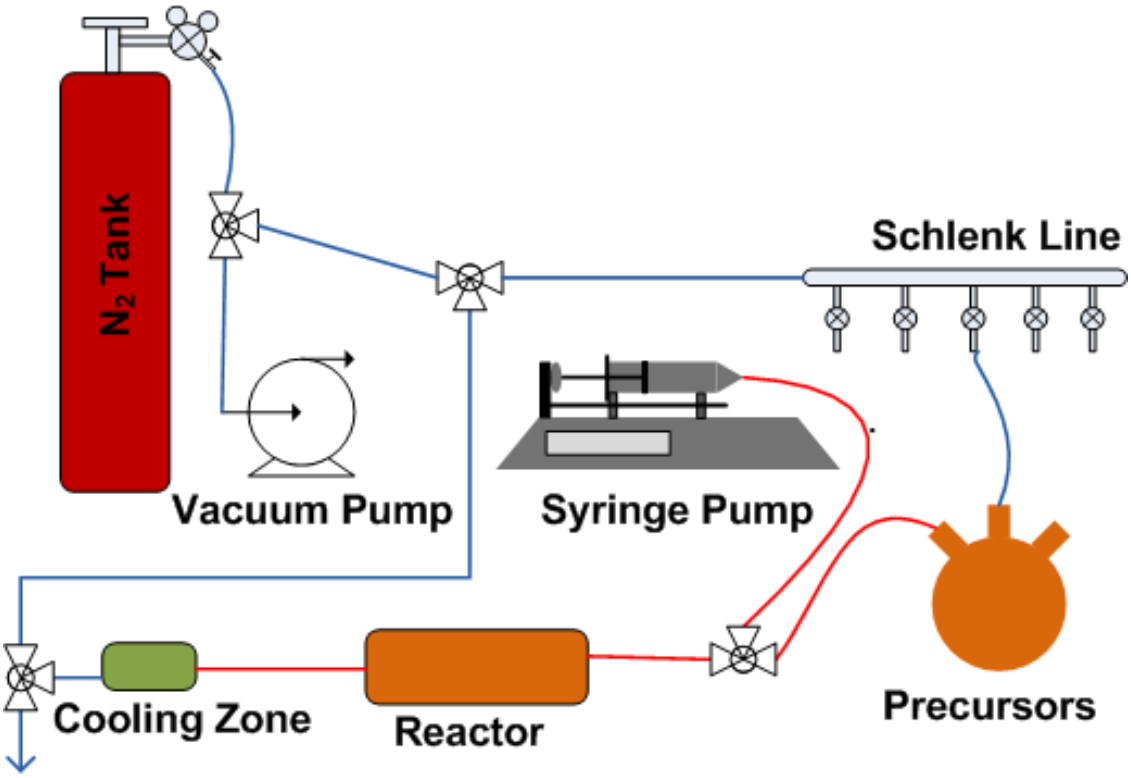

Figure 3.2. Schematic of the flow reactor setup that enables continuous synthesis of anisotropic semiconductor nanoparticles via high temperature and air-sensitive reactions containing solid/viscos reactants. The Red lines indicate heated lines whose temperature was precisely controlled. The Blue lines indicate the lines carrying the reactants at room temperature. The precursors are premixed in a three-neck flask under inert condition. The three-neck flask is then pressurized with nitrogen to transfer the reactants to the syringe pump, which is then used to flow the precursors through the reactor at a desired flow rate. The temperature of products flowing out of the reactor was quickly quenched with the use of a cooling unit downstream of the reactor module to check any residual reactions.

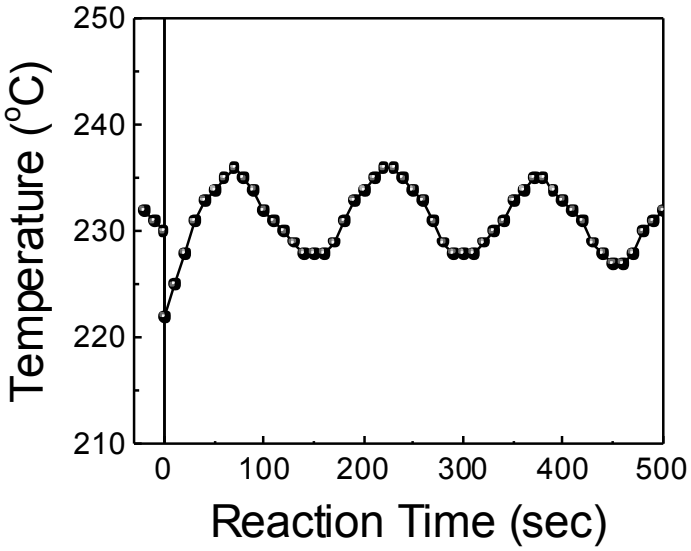

Figure 3.3. Temporal temperature profile for a typical hot-injection technique. Time = 0 s denotes the instant when the cold precursor is injected into the hot solution at a set temperature (230 °C in this case). The temperature of the solution drops quickly after the hot-injection. The temperature of the solution fluctuates by about ~10 °C for over 500 s before stabilizing. The temperature fluctuations can lead to non-uniform products at best and completely different morphologies at worst.

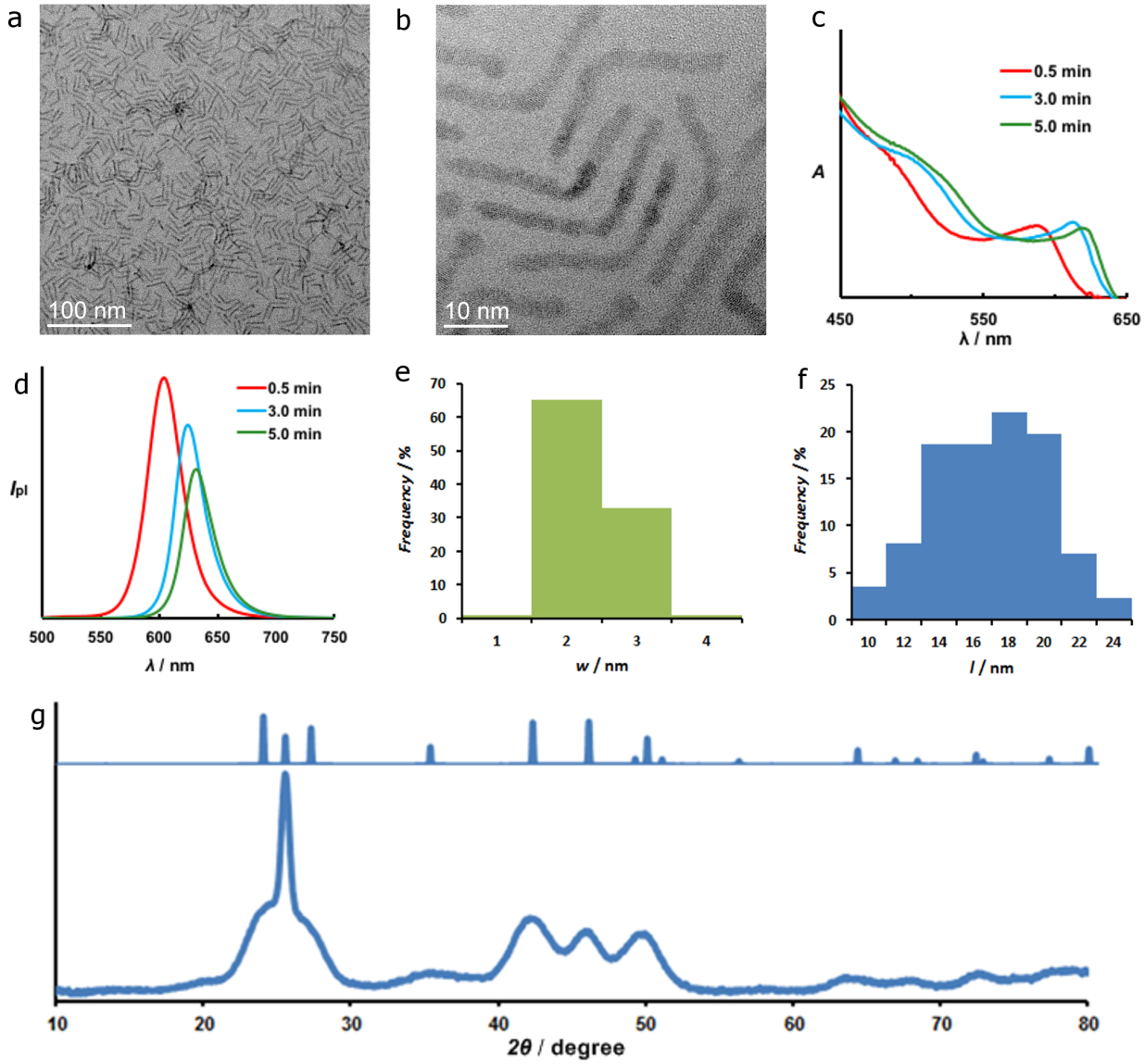

Figure 3.4. (a) TEM image of anisotropic CdSe particles synthesized in the continuous flow reactor at 230 °C and 3 min. **(b)** HRTEM image shows a lattice constant of 3.4 A° corresponding to (002) plane that is indicative of CdSe wurtzite structure in the product. **(c)** Absorption and **(d)** emission spectra (absorption normalized) of the synthesized CdSe particles for different residence times of 0.5 min, 3 min and 5 min. CdSe particles were further coated with a shell of ZnS. The associated **(e)** length and **(f)** width distributions of the sample shown in (a) indicate a fairly uniform size of the particles with an average width and length of 2.5±0.4 nm and 17±3.2 nm. 87 particles were analysed to obtain the size distributions. **(g)** Powder XRD patterns of the synthesized CdSe particles indicate hexagonal wurtzite structure. The broad band at 25° is due to Trioctylamine/TOP ligand. The standard pattern for hexagonal wurtzite for CdSe is given for reference.

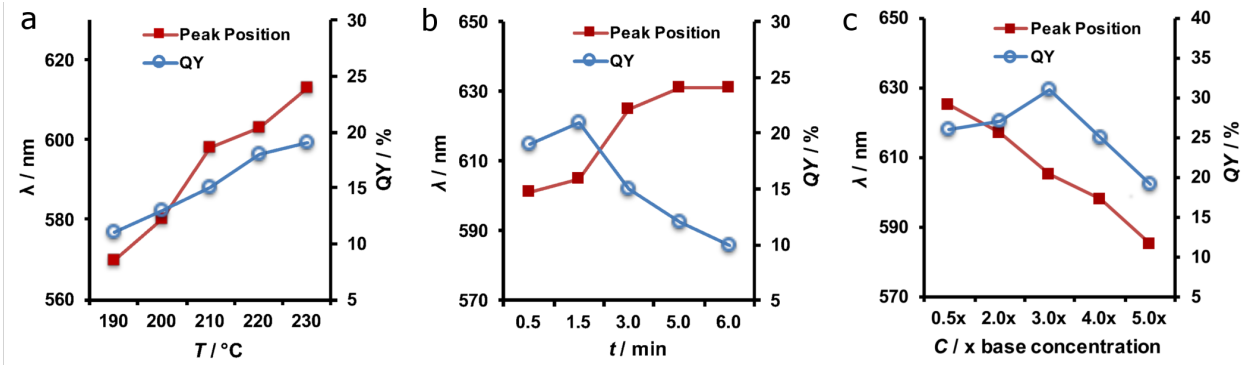

Figure 3.5. (a) Temperature sweep, **(b)** time sweep, and **(c)** concentration sweep were performed to analyse the effects of process parameters on the product quantum Yield (QY) and emission wavelength (λ). Unless stated, the synthesis conditions were kept same as the base case (mentioned in the experimental section) except the parameter for which the sweep was done

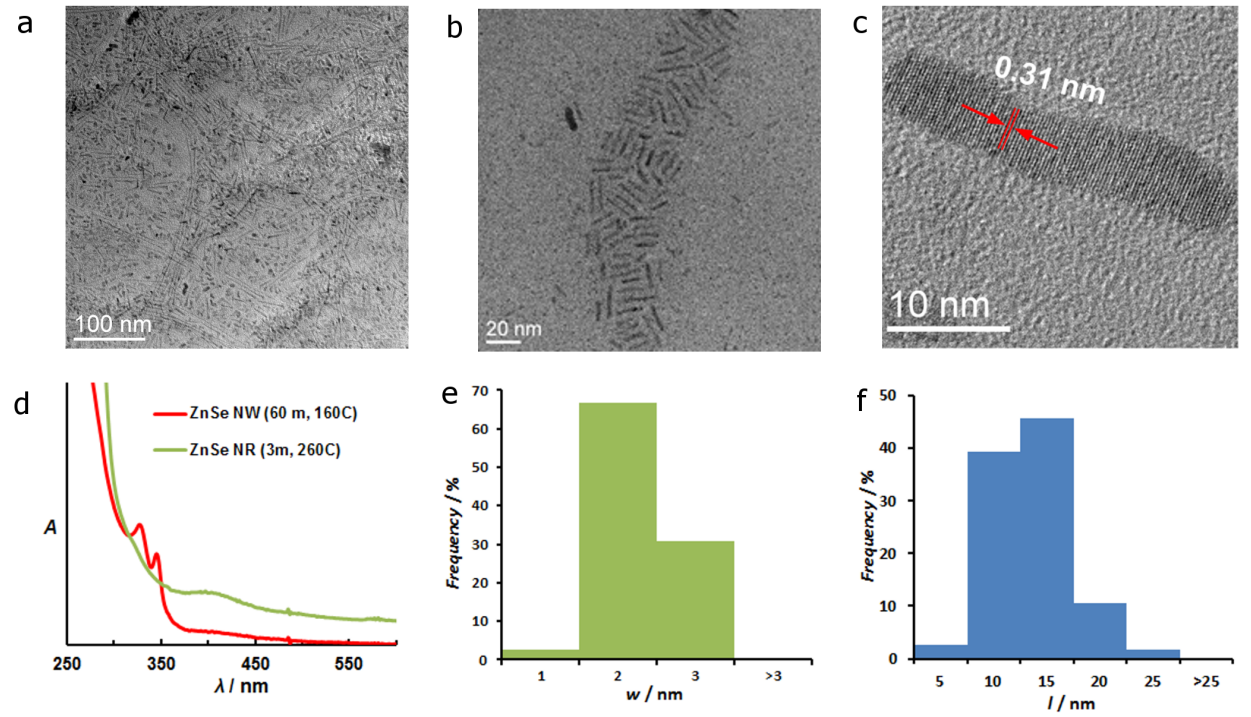

Figure 3.6. TEM images of **(a)** ZnSe nanowire/nanorod mixture obtained from ripening of unpurified nanowire product and **(b)** ZnSe nanorods. Also shown is an **(c)** HRTEM image of the ZnSe nanorods with distinct lattice fringes. Nanowires were synthesized in the continuous flow reactor at 160 °C for a residence time of 60 min. The nanowire product was then purified, redissolved in Oleylamine, and flowed through the reactor at 260 °C for a residence time of 3 min to yield nanorods shown in (b). Absorption spectra of synthesized ZnSe nanowires (160 °C, 60 min) and nanorods (260 °C, 3 min) are shown in **(d)**. ZnSe nanowires exhibit two peaks at 327 nm and 345 nm, indicating presence of magic-size ZnSe nanowires. The associated length and width distributions of the sample in (b) are shown in **(e)** and **(f)** respectively. Nanorods have an average length and width of 13.4±1.8 nm and 2.3±0.2 nm respectively.114 particles were analyzed to obtain the size distributions.

3.8 References

1 Oh, N., Nam, S., Zhai, Y., Deshpande, K., Trefonas, P. & Shim, M. Double-heterojunction nanorods. *Nat Commun* 5, doi:10.1038/ncomms4642 (2014).

2 Zhang, L. J., Chen, F. Y., Tong, J. Z., Chen, G. D., Huang, H. J. & Shen, X. C. Controlled Growth of ZnSe Nanocrystals by Tuning Reactivity and Amount of Zinc Precursor. *J Chem-Ny*, doi:Artn 791437Doi 10.1155/2013/791437 (2013).

3 Nam, S., Oh, N., Zhai, Y. & Shim, M. High efficiency and optical anisotropy in double-heterojunction nanorod light-emitting diodes. *Acs Nano* 9, 878-885, doi:10.1021/nn506577p (2015).

4 Jin, H. D. & Chang, C. H. Continuous synthesis of SnTe nanorods. *Journal of Materials Chemistry* 21, 12218-12220, doi:10.1039/c1jm12211h (2011).

5 Hewa-Kasakarage, N. N., El-Khoury, P. Z., Tarnovsky, A. N., Kirsanova, M., Nemitz, I., Nemchinov, A. & Zamkov, M. Ultrafast Carrier Dynamics in Type II ZnSe/CdS/ZnSe Nanobarbells. *Acs Nano* 4, 1837-1844, doi:Doi 10.1021/Nn100229x (2010).

6 Petti, L., Rippa, M., Fiore, A., Manna, L. & Mormile, P. Optically induced light modulation in an hybrid nanocomposite system of inorganic CdSe/CdS nanorods and nematic liquid crystals. *Opt Mater* 32, 1011-1016, doi:Doi 10.1016/J.Optmat.2010.02.022 (2010).

7 Celik, D., Krueger, M., Veit, C., Schleiermacher, H. F., Zimmermann, B., Allard, S., Dumsch, I., Scherf, U., Rauscher, F. & Niyamakom, P. Performance enhancement of CdSe nanorod-polymer based hybrid solar cells utilizing a novel combination of post-synthetic nanoparticle surface treatments. *Sol Energ Mat Sol C* 98, 433-440, doi:Doi 10.1016/J.Solmat.2011.11.049 (2012).

8 Alivisatos, A. P. Hybrid-nanorod polymer solar cells. *Abstr Pap Am Chem S* 233 (2007).

9 Alivisatos, A. P. Hybrid-nanorod polymer solar cells. *Abstr Pap Am Chem S* 227, U1240-U1240 (2004).

10 Huynh, W. U., Dittmer, J. J. & Alivisatos, A. P. Hybrid nanorod-polymer solar cells. *Science* 295, 2425-2427, doi:Doi 10.1126/Science.1069156 (2002).

11 Kim, S., Fisher, B., Eisler, H. Y. & Bawendi, M. G. Novel type-II quantum dots: CDTE/CDSE(core/shell) and CDSE/ZNTE(core/shell) heterostructures. *Abstr Pap Am Chem S* 224, U443-U443 (2002).

12 Farva, U. & Park, C. Colloidal synthesis and air-annealing of CdSe nanorods for the applications in hybrid bulk hetero-junction solar cells. *Materials Letters* 64, 1415-1417, doi:Doi 10.1016/J.Matlet.2010.03.026 (2010).

13 Muller, J., Lupton, J. M., Lagoudakis, P. G., Schindler, F., Koeppe, R., Rogach, A. L., Feldmann, J., Talapin, D. V. & Weller, H. Wave function engineering in elongated semiconductor nanocrystals with heterogeneous carrier confinement. *Nano Lett* 5, 2044-2049, doi:Doi 10.1021/Nl051596x (2005).

14 Deka, S., Quarta, A., Lupo, M. G., Falqui, A., Boninelli, S., Giannini, C., Morello, G., De Giorgi, M., Lanzani, G., Spinella, C., Cingolani, R., Pellegrino, T. & Manna, L. CdSe/CdS/ZnS Double Shell

Nanorods with High Photoluminescence Efficiency and Their Exploitation As Biolabeling Probes. *J Am Chem Soc* 131, 2948-2958, doi:Doi 10.1021/Ja808369e (2009).

15 Kraus, R. M., Lagoudakis, P. G., Rogach, A. L., Talapin, D. V., Weller, H., Lupton, J. M. & Feldmann, J. Room-temperature exciton storage in elongated semiconductor nanocrystals. *Phys Rev Lett* 98, 017401 (2007).

16 Yang, H., Luan, W., Wan, Z., Tu, S.-t., Yuan, W.-K. & Wang, Z. M. Continuous Synthesis of Full-Color Emitting Core/Shell Quantum Dots via Microreaction. *Crystal Growth & Design* 9, 4807-4813, doi:10.1021/cg900652y (2009).

17 Nightingale, A. M. & de Mello, J. C. Microscale synthesis of quantum dots. *Journal of Materials Chemistry* 20, 8454, doi:10.1039/c0jm01221a (2010).

18 Phillips, T. W., Lignos, I. G., Maceiczyk, R. M., deMello, A. J. & deMello, J. C. Nanocrystal synthesis in microfluidic reactors: where next? *Lab on a chip* 14, 3172-3180, doi:10.1039/c4lc00429a (2014).

19 Peng, X. Green Chemical Approaches toward High-Quality Semiconductor Nanocrystals. *Chemistry – A European Journal* 8, 334-339, doi:10.1002/1521-3765(20020118)8:2<334::AID-CHEM334>3.0.CO;2-T (2002).

20 Sengül, H. & Theis, T. L. 37 Life Cycle Inventory of Semiconductor Cadmium Selenide Quantum Dots for Environmental Applications. (2009).

21 Naughton, M. S., Kumar, V., Bonita, Y., Deshpande, K. & Kenis, P. J. High temperature flow synthesis of CdSe/CdS/ZnS, CdS/ZnS, and CdSeS/ZnS nanocrystals *Nanoscale*, doi:10.1039/C5NR04510J (2015).

22 Jensen, K. F. Microreaction engineering - is small better? *Chem Eng Sci* 56, 293-303, doi:Doi 10.1016/S0009-2509(00)00230-X (2001).

23 Watts, P. & Haswell, S. J. The application of micro reactors for organic synthesis. *Chemical Society reviews* 34, 235-246, doi:10.1039/b313866f (2005).

24 Haswell, S. J., Middleton, R. J., O'Sullivan, B., Skelton, V., Watts, P. & Styring, P. The application of micro reactors to synthetic chemistry. *Chemical communications*, 391-398, doi:Doi 10.1039/B008496o (2001).

25 Knitter, R., Gohring, D., Risthaus, P. & Hausselt, J. Microfabrication of ceramic microreactors. *Microsystem Technologies* 7, 85-90, doi:Doi 10.1007/S005420100107 (2001).

26 Thoma, S. G., Sanchez, A., Provencio, P. P., Abrams, B. L. & Wilcoxon, J. P. Synthesis, optical properties, and growth mechanism of blue-emitting CdSe nanorods. *J Am Chem Soc* 127, 7611-7614, doi:10.1021/ja050501q (2005).

27 Trindade, T., O'Brien, P. & Zhang, X.-m. Synthesis of CdS and CdSe Nanocrystallites Using a Novel Single-Molecule Precursors Approach. *Chemistry of Materials* 9, 523-530, doi:10.1021/cm960363r (1997).

28 Dethlefsen, J. R. & DÃ¸ssing, A. Preparation of a ZnS Shell on CdSe Quantum Dots Using a Single-Molecular ZnS Precursor. *Nano Lett* 11, 1964-1969, doi:10.1021/nl200211n (2011).

29 Wang, H., Nakamura, H., Uehara, M., Yamaguchi, Y., Miyazaki, M. & Maeda, H. Highly Luminescent CdSe/ZnS Nanocrystals Synthesized Using a Single-Molecular ZnS Source in a Microfluidic Reactor. *Advanced Functional Materials* 15, 603-608, doi:10.1002/adfm.200400164 (2005).

30 Yu, W. W., Qu, L., Guo, W. & Peng, X. Experimental Determination of the Extinction Coefficient of CdTe, CdSe, and CdS Nanocrystals. *Chemistry of Materials* 15, 2854-2860, doi:10.1021/cm034081k (2003).

31 Abe, S., Capek, R. K., De Geyter, B. & Hens, Z. Tuning the Postfocused Size of Colloidal Nanocrystals by the Reaction Rate: From Theory to Application. *Acs Nano* 6, 42-53, doi:10.1021/nn204008q (2012).

32 Park, J., Joo, J., Kwon, S. G., Jang, Y. & Hyeon, T. Synthesis of monodisperse spherical nanocrystals. *Angew Chem Int Edit* 46, 4630-4660, doi:10.1002/anie.200603148 (2007).

33 McDaniel, H. & Shim, M. Size and Growth Rate Dependent Structural Diversification of Fe3O4/CdS Anisotropic Nanocrystal Heterostructures. *Acs Nano* 3, 434-440, doi:10.1021/nn800737a (2009).

34 Lim, J., Jun, S., Jang, E., Baik, H., Kim, H. & Cho, J. Preparation of highly luminescent nanocrystals and their application to light-emitting diodes. *Advanced materials* 19, 1927-+, doi:10.1002/adma.200602642 (2007).

35 Yong, K. T., Sahoo, Y., Swihart, M. T. & Prasad, P. N. Shape control of CdS nanocrystals in one-pot synthesis. *J Phys Chem C* 111, 2447-2458, doi:10.1021/jp066392z (2007).

36 Yeh, C. Y., Lu, Z. W., Froyen, S. & Zunger, A. Zinc-Blende-Wurtzite Polytypism in Semiconductors. *Phys Rev B* 46, 10086-10097, doi:DOI 10.1103/PhysRevB.46.10086 (1992).

37 Grebinski, J. W., Hull, K. L., Zhang, J., Kosel, T. H. & Kuno, M. Solution-based straight and branched CdSe nanowires. *Chemistry of Materials* 16, 5260-5272, doi:10.1021/cm048498h (2004).

38 Bullen, C. R. & Mulvaney, P. Nucleation and growth kinetics of CdSe nanocrystals in octadecene. *Nano Lett* 4, 2303-2307, doi:Doi 10.1021/Nl0496724 (2004).

39 Lévesque, F. & Seeberger, P. H. Continuous-Flow Synthesis of the Anti-Malaria Drug Artemisinin. *Angewandte Chemie International Edition* 51, 1706-1709, doi:10.1002/anie.201107446 (2012).

40 Acharya, S., Sarkar, S. & Pradhan, N. Material Diffusion and Doping of Mn in Wurtzite ZnSe Nanorods. *The Journal of Physical Chemistry C* 117, 6006-6012, doi:10.1021/jp400456t (2013).

41 Jia, G. & Banin, U. A General Strategy for Synthesizing Colloidal Semiconductor Zinc Chalcogenide Quantum Rods. *J Am Chem Soc* 136, 11121-11127, doi:10.1021/ja505541q (2014).

42 Peng, X. & Peng, Z. A. Mechanisms of shape evolution of CdSe nanocrystals. *J Am Chem Soc* 123, doi:10.1021/ja0027766 (2001).

43 Peng, X. & Peng, Z. A. Nearly Monodisperse and Shape-Controlled CdSe Nanocrystals via Alternative Routes: Nucleation and Growth. *J Am Chem Soc* 124, doi:10.1021/ja0173167 (2002).

44 Jia, G. H., Sitt, A., Hitin, G. B., Hadar, I., Bekenstein, Y., Amit, Y., Popov, I. & Banin, U. Couples of colloidal semiconductor nanorods formed by self-limited assembly. *Nature materials* 13, 302-308, doi:Doi 10.1038/Nmat3867 (2014).

45 Panda, A. B., Acharya, S. & Efrima, S. Ultranarrow ZnSe Nanorods and Nanowires: Structure, Spectroscopy, and One-Dimensional Properties. *Advanced materials* 17, 2471-2474, doi:10.1002/adma.200500551 (2005).

46 Chin, P. T. K., Stouwdam, J. W. & Janssen, R. A. J. Highly Luminescent Ultranarrow Mn Doped ZnSe Nanowires. *Nano Lett* 9, 745-750, doi:10.1021/nl8033015 (2009).

47 Panda, A. B., Acharya, S., Efrima, S. & Golan, Y. Synthesis, Assembly, and Optical Properties of Shape- and Phase-Controlled ZnSe Nanostructures. *Langmuir : the ACS journal of surfaces and colloids* 23, 765-770, doi:10.1021/la061633f (2006).

3.9 Supplementary information

COMSOL simulations indicate fast heating (< 1 s)

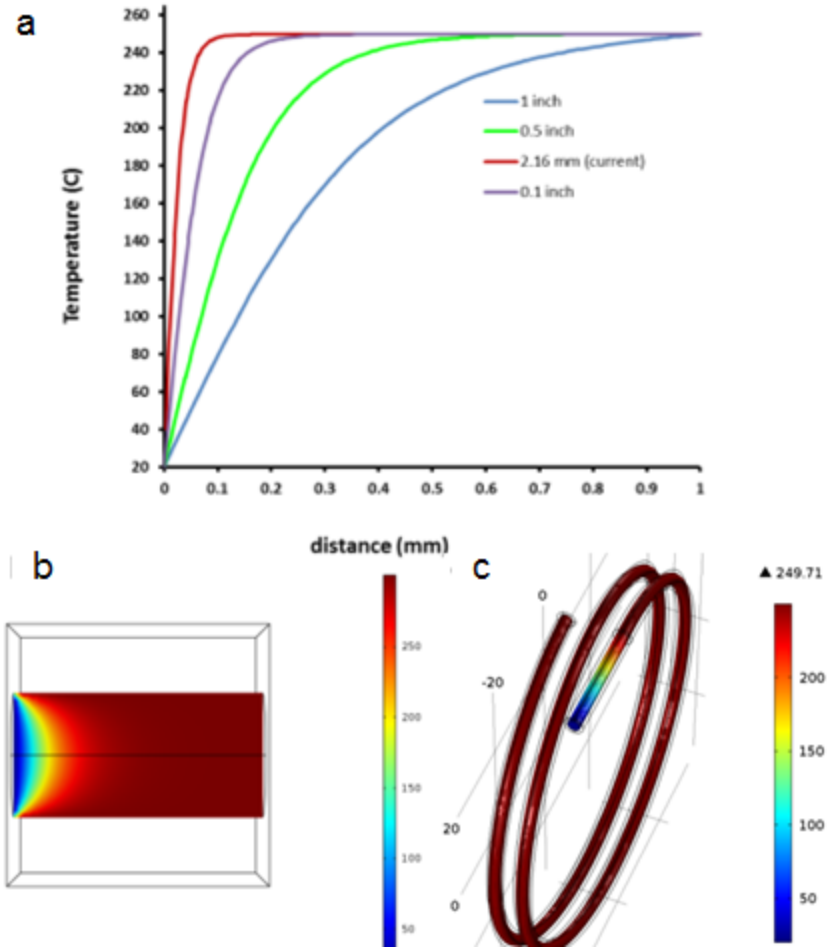

Figure 3.7. (a) Centerline temperature profiles of the reactants inside stainless steel tubing for different diameters based on COMSOL simulations. **(b)** Surface temperature of reactants flowing through a stainless steel tubing of ID 2.16 mm. The inlet temperature of the reactants was set at 20 °C and the wall temperature of the tubing (in equilibrium with the stainless steel casing temperature) was set at 250 °C for all simulations. Heating time of around ~400 ms was achieved in the simulation. **(c)** Temperature profile of reactants inside the stainless steel tubing with a part of the tubing (near the reactant entry point) exposed to air, and therefore there is some preheating of the reactants before it enters the heating zone. The simulation accurately represents the conditions in the hood in which the reactor setup was used.

Reactor schematic and fabricated parts

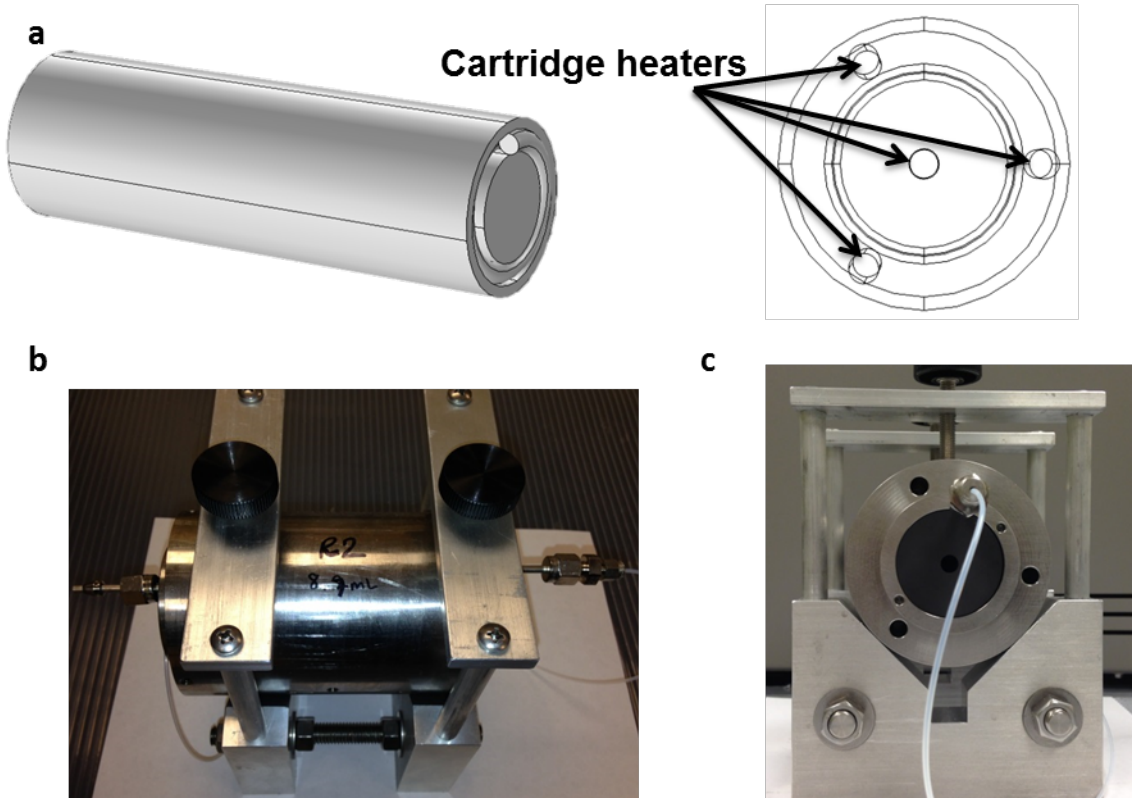

Figure 3.8. (a) Schematic of the stainless steel reactor module. The schematic shows a stainless steel tubing wound around a cylindrical graphite bar. The entire tubing and graphite bar assembly is encased inside a stainless steel casing. The diagram on the right shows the cross section view of the reactor module with four slots for cartridge heaters. **(b)** Top view and **(c)** front view of the fabricated stainless steel reactor module

Cooling zone simulation to obtain and fast and optimum cooling

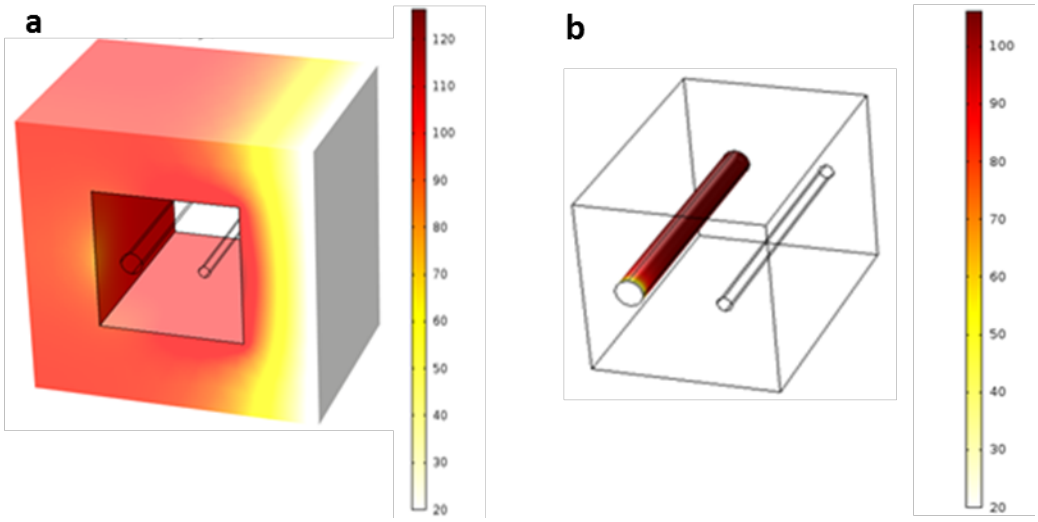

Figure 3.9. Model of the parallel flow (counter-flow) heat exchanger configuration used in COMSOL simulations for designing cooling zone. **(a)**Temperature of air flowing in the hood around the heat exchanger. **(b)** The bigger cylindrical channel on the right carries coolant, which is water (at 20 °C) in our case. The reactants enter the cooling zone through the smaller channel on left at a temperature of 250 °C. We found that the exit temperature of the reactants was independent of the flow rate of water because of the high thermal mass of water. The scale bars on the side represent temperature in °C. The parallel flow heat exchanger enables superior control on cooling over Shell tube heat exchanger design

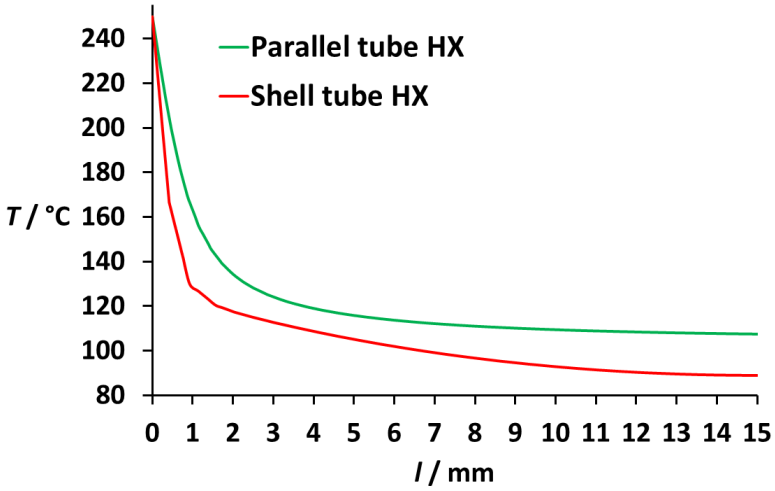

Figure 3.10. Temperature profile of the reactants for both, shell and tube and parallel flow heat exchanger configurations. Reactants enter the cooling zone at 0 mm at a temperature of 250 °C. Parallel flow heat exchanger seemed to provide fast and optimum cooling with the final exit temperature around 105 °C. On the other hand, shell and tube configuration provided a faster cooling at the expense of a lower exit temperature of about 85 °C. For our purposes, we chose shell and tube heat exchanger configuration. Water was chosen as the coolant in all the above simulations.

The reactor setup has uniform heating with no hot spots (Bi < 10)

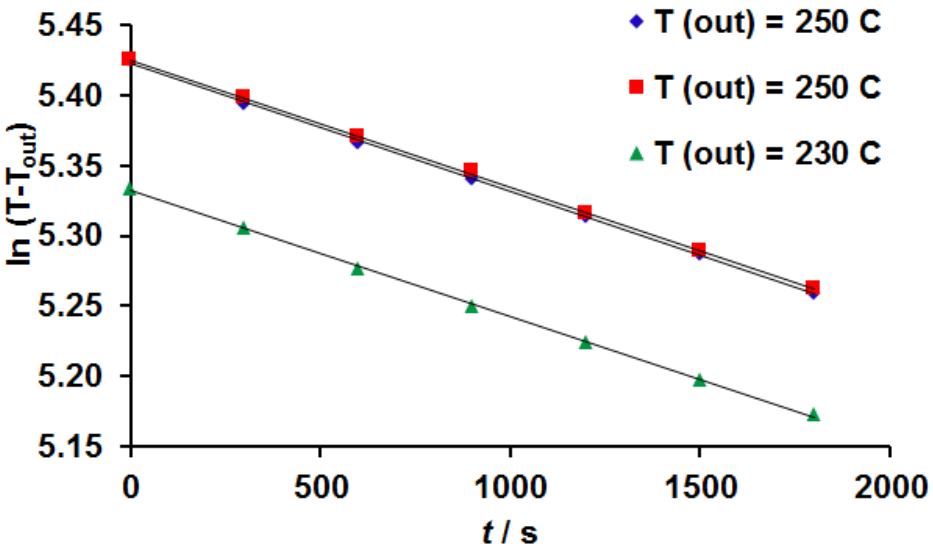

Figure 3.11. Results from the experiment that was carried out to calculate the Heat Loss Coefficient (U) for the insulated reactor module. "T" in the above graph represents temperature of the reactor that is measured by a thermocouple clamped to the reactor. "T_{out}" stands for the ambient temperature in the hood which was set to 22 °C. The insulated reactor module was first heated to a certain temperature and was then allowed to cool down slowly. The temperature of the reactor was recorded at regular intervals. According to the equation, Ln(T-Tout) should lie on a straight line which is what we see in the graph. The experiment was reproduced for a (starting) temperature of 250 °C and was also performed once at a different temperature (230 °C). All the three experiments produced straight lines with a constant slope of $9*10^{-5}$ s^{-1}.

$$m * Cp * dT = U * A * (T - Tout) \quad (1)$$

$$\frac{dT}{T - Tout} = \left(\frac{U * A}{m * Cp} * dt\right) \quad (2)$$

$$Ln\,(T - Tout) = \left(\frac{U * A}{m * Cp}\right) * t + k \quad (3)$$

Here "k" is a constant and (U*A)/(m*Cp) is the slop of the semi-log plot shown in Figure S3. The coefficient of heat loss (U) can be calculated by finding the slope of the lines in Figure S3 and substituting values for the physical constants involved in the equation. Using the heat loss coefficient, we found that the Biot number for the insulated reactor setup was of the order 10^{-6}, which is much less than 0.1. Therefore, the assumption of lumped capacitance and non-existence of any hotspots in the insulated reactor is validated.

Conversion estimation steps

1. Purify known volume (V mL) of product using centrifuge
2. After several steps of centrifugation, the nanoparticles (NP) are dissolved in small volume of hexane/chloroform
3. Dissolved NP is carefully transferred to the teflon tubes used for ICP (several transfer cycles are involved)
4. Solvents are removed from the mixture → dry NP
5. Sample is digested using HNO_3 and diluted to known volume (50 mL) before the ICP analysis
6. Concentration (C_p) of Cd and Se in the product was determined from ICP.
7. % conversion = C_p x 0.05/(102.5 x (V/53)) x (128.41/112.41)

Table 3.1. Yield of the reactor determined for different synthesis conditions based on Cd and Se concentrations in the product determined by ICP OES

Sample	Cd concentration (mg/L)	Yield (%)
CdSe (230 °C, 2 min)	55.2	54.2
CdSe (230 °C, 3 min)	65.3	64.9
CdSe (230 °C, 4 min)	72.06	70.73
CdSe (240 °C, 3 min)	63.7	81.28

Shape analysis of CdSe product reveals that continuous flow synthesis yields a high percentage of bipods compared to batch synthesis methods

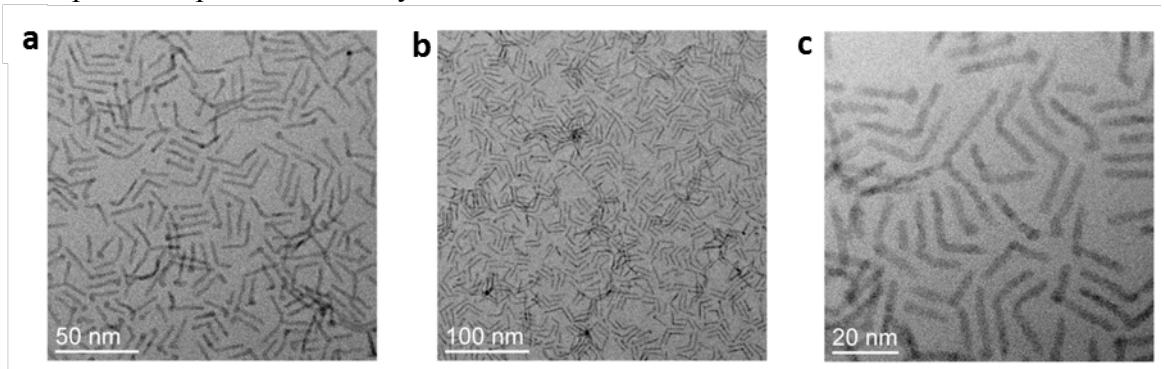

Figure 3.12. Shape analysis of CdSe– **(a)**, **(b)**, and **(c)** were used to calculate the percentage of bipods in the product. ImageJ software was used to count the number of bipods in the TEM images.

Table 3.2. Result of shape analysis of the images shown in Figure S7

Image	Number of particles analyzed	Number of bipods found	% of bipods
a	53	22	41.5
b	120	54	45
c	40	16	40
Total	213	92	43.2

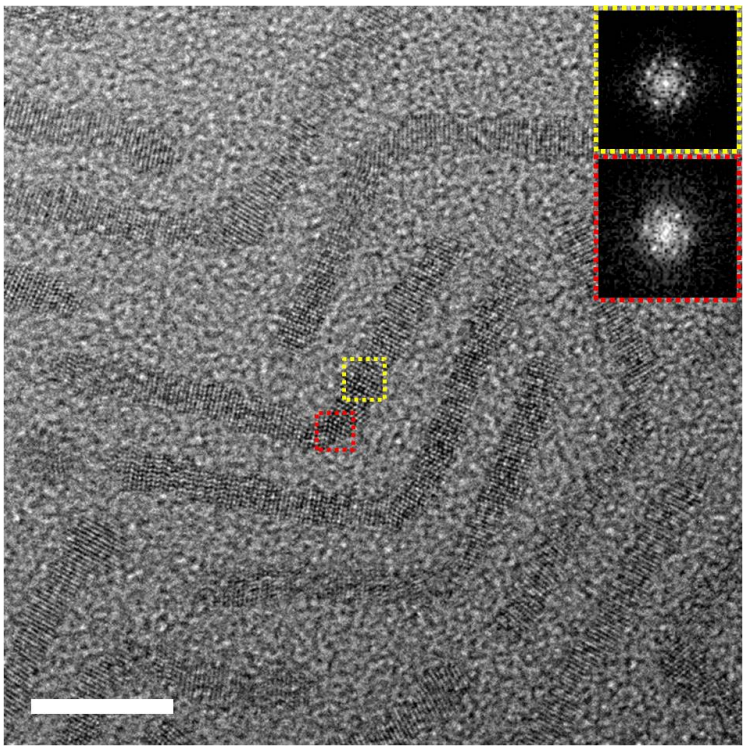

Figure 3.13. TEM image of CdSe bipods synthesized in the continuous flow reactor. The core of the bipods (shown in red) is very small (< 1 nm) and exhibits Zinc blende structure, while the arms of the bipods show distinct wurtzite structure. Scale bar = 10 nm

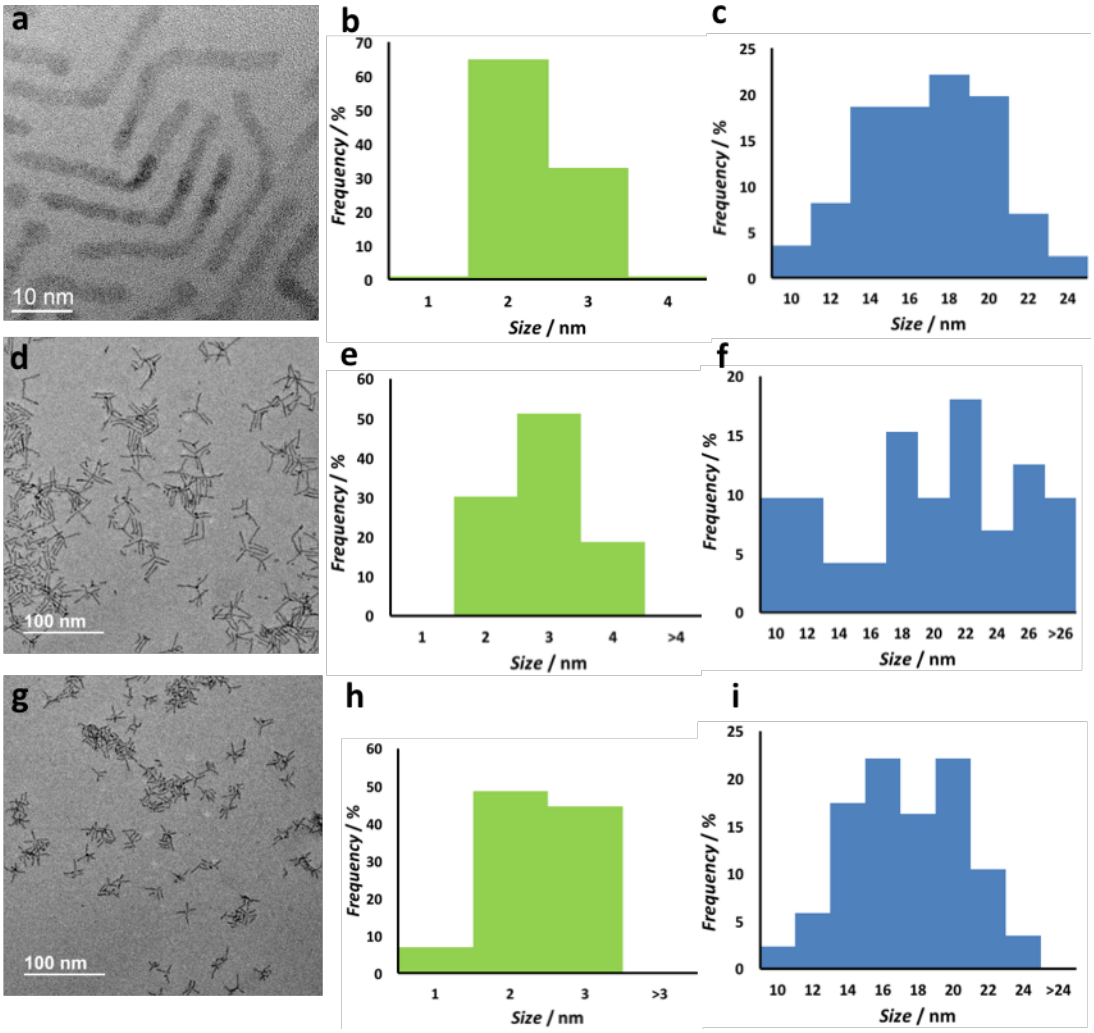

Figure 3.14. (a) TEM image of CdSe nanoparticles synthesized in the continuous flow reactor and its associated size analysis for **(b)** width and **(c)** length. **(d)** TEM image of CdSe nanoparticles synthesized using hot-injection technique in a batch reactor and its associated size analysis for **(e)** width and **(f)** length. **(g)** TEM image of CdSe nanoparticles synthesized via heat-up method in a batch reactor and its associated size analysis for **(h)** width and **(i)** length.

Operation protocol for air-sensitive reactions

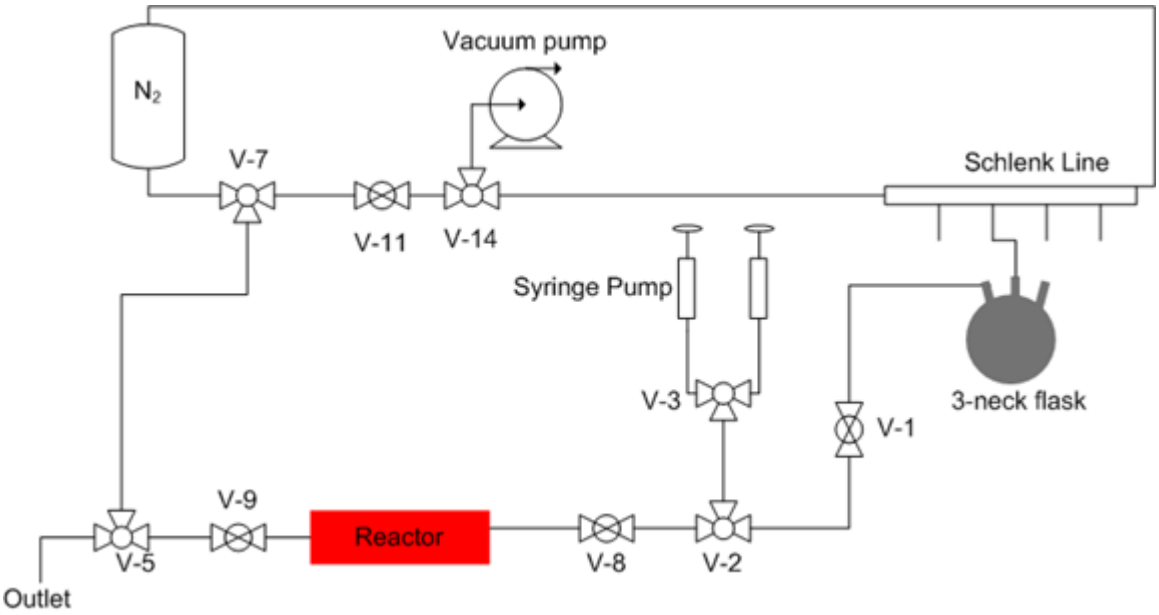

Figure 3.15. Piping and instrumentation diagram (P&ID) of the reactor setup that enables synthesis of nanoparticles that involve high temperature, air-sensitive reactions with solid/viscos reactants.

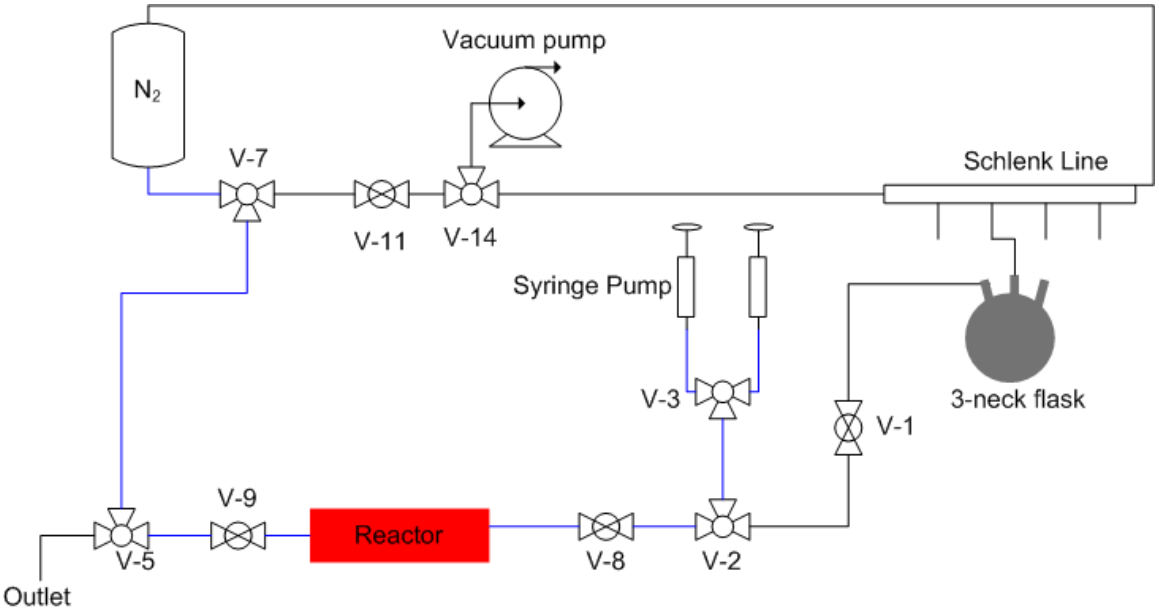

Figure 3.16. First step of the reactor startup process - Lines highlighted in blue are exposed to 3-4 cycles of nitrogen and vacuum. This is done to ensure good inert conditions in the reactor and the lines leading to or coming out of the reactor

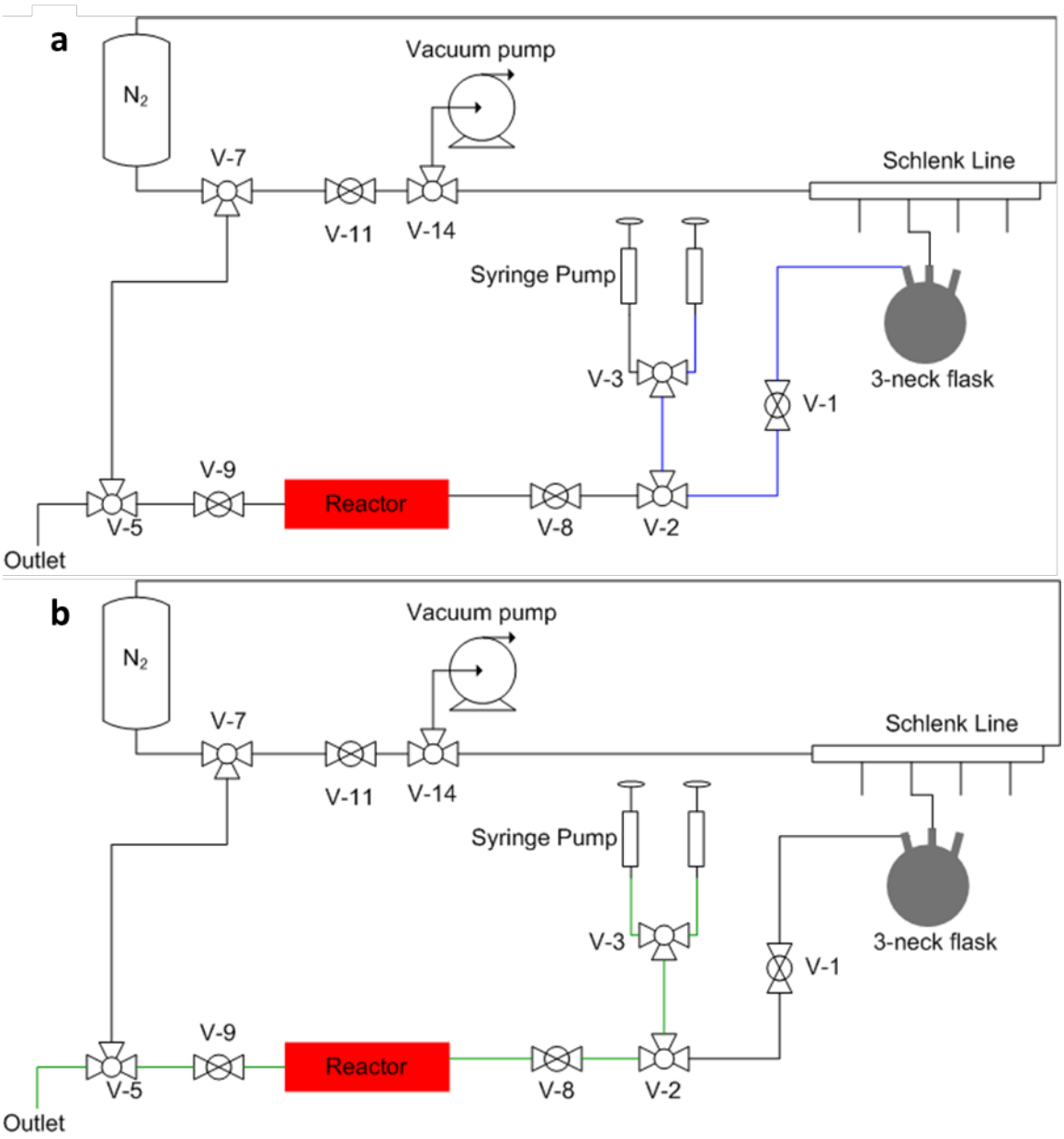

Figure 3.17. Second and third step of the startup process – **(a)** 3-neck flask is filled with solvent. The solvent is exposed to cycles of vacuum and nitrogen to get rid of any dissolved oxygen. All the lines leading to the syringes (highlighted in blue) are brought under inert conditions. 3-neck flask is then pressurized with nitrogen to push the reactants into the syringe (right); **(b)** A very similar process is followed to fill the syringe (left) with reactants while maintaining inert conditions

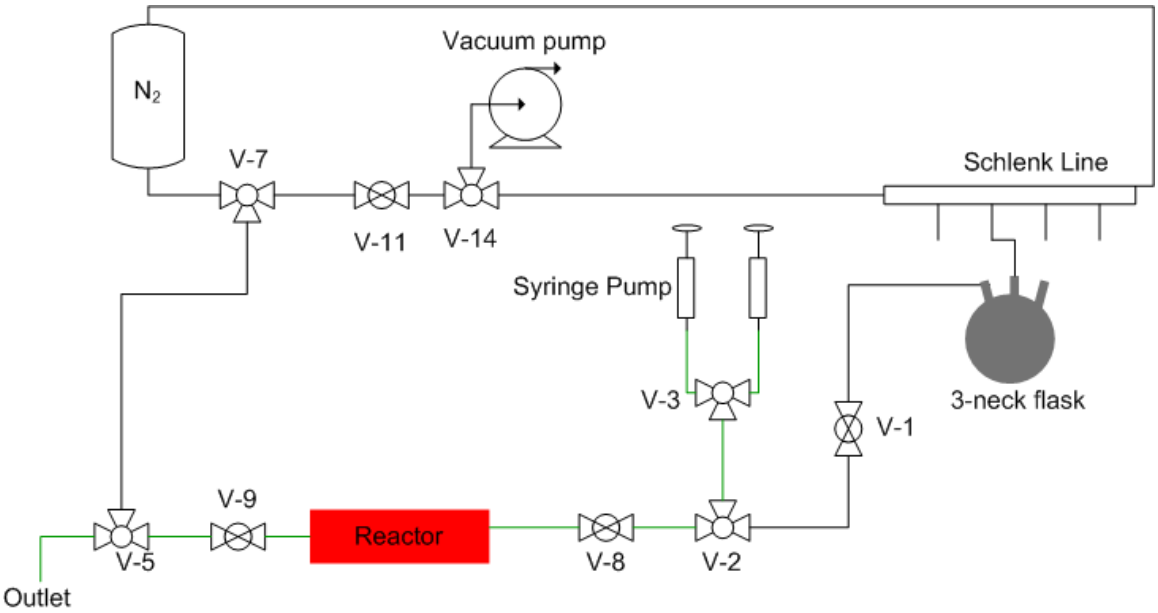

Figure 3.18. Synthesis step – Once the syringes are filled with solvent and reactants and all the lines have been made inert, the reactants are pushed into the reactor at a desired flow rate via syringe pump. The lines carrying the reactants are shown in green.

In order to maintain inert conditions throughout the flow reactor system the following protocol was developed and followed for all the reaction steps that needed inert conditions.

a) First, the reactor and the syringes are exposed to cycle of nitrogen and vacuum 3-4 times (Figure S8).
b) The reactor is then isolated from the rest of systems by closing the block valves, V-8 and V-9.
c) The syringes are then connected to the 3-necked flask via 3-way valve, V-2. Nitrogen in the syringe is then pushed out into the 3-necked flask, which is connected to the schlenk line.
d) The block valve, V-1 is now closed to isolate the 3-necked flask from rest of the system.
e) The reaction solvent is then added to the 3-necked flask and is exposed to cycles of nitrogen and vacuum 4-5 times via schlenk line.
f) Once the solvent is devoid of oxygen, it is then flowed into one of the two syringes by opening the valves V-1, V-2, and V-3. Nitrogen is used to push the contents from 3-necked flask into the syringe. (Figure S9a)
g) Vacuum is then applied to the 3-necked flask in order to clean left over reaction solvent present in the line connecting the 3-necked flask and the syringe. The block valve, V-1 is then closed again.
h) The 3-necked flask is then filled with reactants. The reactants are exposed to 4-5 cycles of nitrogen and vacuum.
i) Valves V-1, V-2, and V-3 are then opened and the reaction mixture is then pushed into the other syringe by pressurizing the 3-necked flask with nitrogen (Figure S9b)
j) The reaction mixture is then pushed out through the reactor at a set flow rate by diverting the flow towards the reactor via the 3-way valve, V-2 and opening the valves, V-8 and V-9 (Figure S10).

Table 3.3. ICP results of ZnSe nanorods synthesized at different temperatures and residence times (sample were diluted to 100 mL)

Sample	Se concentration (mg/L)	Zn concentration (mg/L)
ZnSe (260 °C, 2 min)	31.04	24.34
ZnSe (260 °C, 3 min)	36.28	27.31

EDS analysis of ZnSe nanorods

EDS analysis confirms the presence of ZnSe nanorods. Furthermore, traces of Fe, Cr, and Ni indicate reactor leaching. Further steps towards passivation of stainless steel reactor will inhibit any contamination of the product in the future.

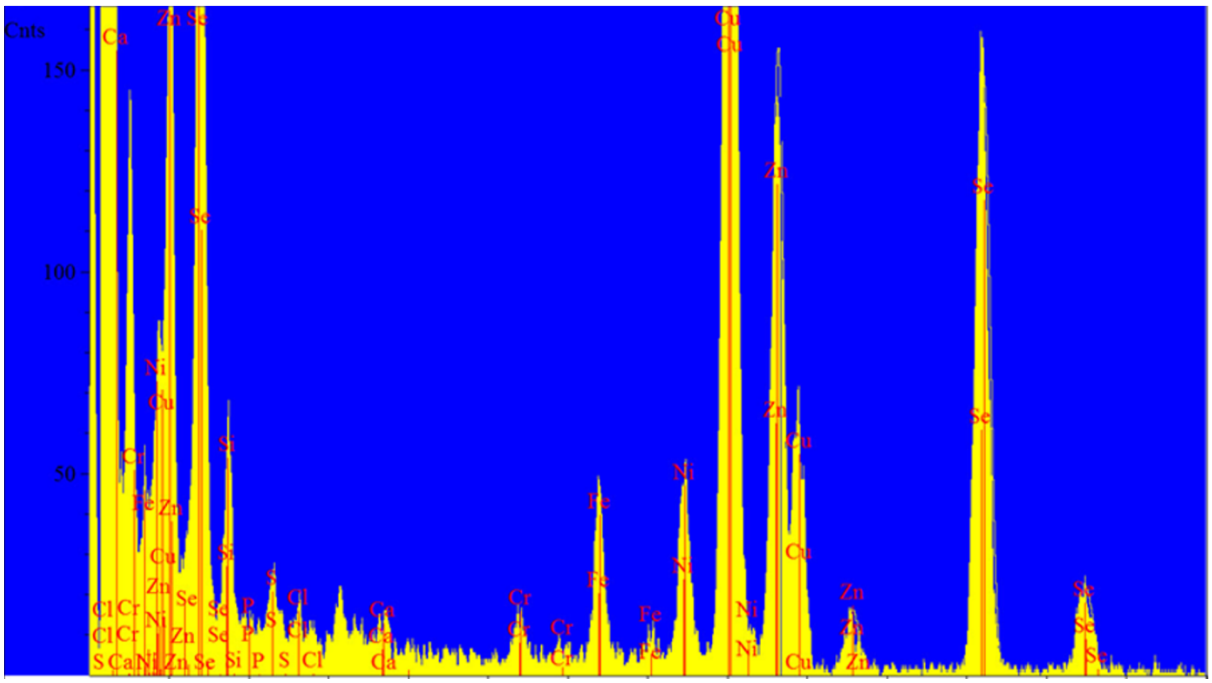

Figure 3.19. EDS analysis results for ZnSe nanorods synthesized at 260 °C and 3 min. The analysis indicated a Se/Zn ratio of 1.2/1. The ratio is in agreement with ICP analysis. Furthermore, traces of Fe, Ni, and Cr were present that indicates reactor leaching.

CHAPTER 4

MULTISTEP CONTINUOUS FLOW SYNTHESIS OF HIGHLY LUMINESCENT INDIUM PHOSPHIDE/ZINC-SELENIDE-SULFIDE NANOCRYSTALS*

4.1. Introduction

Colloidal quantum dots are of great importance due to their tunable optoelectronic properties. The size dependent optical properties make these particles very promising for many applications including, optoelectronics[1-10], photocatalysis[11,12], biolabelling and bioimaging[13-15], therapeutics[15,16]. CdSe has received the most attention among various semiconductor nanoparticle compositions[17]. Numerous synthesis techniques including, hot-injection[18-20], heat-up[19,21], SILAR[22-24], have been developed to precisely tailor the composition and morphology of Cd-based nanoparticles. Despite their advantages – high quantum yield, narrow FWHM, low blinking, high photostability – Cd-based nanoparticles have found a restricted use in the commercial products due to their high toxicity[25]. Furthermore, recent regulations against the use of Cd in the consumer products have cast a dark shadow on their potential use at a commercial scale. Although, tight encapsulation and recycling techniques could mitigate the environmental issues associated with the use of Cd-based nanoparticles, fundamental solutions are required to prevent the use of heavy metals. Amidst such regulations, the focus of the industry and academia

*This chapter has been adapted from the following manuscript in preparation: V. Kumar, U. Ramesh, K. Balakrishnan, N. Oh, K. Deshpande, M. Shim, P.J.A. Kenis, "Multistep continuous flow synthesis of highly luminescent InP/ZnSeS nanocrystals."

shifted to “greener” Cd-free materials, mainly III-V semiconductor nanoparticles that includes metals like Indium, Gallium, and Aluminium.

Indium phosphide (InP) nanoparticles (band gap: 1.35 eV) is the most widely studied III-V nanomaterial, mainly due to its emission in the visible wavelengths like CdSe, but without any intrinsic toxicity. This makes InP a viable alternative to CdSe. However, the strong covalency of Indium and Phosphorus makes it difficult to formulate labile precursor materials, which eventually leads to large amount of crystal defects. Difficult synthesis methods coupled with weak performance in terms of low quantum yield (< 1%), weak photo, and chemical stability have hindered the the use of In-based materials on a commercial scale. To overcome these aforementioned challenges, many studies have been conducted to control the surface properties of InP nanoparticles. Type-I core-shell quantum dots are known to exhibit enhanced photoluminescence when passivated with higher band-gap material[26-29]. Nann *et al.* demonstrated one of the first successful synthesis of high-quality InP particles[30]. Following this, many core-shell compositions were studied, including InP/ZnS[31-35], InP/ZnSe/ZnS[36,37] InP/ZnSeS[38,39], InP/GaP/ZnS[40], and ZnSe/InP/ZnS[41] that exhibited high photometric performance – quantum yields as high as 80% and strong photostability. Notable works include high external quantum efficiency (~3.46%) achieved by Lim *et al*[39]. and high luminous efficiency (54.71 lm/W) attained for white QD-LED by Kim *et al*[40]

Despite the progress made in the batch synthesis techniques of In-based nanomaterials, continuous scale synthesis of these nanomaterials appears lagging far behind. De Mello first reported on the successful application of a continuous flow reactor to synthesize In-based nanomaterials[42]. Their work serves as a good proof-of-concept study on the application of microfluidics to synthesize Cd-free materials. Soon after, Jensen *et al.* developed a special

microreactor to study the growth processes of InP nanoparticles[43]. The Jensen group has published several insightful studies on the application of microfluidics to understand the underlying mechanism involved in the formation and growth of these nanomaterials[44,45]. However, none of the works from the Jensen group pertains to the synthesis of highly luminescent In-based particles. Furthermore, the majority of the works related to In-based nanoparticles in the Jensen group use microreactors that is not suited for scalable synthesis of these nanoparticles. A few more studies in literature report on continuous flow synthesis of InP nanoparticles, but none addresses the issue of low photoluminescence quantum yields associated with these particles[46]. A recent study demonstrated multi-step synthesis of InP/ZnS core-shell nanoparticles in a hybrid reactor[34]. The reactor used in the aforementioned work is not truly continuous and can be best described as a hybrid of a semi-batch and a flow reactor. Moreover, the highest quantum yield achieved on this reactor is about 41% that is much less than what has been achieved using batch synthesis modes. Even on batch scale, high quantum yields (> 70%) have been attained only for intermediate wavelengths (500 – 580 nm). The highest quantum yields achieved in the red region (>610 nm) hovers around 60%.

In this work, we report on the multi-step continuous flow synthesis of highly luminescent InP/ZnSeS nanoparticles. The resulting nanoparticles exhibit quantum yields as high as 55% and wide range spectrum tunability. We were able to achieve quantum yields of over 50% for red emission wavelengths (610 - 700 nm) which exceeds all the previous results obtained for Cd-free nanoparticles synthesized in a continuous flow reactor. Furthermore, the aforementioned results for the red emission wavelengths are comparable to the best batch results for In-based nanoparticles. We also demonstrate the ability to synthesize blue-emitting InP quantum dots (quantum yields ~15%) that are very difficult to obtain even in a batch reactor and have not yet

been produced in a continuous flow reactor. The emission wavelength of the nanoparticles can be tuned to cover the entire visible range by changing the residence time (or flow rate), temperature of the InP core growth zone, and/or concentration of the precursors. The product was analyzed with the help of two flow cells positioned downstream of the reactor that provided real-time absorbance and fluorescence spectra of the product. The millifluidic reactor dimensions allow for operating flow rates as high as 1 L/min and is well suited for scalable synthesis of these nanoparticles.

4.2 Reactor module design, fabrication, and operation

The reactor module is composed of a 2.5 in thick and 5 in long stainless steel cylindrical bar with a 0.28 in wide hole in the center that runs the entire length of the reactor. This forms the reactant channel through which the reactants flow inside the reactor module. Four symmetrically placed slots are positioned around the reactant channel to host the cartridge heaters used for heating the reactor (**Figure 4.1a**). Each cartridge heater is 4" long and has a power rating of 60W. A stainless steel static mixer (Omega FMX 8442S) is placed in the reactant channel to break the parabolic flow front of the reactant stream to ensure narrow a residence time distribution (RTD) as shown in **Figure 4.1b**. We conducted tracer experiments to characterize the RTD of the reactor discussed in a subsequent section. The ends of the reactant channel are sealed with 1/8 NPT pipe-to-tube (1/8") compression fittings. The tapered pipe threads provide good air-tight seal. The reactor module was fabricated in the machine shop using conventional milling machine, thereby obviating the need for any special facilities associated with the fabrication of silicon-glass[47], glass[48,49], and ceramic[50] flow reactors. The fabricated reactor module is shown in **Figure 4.1c**.

As mentioned before, a static mixer is used in the reactant channel to ensure plug flow-like behavior in the reactor. Fluids flowing through a tube are known to exhibit a distinct parabolic flow profile in the laminar. The parabolic flow profile results in a residence time distribution that could potentially lead to variation in the product quality or less uniform particles in our case.

This reactant channel in the reactor module has a total volume of 5.2 mL and allows the reactants to be heated from 25 °C to 270 °C in less than 1 s (see supplementary information, Chapter 3), which is a major improvement over conventional batch synthesis. The entire reactor module is insulated using a layer of ceramic wool and a layer of ceramic roll (Unifrax LLC). The use of long cartridge heaters that run through the entire length of the reactor, and double insulation layers prevent any hotspots in the reactor, indicated by low Biot number (10^{-6}) for the system. Due to some differences in the threading process, reactor 1, R1 has a volume of 5.2 ml and the reactor 2, R2 has a volume 5.7 ml.

The fabricated reactor module was used in a configuration (**Figure 4.2** – schematic, **Figure 4.3** – P&ID) that allows for multistep synthesis of highly luminescent InP/ZnSeS. For all the syntheses described in this chapter, the core (InP) and shell (ZnSeS) precursors were first pre-mixed separately in two different 3-neck flasks that are connected to a schlenk line. The entire setup was then brought under inert conditions by flushing the setup with nitrogen for about 2 hours. The entire setup including the reactors, the 3-neck flasks, the air-tight collection vial was kept under positive pressure of about 5 – 10 psig with the help of a back-pressure regulator positioned downstream of the the collection vial. The positive pressure was maintained throughout the run to check any back-diffusion of air/oxygen into the reactor setup. First, the premixed InP core-precursor was flowed into the first reactor (R1) at a set flow rate (ranging from 0.1 mL/min to 1.5 mL/min) using a Masterflex peristaltic pump. The peristaltic pumps used

in the syntheses operate with Teflon tubings and therefore are compatible with the chemicals used in the syntheses at the operating temperatures. Furthermore, these pumps can also dry run as opposed to most of the piston pumps frequently used in many wet syntheses. The product exiting R1 was then mixed with the ZnSeS shell-precursors (stored in a second 3-neck flask) in an inline mixer that is specially designed to enable full mixing at the operating flow rates and the viscosities of the reactant streams. The inline mixer contains 5 Sulzer SMX plus mixing elements, each 4.8 mm wide and 4.8 mm long. The set of 5 mixing elements provides high enough strain rates to promote effective mixing between the incoming streams. The mixed stream was then flowed into the second reactor, R2 where the formation of ZnSeS shell occurred over InP cores. The SS lines (shown in red in **Figure 4.2)** carrying the reactants to the inline mixer and the second reactor (R2) are heated using rope heaters. The temperature of these lines is closely monitored and controlled using PID controllers (CSi-32k) and thermocouples positioned at various places along the lines. The reactors, R1 and R2, were run at different temperatures ranging from 220 °C to 240 °C and 290 °C to 320 °C respectively. We also varied the concentrations of the shell precursor to observe its effects on the quantum yield of the product.

The product streams exit the reactor at the respective operating temperatures of the reactors (generally > 200 °C). Cooling modules are installed downstream of the reactors to quench the temperature of the products to avoid any residual reactions. The cooling module design and fabrication is based on the same principles as discussed in Chapter 3. The detailed operating protocol is mentioned in supplementary information. The entire flow reactor setup used for the multistep synthesis of InP/ZnSeS particles is shown in **Figure 4.4**.

4.3 Residence time distribution and dispersion studies

Continuous flow synthesis is considered a superior technique for the synthesis of nanomaterials compared to the batch synthesis modes mainly because of the fast and precise temperature control and fast mixing. However, the positive effects of fast mixing often get marred by the ill-effects of so called broad "residence time distribution" in real flow reactors if not taken care of. In an ideal plug-flow reactor all the atoms leaving the reactor at a certain instant of time remain in the reactor for exactly the same amount of time before finally exiting. The time that the atoms spend in the reactor is called the residence time of the atoms in the reactor. However, in reality different atoms in the feed spend different times inside the reactor giving rise to a distribution of residence times of the materials within the reactor, commonly known as the residence time distribution. Residence time distribution in a continuous flow reactor results from a variety of reasons, the primary ones being the parabolic flow profile exhibited by a liquid stream flowing through a closed tube, axial and radial mixing due to molecular diffusion, dead zones, and short-circuit channeling[51]. For example, in the case of a parabolic flow profile, the section of the liquid that is the farthest from the walls flows the fastest (**Figure 4.5**). The flow velocity of the parabolic front decreases for the sections closer to the wall. Therefore, different sections of the liquid exit the reactor at different times giving rise to a residence time distribution. Non-ideality in a flow reactor can described in various ways including, one-parameter model, two-parameter model, and other computational intensive techniques. For the purposes of this thesis, we will restrict our discussion to one-parameter model, which includes both the Dispersion and Tanks-in-series models.

The dispersion model is frequently used to describe the non-idealities in a tubular reactor. In any tubular reactor, reactant depletion and non-uniform flow velocities lead to concentration gradient paving way for molecular diffusion, both in axial and radial directions. In addition, for a

turbulent flow, the eddies tend to even up any concentration gradient much faster than molecular diffusion. However, we will restrict the discussion to the laminar regime only since the Reynolds number for the operating conditions in our reactor never exceeds 16 indicative of a laminar flow regime in the reactor. It is extremely difficult to formulate a model that accurately incorporates all the aforementioned factors. Therefore, the Dispersion model was derived based on the following two assumptions to simplify the analysis without compromising on the accuracy of the model

1. The model assumes radial homogeneity and the mean velocity ($\bar{u}$) of the process stream is equal to the ratio of the volumetric flow rate of the process liquid and cross-section area of the tube.
2. The model assumes an "axial dispersion" coefficient (D_a) that subsumes the effects of all the dispersive phenomena resulting from molecular and convective diffusion such as Aris-Taylor dispersion in the laminar regime, turbulent diffusion resulting from the eddies in the turbulent regime, and non-uniform velocity profiles. The axial dispersion coefficient is governed by an equation that is analogous to Fick's law of diffusion in which the dispersion coefficient ($D_a \partial C/\partial z$) is used in place of the regular diffusion term in addition to bulk transport term ($\bar{u}C$).

The following equation is obtained when a non-dimensionalized mass balance equation is written for a reactant stream flowing into a tubular reactor

$$\frac{\mathbf{1}}{\boldsymbol{Pe}}\frac{\boldsymbol{\partial^2 \Psi}}{\boldsymbol{\partial z^2}} - \frac{\boldsymbol{\partial \Psi}}{\boldsymbol{\partial z}} - \boldsymbol{Da}(\boldsymbol{\Psi^n}) = \mathbf{0} \tag{1}$$

$$\boldsymbol{Pe} = \bar{\boldsymbol{u}}\boldsymbol{L}/\boldsymbol{D_a} \tag{2}$$

$$\boldsymbol{Da} = \boldsymbol{kC^{n-1}L}/\bar{\boldsymbol{u}} \tag{3}$$

In the above equations, *Pe* is Peclet number, Ψ is the dimensionless concentration, *C* is the actual concentration, z is the dimensionless length, L is the characteristic length of the system, *k* is the kinetic constant of the reaction, n is the order of the reaction, D_a is the dispersion coefficient, and Da is the Damkohler number, $\bar{u}$ is the mean flow velocity in the direction of the flow.

The dispersion coefficient or alternatively, Pe, provides an estimation of the intensity of the dispersion effects in the reactor. Based on the reactor dimensions and the general operating conditions, we obtained a ratio of 21.4 for the reactor length over diameter, while the Bodenstein number and the Reynolds number are ~3000 and ~16 respectively. This results in an Aris-Taylor dispersion coefficient is about 9.27×10^{-5} resulting in a Peclet number of 0.87, which indicates high dispersion regime based on **Figure 4.6**[52].

High dispersion in the reactor prompted us to use a static mixer (FMX 8442S, Omega) in the reactor to minimize dispersion. To characterize the residence time distribution after installing the static mixer in the reactor, we performed the step-input tracer dye experiments. The step-input experiments generate Cumulative Distribution Function, F(t), whose first derivative with respect to time yields the Residence Time Distribution. Two syringe pumps (PHD 2000, Harvard Apparatus) were used to drive the syringes filled with deionized water and a solution of Amaranth (tracer dye) separately. The concentration of the dye solution was maintained to ensure a linear relationship between the absorption peak intensity at 520 nm and concentration of the dye. The two syringes were connected to the reactor via a 4-way injector valve (Cole-Parmer). An absorption flow cell (connected to a UV-Vis spectrometer) was positioned downstream of the reactor to collect the absorbance spectrum of the dye solution exiting the reactor. We also made sure to keep the distance between the 4-way valve, reactor, and the

absorbance flow cell as short as possible to minimize any dispersion effects outside the reactor. First, the reactor was primed with deionized water for about 0.5 hour (equivalent at least 5 residence times at the operating flow rates) at a set flow rate (1 mL/min and 2 mL/min) to ensure a steady state flow inside the reactor. Then the valve was quickly turned to allow the dye to flow through the reactor at the same flow rate as the water at time t = 0. The absorbance readings were collected at an interval of 2 seconds starting at t = $\tau/2$, where "τ" is the residence time at the operating flow rate - 5.2 min for 1mL/min and 2.6 min for 2 mL/min. The readings were collected until the absorbance peak intensity at 520 nm plateaued at the final value which is same as that of the dye solution in the syringe. The experiments were repeated three times for each flow rate. The absorbance peak intensity at 520 nm was then plotted against time to generate a sigmoidal looking F(t) for each experiment. The curves were fitted and the RTD was derived using MATLAB and Origin (**Figure 4.7b-c** and **4.8b-c**). The spread of an RTD curve provides a qualitative measure of the extent of dispersion in the reactor. Several correlations exist that relate the variance of an RTD curve with the dispersion coefficient of the reactor for different boundary conditions. In our case, the open open vessel boundary condition is applicable since there is a possibility of dispersion both upstream (in the lines joining the valve to the reactor) and downstream of the reactor (in the lines joining the reactor to the flowcell). The Pe number can be calculated using equation (4)[51]

$$\frac{\boldsymbol{\sigma^2}}{\boldsymbol{\tau^2}} = \frac{\mathbf{2}}{\boldsymbol{Pe}} + \frac{\mathbf{8}}{\boldsymbol{Pe^2}} \qquad (4)$$

The low flow rate of 1 mL/min exhibits good reproducibility. The dispersion number (D/uL) and the associated Pe for the flow rate were and 2.4×10^{-6} and 378071 respectively. An almost symmetric RTD curve coupled with the peaks positioned at $t/\tau = 1$ indicates a good plug flow-like behavior in the reactor[51,52]. However, at a higher flow rate of 2 mL/min, the cumulative

distribution function did not look as smooth. F(t) contained more small disturbances (**Figure 8**) that were smoothened out with the help of MATLAB. The RTD curve derived from the fitted F(t) indicated the presence of dead zones within the reactor which is evident from a long tail and the peak-position at $t/\tau > 1$. The black curve is drastically different from the other two curves as the run was affected by the presence of a few air bubbles observed during the experiment. The average Peclet number and dispersion number for the flow rate of 2 ml/min were 7912 and 1.26×10^{-4} respectively.

It is easier to perform a step-input tracer experiment compared to a pulse-input experiment as generation of a good pulse that resembles the Dirac Delta function requires more expensive specialty injection valves. The pulse-input experiment suffers from issues like inaccurate pulse generation, low signal/noise ratio. Although easier to perform, the step-input experiment has the tendency to mask small disturbances in the flow behavior due to the integral nature of the curve. For instance, any curve smoothening performed to obtain a fitted curve veils a lot of non-idealities that would have otherwise resulted in multiple peaks in an RTD curve. Therefore, it is advisable to use the results obtained using a step-input experiment with caution.

4.4 Multistep continuous flow synthesis of InP/ZnS nanocrystals

Synthesis Chemistry: Indium acetate (99.5%), Myristic acid (Sigma grade, >99%), Octadecene (technical grade, 90%), Oleic acid (90%), Octylamine (99%), Trioctylphosphine (TOP) (90%), zinc stearate (technical grade), and Zinc diethyldithiocarbamate ($ZnDDTC_2$) (97%) were purchased from Sigma-Aldrich and used as received. Tris(trimethylsilyl)phosphine (>98%) was purchased from Strem Chemical and used as received. To prepare 0.1M stock solution of Indium myristate, 3 mmol of Indium acetate was heated with 9 mmol myristic acid in 30 mL of

Octadecene at about 200 °C about an hour until a clear Indium myristate solution was obtained. The Indium myristate stock solution was then transferred to a glove box in an air-tight vial after an hour of thorough degassing. 10 mmol of Zinc diethyldithiocarbamate (ZnDDTC) was dissolved in 10 ml of TOP to prepare 1M stock solution of ZnDDTC-TOP. Similarly, 1M TOP-S and TOP-Se stock solutions were prepared by sonicating 10 mmol of S and Se in 10 mL of TOP in two separate airtight vials. All the stock solutions were stored in a glove box. For a typical synthesis, 0.1 mmol of zinc stearate, 0.2 mmol of Oleic acid, 0.4 mL of Octylamine and 20 mL of Octadecene were stirred under inert atmosphere in a 3-neck flask (InP-flask) equipped with a condenser. The mixture was then heated to 120 °C until zinc stearate dissolved completely in Octadecene. In a separate 3-neck flask (ZnS-flask), 0.4 mL of Octylamine, and 20 mL of Octadecene are stirred under inert conditions. The entire reactor setup was purged with nitrogen for about an hour to get rid of any oxygen in the setup. Following the nitrogen purge, the 3-neck flaks were again exposed to nitrogen and vacuum cycles for about 45 min. The entire setup (including the 3-neck flasks) was then maintained at a positive pressure of about 5 psig to avoid any back diffusion of air. 2 ml (0.2 mmol) of Indium myristate was premixed with 0.04g of Tris(trimethylsilyl)phosphine (TMSP) and 2 mL Octadecene in a glovebox. The solution quickly changed the color to pale yellow indicating the formation of InP nuclei. The pre-mixed solution containing InP nuclei is then transferred to the InP-flask under inert conditions to avoid any oxidation of the nuclei. The contents from the InP-flask are pumped into the first reactor set at 240 °C at flow rate of 2.4 mL/min (equivalent residence time of 2.67 min). Once the product starts to flow out of the second reactor (and starts approaching the static mixer) the second pump is turned on to pump the contents from the ZnS-flask at a flow rate of 2.4 mL/min. The two streams (product from the first reactor and the precursors from the ZnS-flask) mix well as they

flow through the static mixer into the second reactor. The temperature for the second reactor is set at 190^{o}C. The product from the second reactor flows into an absorbance and fluorescence flow cells that enables inline analysis of the product as it exits the second reactor.

Preparation of Indium myristate stock solution. 3 mmol of indium acetate were mixed under inert atmosphere with the desired quantity (i.e. 4-8 mmol) of myristic acid (MA) and 30 mL of ODE in a 50 mL three neck flask equipped with a condenser. The mixture was heated to 100-120°C for 1 h under vacuum to obtain an optically clear solution, backfilled with nitrogen, and then cooled down to room temperature. The prepared stock solution was stored in a glovebox.

4.5 Multistep continuous flow synthesis InP/ZnSeS nanocrystals

Indium acetate (99.5%), Myristic acid (Sigma grade, >99%), Octadecene (technical grade, 90%), Oleic acid (90%), Octylamine (99%), Selenium (99.99%), Sulfur, 1-Dodecanethiol (> 98%) Trioctylphosphine (TOP) (90%), and zinc acetate (99.99%) were purchased from Sigma-Aldrich and used as received. Tris(trimethylsilyl)phosphine (>98%) was purchased from Strem Chemical and used as received. For a typical synthesis, 0.2 mmol of zinc stearate, 0.4 mmol of Oleic acid and 20 mL of Octadecene are stirred under inert atmosphere in a 3-neck flask (InP-flask) equipped with a condenser. The mixture is then heated to 120 °C until zinc stearate dissolves completely in Octadecene. 2 ml (0.2 mmol) mmol of Indium myristate ($In(MA)_3$) is premixed with 0.04g of Tris(trimethylsilyl)phosphine and 2 mL Octadecene in a glovebox. The pre-mixed mixture is then transferred to the InP-flask under inert conditions. In a separate 3-neck flask (ZnSeS-flask), 5 mmol of Zinc acetate, 4 mL of Oleic acid and 16 mL of Octadecene are stirred under inert conditions until Zinc acetate dissolves completely. 0.3 mL of TOP-Se (1 M solution) is premixed with 3 mL of TOP-S (1 M solution) or 1.8 mL of Dodecanethiol in a glovebox. The premixed solution is injected into the ZnSeS-flask. The entire reactor setup

(including the 3-neck flasks) is maintained at a pressure of 5 psi. The contents from the InP-flask are pumped into the first reactor at a set flow rate, ranging from 0.1 mL/min to 1.5 mL/min. Once the product starts to exit the first reactor, R1 (and starts approaching the static mixer) the second pump is turned on to flow the contents from the ZnSeS-flask at the same flow rate as the first pump. The two streams (product from the first reactor and the precursors from the ZnSeS-flask) mix well as they flow through the static mixer into the second reactor, R2. The product exiting R2 flows through an absorbance and a fluorescence flowcell that enable inline analysis of the product. The product is finally collected in an airtight vial. To examine the effects of different process parameters, the flow rates (0.1 – 1.8 ml/min), the temperature of R1 (220 °C – 240 °C) and R2 (300 °C – 320 °C) were varied.

Characterization. The product was first passed through a syringe filter (pore size - 0.22 mm) to get rid of any particulates and unreacted Zn-based complex. The clear filtrate solution was then typically diluted 1:30 in chloroform to obtain an absorbance reading between 0.02 and 0.05 absorbance units (substantial additional dilution was required for certain samples) and were analysed in solution without additional purification or size selection. Fluorescence results from a common purification process (mix with methanol and ethanol in a 20:1 alcohol:effluent ratio, shake to generate an emulsion, centrifuge at 13,000 rpm for 5 minutes, pour off liquid, suspend in chloroform) were within 90-110% of the values obtained from the as-synthesized solution.[14] Absorption spectra were obtained from an 8453 UV-Vis Diode Array System spectrophotometer (Agilent) and fluorescence spectra were obtained from a Jobin-Yvon Fluoromax-3 spectro-fluorimeter (Horiba); a 385 nm excitation wavelength was used for the In-based nanoparticles. Quantum yields (QY) were determined by comparing to a (1) quinine sulfate solution in 0.1 M

H_2SO_4 (58% quantum yield)[53] and (2) Rhodamine B solution in ethanol such that the absorbance of the solution was less than 0.01 at 510 nm (70% quantum yield).

4.6 Results and Discussion

The initial goal of the experiment was to demonstrate multistep synthesis of highly luminescent InP/ZnSeS core-shell nanoparticles in a continuous flow reactor. The majority of the literature on continuous flow synthesis of semiconductor nanoparticles has focused on Cd-based compositions. There was a palpable shift in the interest towards Cd-free materials post the regulations against the use of Cd in the consumer products. In the last decade, there have been countable attempts to synthesize In-based nanomaterials in continuous flow reactors. However, there is no account of highly luminescent (QY > 50%) In-based nanomaterials synthesized on a continuous scale. To date, the best result involves synthesis of InP/ZnS nanoparticles exhibiting quantum yields of ~40% in a reactor that can be best described as a hybrid of semi-batch and flow reactor.

Initial studies explored the feasibility of synthesizing InP nanoparticles involving highly air-sensitive reagents (TMSP) in a continuous flow reactor using a one-step synthesis procedure. To mitigate any risks of oxidizing TMSP, $In(MA)_3$ and TMSP were mixed in a glovebox resulting in pale-yellow solution. The colour change indicates the nucleation of InP particles[31,32]. The pre-mixed solution containing InP nuclei was then transferred to a 3-neck flask, which already contained the solvent (Octadecene) and Zn Oleate maintained under inert conditions. The contents of the 3-neck flask were mixed for 5 minutes at ~60 °C which is low enough a temperature to avoid any unwanted reaction[54-57]. The mixed solution was pumped at a fixed flow rate through the reactor, R1 set at 240 °C; only one reactor module (R1) was used for the synthesis InP nanoparticles. We found our results in agreement with the previous studies[58] that

demonstrate the importance of Zn in stabilizing InP nanoparticles by passivating InP nanoparticle surface. InP particles with Zn exhibit a sharper absorbance peak compared to the product without Zn.

Following the one-step synthesis of InP nanoparticles, an inline static mixer and another reactor module (R2) was added to the reactor setup to enable multistep synthesis of InP/ZnS and InP/ZnSeS core-shell nanomaterials. The synthesis procedure for InP core was kept the same as described in the above paragraph. Furthermore, the lines connecting the Zn-flask, static mixer, and reactor (R2) were heated (80 – 90 °C) to prevent any solidification of Zn Oleate in the lines. During the initial attempts, TOP-S and TOP-Se were used as S and Se sources respectively. Since TOP-Se is more reactive than TOP-S, the TOP-Se:TOP-S ratio was kept greater than 1:10 to ensure comparable reactivity of the two precursors, thereby promoting formation of ZnSeS alloy[59,60]. Zn was used in excess to ensure a thick shell cover. The products exhibited moderate quantum yields with a maximum of ~30% at a high residence time of 58 min in R1 and ~32 min in R2. We observed that the products obtained at low residence times exhibited broad FWHM (QDs emitting in blue region) at best and two peaks (QDs emitting in orange) at worst. We repeated the InP/ZnSeS runs with 1-dodecanethiol (DDT) as the S-source[35,61]. DDT is less reactive than TOP-S, therefore TOP-Se is expected to preferentially react before DDT resulting in a higher concentration of ZnSe shell coating around InP cores[39]. The concentration of ZnSe gradually decreases with the distance from the InP core particles. InP QDs with a thin shell of ZnSe close to the cores and a thick ZnS shell farther away from the cores is expected to exhibit higher photoluminescence and photostability since it marries the benefits of lower lattice strain (3.4% from thin ZnSe shell) with high passivation abilities of the ZnS shell. In general, we were able to cover the entire visible spectrum (**Figure 4.10** and **4.16b**) by varying the different process

parameters – flow rate, InP-core growth temperature (R1), ZnSeS shell growth temperature (R2), and relative concentration of ZnSeS precursors with respect to In precursors. However, in this work we will not discuss the effect of relative concentration of ZnSeS-shell precursors due to a lack of enough data points. As shown in **Figure 4.10a**, we were able to synthesize blue particles by running the reactants at a flow rate of about ~1.73 mL/min resulting in a residence time of about 3 min in R1 and about 1.64 min in R2. Blue QDs exhibited low quantum yields of about 15%, which we believe happens as a result of inadequate shell formation over the core InP particle due to very short residence times in the second reactor, R2. An intermediate flow rate of ~ 0.31 mL/min yielded particles emitting in the orange region (585 nm) as shown in **Figure 4.10b**. Particles emitting in the deep red region (**Figure 4.10c**) were achieved by running the reactants at a very slow flow rate (<0.1 ml/min). The use of DDT as a S-source resulted in a considerable higher photoluminescence compared to the InP/ZnSeS particles synthesized using TOP-S. The highest QY achieved was about 55% for a flow rate of 0.1 ml/min and the temperatures of 230 °C (R1) and 310 °C (R2). However, the amount of Zn and S precursors used was reduced to about 60% of the original amount mentioned in the Materials and methods section.

Effect of the process parameters. The quantum yield and the emission wavelength increased with the shell-growth temperature (**Figure 4.11e-f**) We believe that high temperature induces thermodynamic shell-growth conditions resulting in effective and homogenous shell formation and therefore high quantum yields. It is worth noting that the fracture-resistance stainless steel reactor enabled us to operate at temperatures (320 °C) close to the boiling point of Octadecene (318 ± 5 °C) since the reactor was run under a moderate back pressure, ranging from 4 – 10 psig. These examples show promise for future experiments to be conducted at even higher

temperature and pressure. In addition to the suitable thermodynamic conditions for shell growth, quantum dot synthesis is known to benefit from accelerated mass transfer of the reagents, typically observed in supercritical regimes. However, the QY increases with shell-growth temperature until a point where an optimum thickness of the shell is reached **(Figure 4.11f)**. We believe that a steep red-shift and a drop in the quantum yield around 320 °C caused by the formation of a thicker shell due to high mass transfer rates. Similarly, a high InP core growth temperature (R1) results in a product emitting at a higher wavelength due to the formation of bigger particles (**Figure 4.11 c-d**). The InP core growth temperature seemed to have a positive impact on the QY of the final product as more crystalline particles are expected to form at higher temperatures. We were able to tweak the emission wavelength of the QDs by varying the flow rates (**Figure 4.11a-b**). As observed in the syntheses involving TOP-S, fast flow rates produced smaller particles that emitted in the blue region and exhibited low quantum yields compared to the products obtained using long residence times. The emission spectra for the products obtained using short residence times either had an additional secondary peak (around 450 nm) or very broad FWHM (>90 nm). Furthermore, the secondary peak typically almost disappeared for very slow flow rates. We believe that the two peaks in the fluorescence spectra are due to a bimodal population of InP/ZnSeS in terms of size, which is indicative of aggregative coalescence growth mode.

The composition of the InP/ZnSeS particles were determined using XRF (**Table 4.1**). The composition was in agreement with the results obtained using ICP OES. The presence of Se was further confirmed using EDS.

Table 4.1. Composition of InP/ZnSeS particles emitting at different wavelengths

Emission peak (nm)	In (%)	P (%)	Zn (%)	Se (%)	S (%)
585 (I)	1.8	2.2	49.1	11.1	35.7
604	2.1	2.3	39.3	9.3	46.2
617	1.7	2.3	51.7	11.6	33.2
585 (II)	2.0	2.1	46.5	10.3	39.0

The particle size was analysed with the help of Scanning Transmission Electron Microscopy (STEM) images (**Figure 4.12**). We deliberately imaged two different products having different quantum yields, but similar emission peak positions (616 nm). We found that the product with a lower QY has an average diameter of 6.1±1.0nm, while the one with the higher QY had a mean size of 6.±1.3nm. The average diameter of the InP cores (excitonic peak ~580 nm) for these products was estimated to be 2.9 – 3.0 nm[29,55,62]. This essentially indicates that the shell thickness for the products with high QY and low QY are about 1.5 nm and 1.75 nm respectively. We believe that thicker shell causes higher strain, thereby adversely affecting the QY of the product. Therefore, an optimum shell thickness (~ 1.1 nm) is required to achieve a high QY[39]. HAADF-STEM images confirmed ZnSeS shell around the InP core indicated by a six-fold symmetry as seen in **Figure 4.13**. Each edge of the hexagon is about 0.39 nm which is in agreement with the zinc blende crystal form of ZnS (0.38 nm). We believe that a higher edge length (of the hexagon) is due to the alloy nature of the ZnSeS shell. An analogous edge length for a ZnSeS (alloy) shell will lie between 0.38 nm (pure ZnS) and 0.40 nm (pure ZnSe) depending on the composition of the shell[63].

Evidence of aggregative coalescence growth. InP particles are known to grow via non-molecular ripening; highly reactive phosphine-based precursors react very quickly when mixed

with In-precursors. This results in the depletion of the phosphorus molecular precursors[64], thereby providing ideal conditions for non-molecular ripening[43]. Non-molecular ripening can proceed via Ostwald ripening or aggregative growth processes (dynamic coalescence). STEM images of the InP/ZnSeS particles show irregular, non-spherical shaped particles that is characteristic of an aggregative growth process (**Figure 4.12**). Furthermore, aggregative growth is known to produce a bimodal size distribution[65,66] at intermediate reaction times (close to characteristic nucleation time, $\tau_{nucleation}$) in the reaction. At intermediate times, the colloidal solution is considered to be composed of primary nanocrystals (small-sized particles) and critical-sized aggregates (big-sized particles) which gives rise to a bimodal size-distribution[65,67]. The bimodal size distribution then converges to a unimodal size-distribution composed mainly of critical-sized aggregates if the reaction is continued for long enough (reaction time >> $\tau_{nucleation}$) since the smaller particles become progressively unstable (thermodynamically) with time. Eventually, the smaller particles either dissolve away into the solution or coalesce to form bigger particles at longer reaction times. Detailed studies on ripening process reveal that the population eventually reaches a steady size distribution (or alternatively variance) irrespective of the starting point for ripening[6868]. This trend is consistent with the observed results (**Figure 4.13**). We observed two prominent peak at fast flow rates or consequently, short residence times. We believe that the emission peak at the shorter wavelength is due to the primary nanocrystals and the peak at the longer wavelength is due to the critical-sized aggregates. When one of the products exhibiting binary peaks (**Figure 4.13a**) was imaged using STEM, we found showers of small InP/ZnSeS particles (**Figure 4.14b**) along with big particles. The size of the small particles matched well with the secondary emission peak (**Figure 4.14a**). This confirms our hypothesis of the existence of populations of two different sizes in the solution at intermediate reaction times.

When the reaction is continued for longer residence time times (slower flow rates), we observe that the peak at the shorter wavelength diminishes and eventually disappears completely.

4.7 Conclusions

In conclusion, we demonstrated the multistep synthesis of highly luminescent InP/ZnSeS particles that cover the entire visible spectrum in a continuous flow reactor. The particles synthesized in the continuous flow reactor exhibited PL QY as high as 55%, which exceeds all the previous best results for Cd-free nanoparticles synthesized in a continuous flow reactor. Furthermore, high quantum yields (>50 %) were achieved for particles emitting in the red region (> 610 nm), which exceeds the best results in the literature to date. We also demonstrated the synthesis of In-based particles emitting in the blue region with a moderate QY of about 15%. The size of the In-based core-shell particles could be effectively tuned by varying the different process parameters - flow rate, concentration and reaction temperature. This enabled the flow reactor setup to synthesize particles spanning the entire visible spectrum. The millifluidic dimensions of the flow reactor allow for high operating flow rates up to 1 L/min.

The continuous flow reactor enables precise control of the reaction conditions including, temperature and residence time. This allowed us to probe into the growth mechanism of InP-based particles. It is widely accepted in the literature that the InP particles grow via nonmolecular ripening. However, there has been no reference to InP particles exhibiting aggregative growth mechanism. In our work, we see evidences of aggregative growth for InP nanomaterials in terms of the irregular shaped particles as seen in the STEM images and bimodal size distribution at relatively short residence times. The bimodal size distribution eventually grows into a unimodal distribution at long residence times, which is typical of an aggregative

growth mechanism. These examples serve as strong proves in the favour of aggregative growth mechanism adopted by the InP particles.

Next, a sensitivity analysis will be performed to identify the important process parameters based on their impact on the quantum yield of the final product. To ensure a distinct layer of ZnSe shell around the InP cores, the shell formation step can be performed in two separate steps. The results of the two-step shell formation can then be compared with the single-step shell formation to assess any differences in the two synthetic strategies. In addition to optimizing the synthetic strategies to achieve high quantum yields, the reactor setup can also be applied to obtain more insights into the growth mechanism of InP particles, which will further corroborate the preliminary evidences of aggregative growth exhibited by InP particles.

Acknowledgements

We gratefully acknowledge financial support from the Dow Chemical Company for research agreement #226772AC and a graduate fellowship to VK. We thank Dr. Pete Trefonas, Dr. Jieqian Zhang, Dr. Jong Park, and You Zhai for stimulating discussions.

4.8. Figures

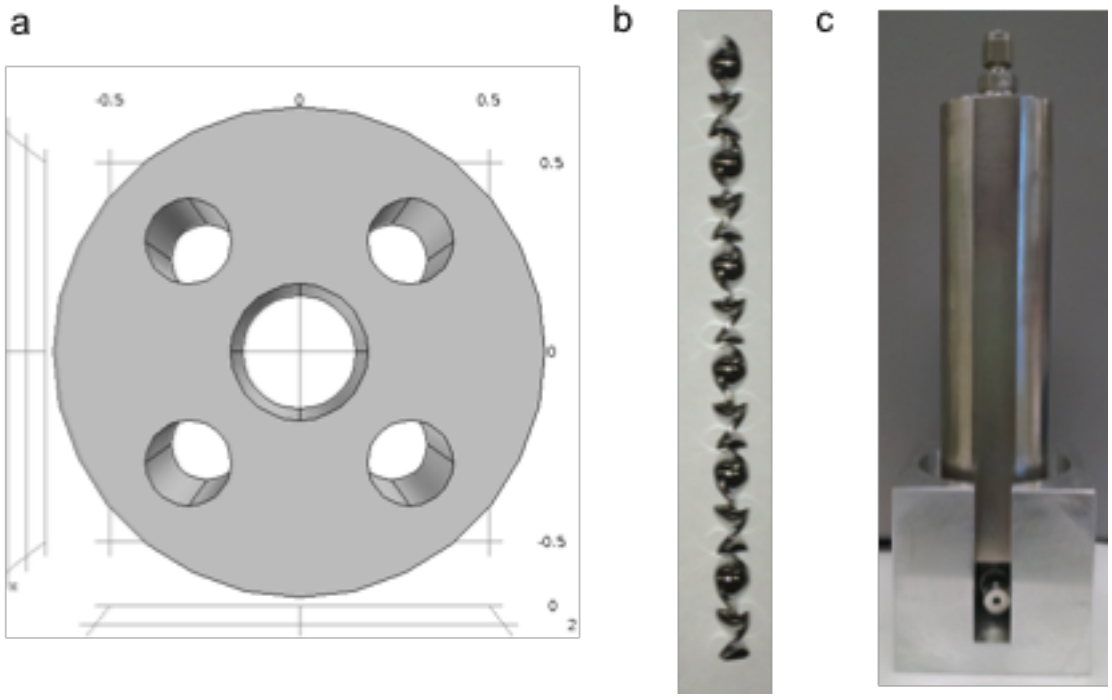

Figure 4.1. (a) Cross-section of the reactor module. The hole in the center is the reactant channel that hosts the static mixer shown in **(b)**. **(c)** Fabricated reactor module with an inlet at the bottom and an outlet at the top.

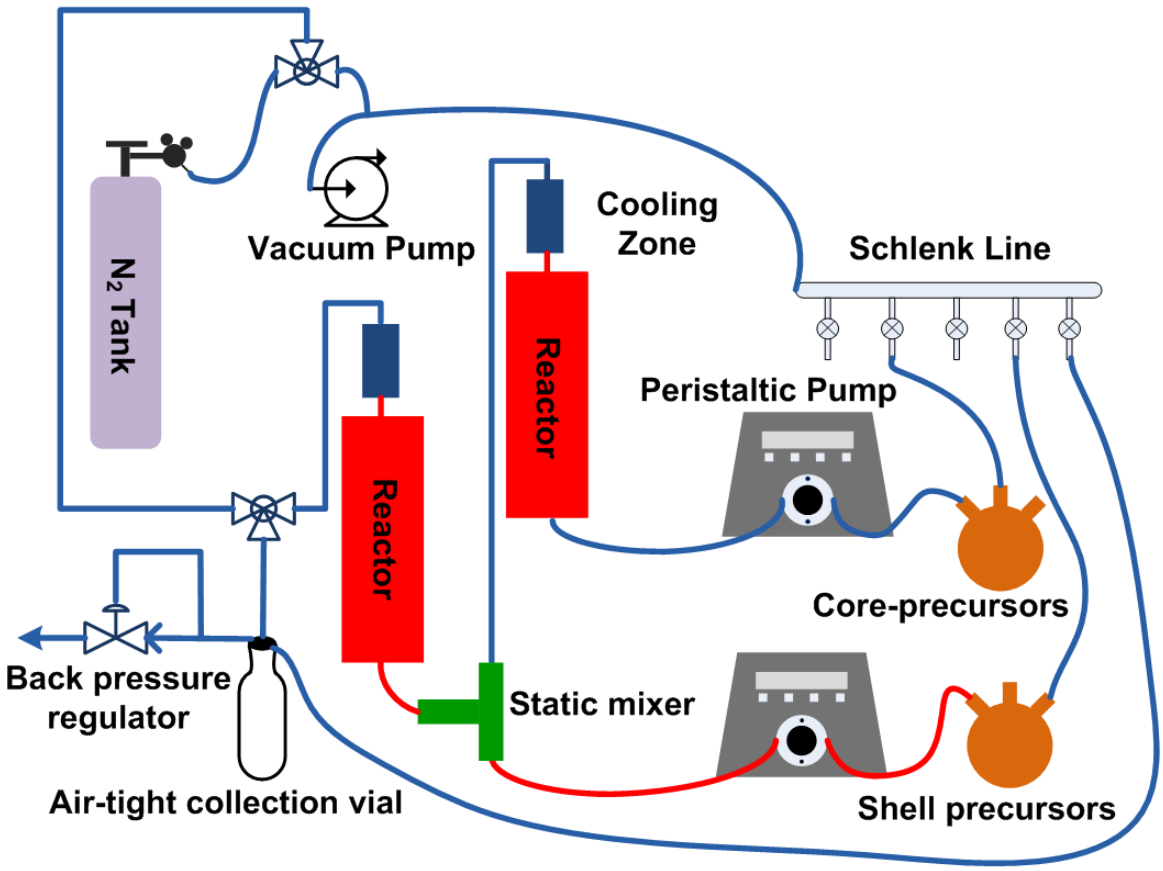

Figure 4.2. Schematic of the flow reactor setup for multistep continuous flow synthesis of InP/ZnSeS nanoparticles via high temperature and air-sensitive reaction. The temperature of the red lines is precisely controlled. The blue lines carry the reactants at room temperature. The core and shell precursors are premixed separately in two three-neck flasks under inert condition. The precursors are flowed through the reactor using two peristaltic pumps at a desired flow rate. The temperature of products flowing out of the reactor was quickly quenched with the use of a cooling unit downstream of the reactor module to avoid any residual reactions.

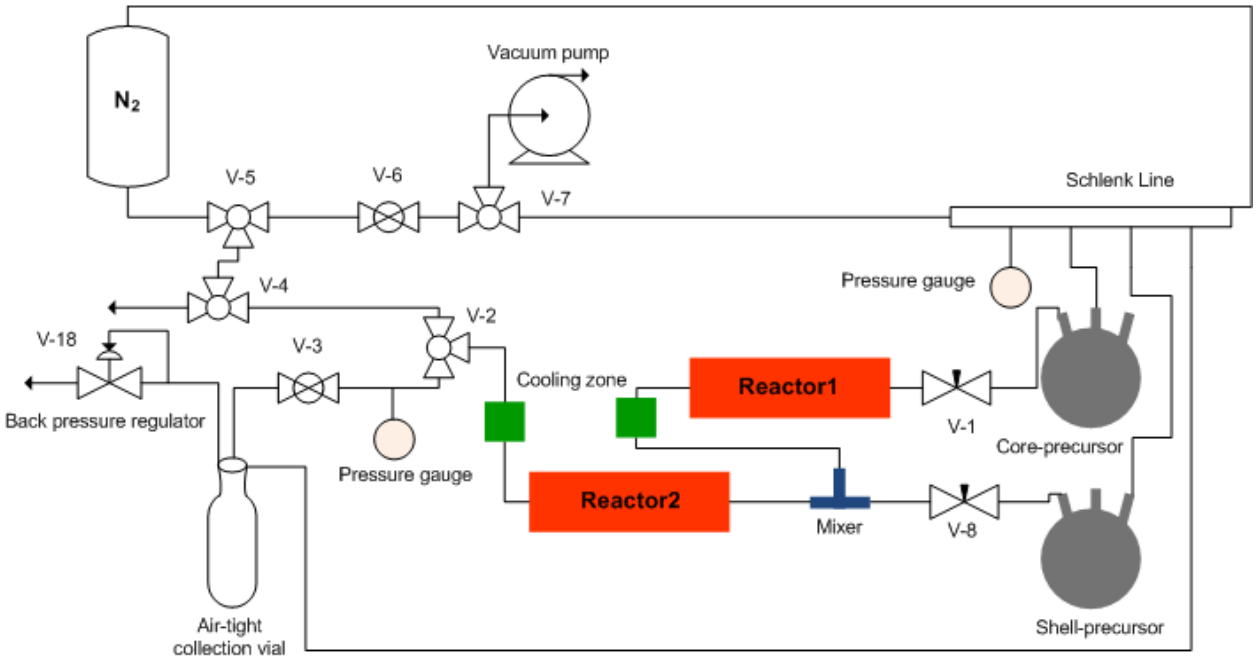

Figure 4.3. Process flow diagram of the continuous flow reactor for multistep synthesis of InP/ZnSeS nanoparticles. The peristaltic pumps are omitted for simplicity. The entire setup is brought under inert conditions before flowing the InP core precursors into Reactor1. The InP cores mix with ZnSeS precursors in the inline mixer as they exit reactor1. The well-mixed stream then enters Reactor2 for shell-growth process, after which, the product exiting Reactor2 is collected in an air-tight vial. The reactor setup is maintained at a positive pressure (5 – 8 psig) for the entire synthesis.

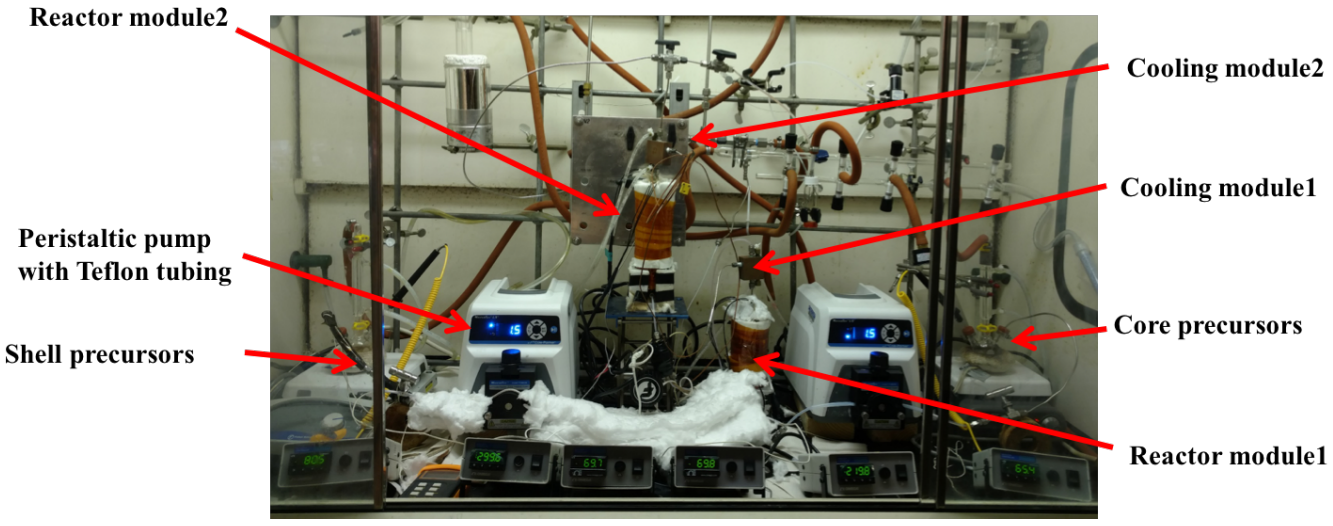

Figure 4.4. Image of the multistep continuous flow reactor setup inside a fumehood.

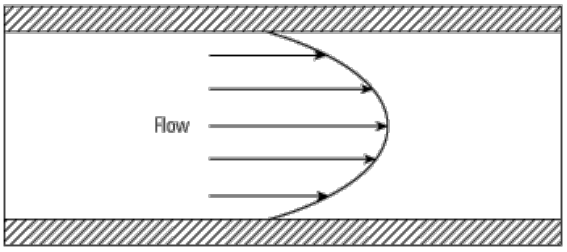

Figure 4.5. Parabolic flow profile for a liquid flowing through a tube (laminar regime). The shaded areas on top and bottom represent walls where the fluid velocity is assumed to be 0 for no-slip boundary conditions. The velocity of the flow front increases with the distance from the walls. Adapted from Wikipedia

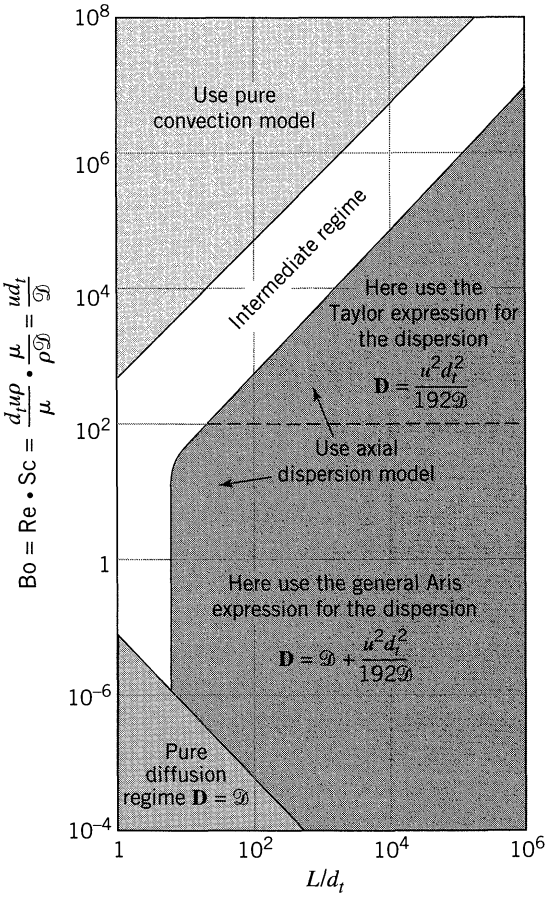

Figure 4.6. A chart showing different flow models that can be used based on Bodenstein number (Bo) and the geometry of the tube characterized by the ratio of the length of the channel and the diameter of the channel. Adapted from Levenspiel.

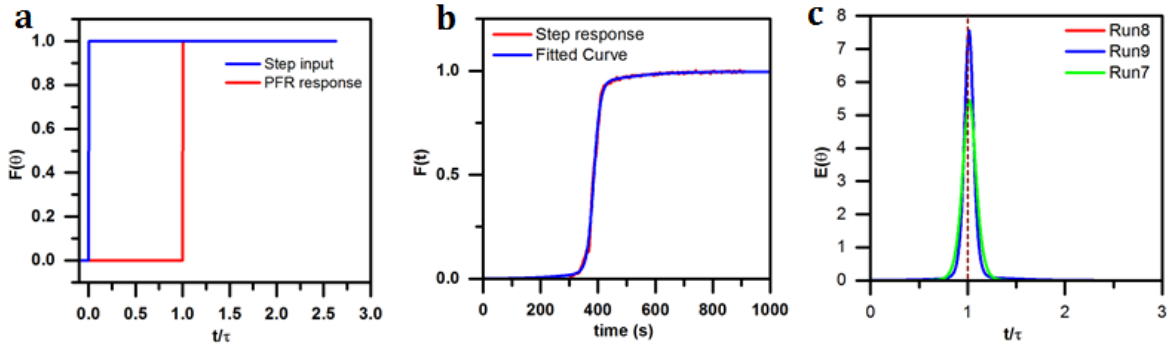

Figure 4.7. Cumulative response curve, F(θ), at a flow rate of 1 ml/min for (a) an ideal PFR, (b) the continuous flow reactor used for multistep synthesis of InP/ZnSeS particles. (c) The residence time distribution derived from the cumulative function shown in (b) for the continuous flow reactor. Average dimensionless variance for the RTD curves in (c) was 0.0023. The mean residence time (τ) at 1 ml/min was 380 s. The symmetric shape and the peak position at at $t/\tau = 1$ of the residence time distribution curve indicate a plug flow reactor-like behavior. The Peclet number (Pe) obtained by using equation (4) was 378071 yielding a dispersion number of 2.64×10^{-6}.

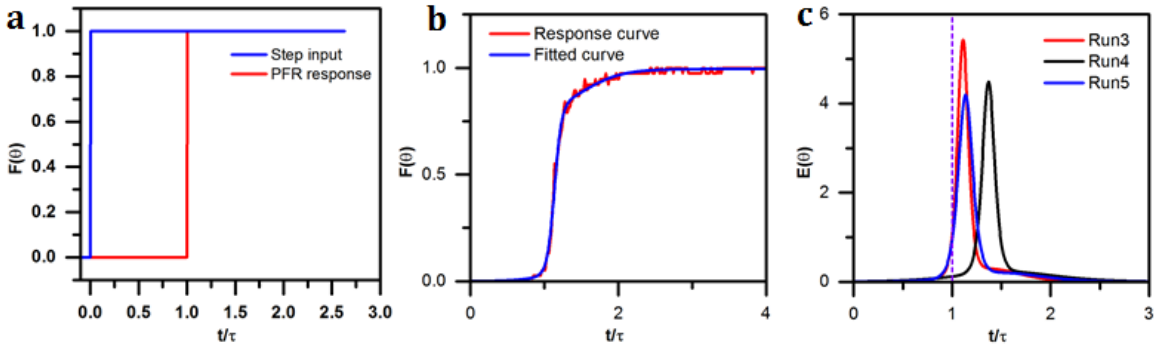

Figure 4.8. Cumulative response curve, F(θ) obtained at a flow rate of 2 ml/min for (a) an ideal PFR, (b) the continuous flow reactor used for multistep synthesis of InP/ZnSeS particles. (c) The residence time distribution derived from the cumulative function shown in (b) for the continuous flow reactor. Unlike 1 ml/min, the RTD for the flow rate 2 ml/min exhibited asymmetric shape with a longer tail. Also, the peak position shifted to $t/\tau > 1$, which is indicative of the presence of dead zones in the reactor. Run 4 in (c) looks marginally different from Run 3 and Run 5 as it was seemingly affected by the presence of a few air bubbles. The average dimensionless variance for Run 3 and Run 4 was 0.0159 and the mean residence time, τ was 190 s. The Peclet number obtained by using equation (4) was 7912, which results in a dispersion number (D/uL) of 0.000126.

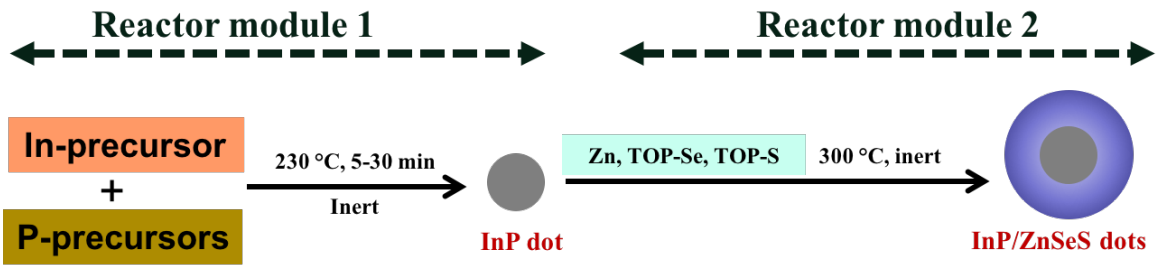

Figure 4.9. Schematic of the InP/ZnSeS dots synthesis procedure. The InP cores are synthesized in the reactor module 1 and the ZnSeS shell-growth takes place in the reactor module 2.

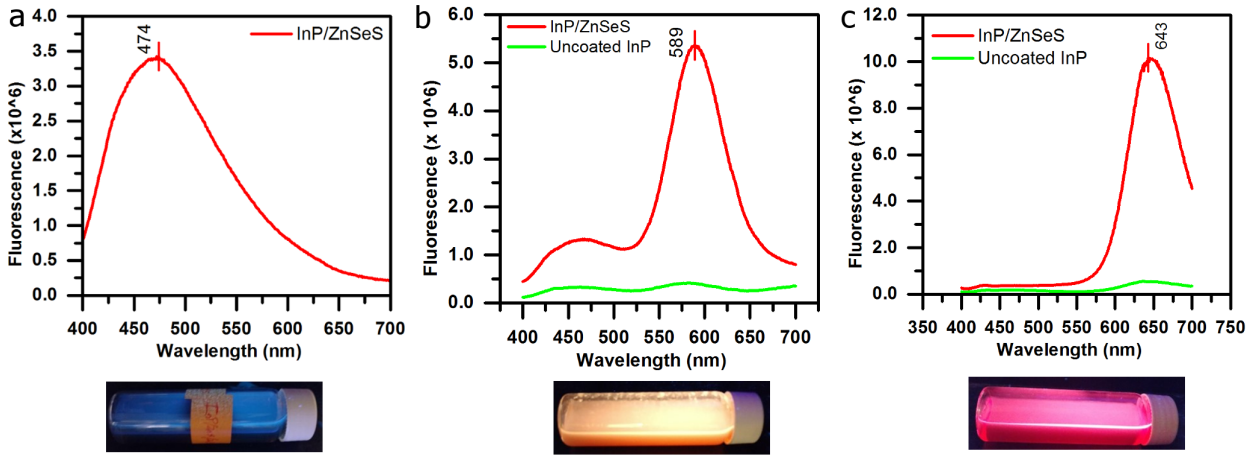

Figure 4.10. (a) Top – InP/ZnSeS synthesized at 230 °C (R1), 300 °C (R2), and 3 min (R1). Bottom – Particles in the top inset illuminated under UV light (365 nm). **(b)** Top – InP/ZnSeS synthesized at 220 °C, 300 °C, 20 min. Bottom – Particles in the top inset illuminated under UV light (365 nm). **(c)** Top – InP/ZnSeS synthesized at 230 °C, 315 °C, 45 min. Bottom – Particles in the top inset illuminated under UV light (365 nm). Also, it is worth noticing that the uncoated InP particles in (b) and (c) exhibit much lower photoluminescence than InP/ZnSeS particles.

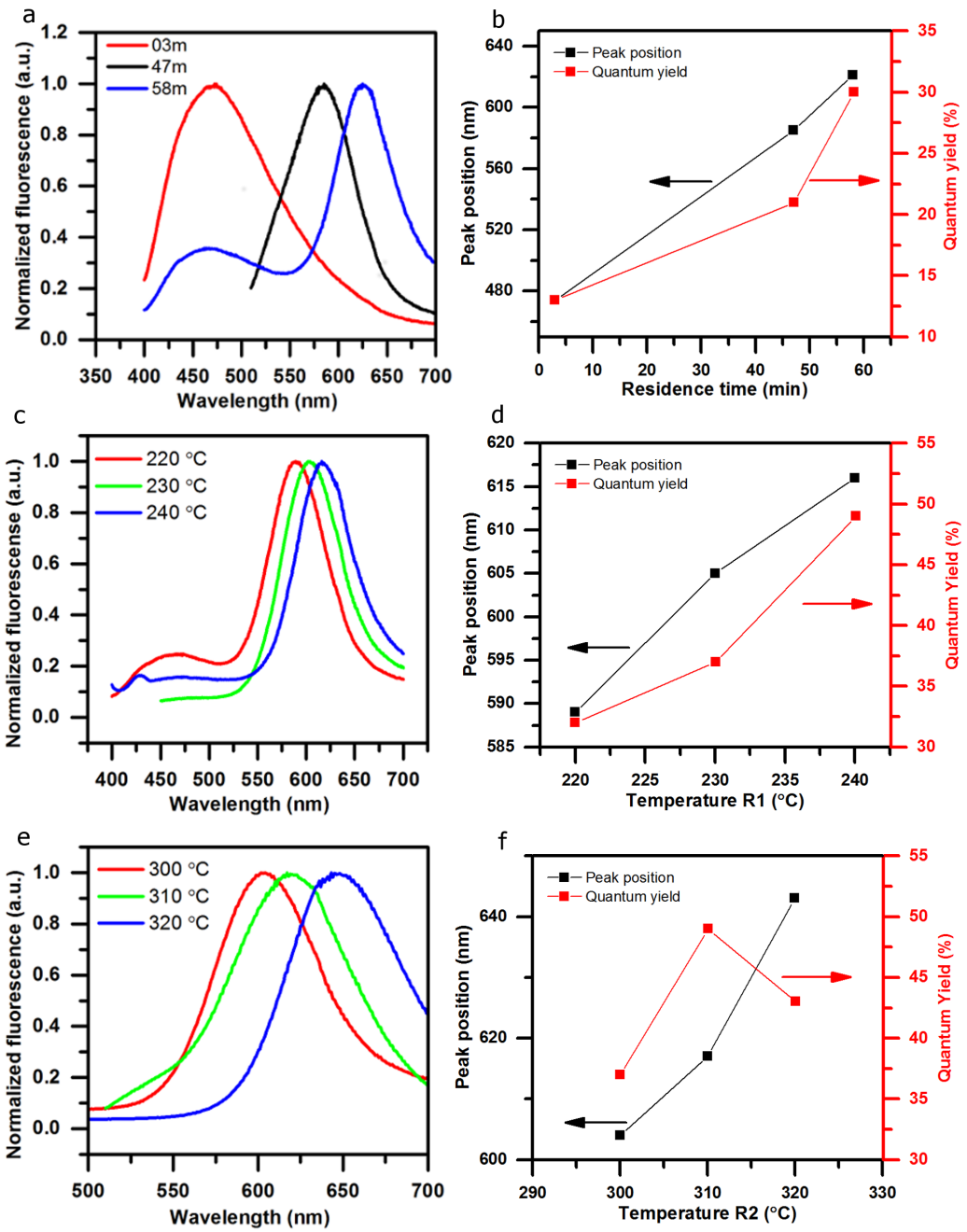

Figure 4.11. (a) Fluorescence spectra of InP/ZnSeS particles synthesized using different residence times (R1), 230 °C (R1), 300 °C (R2). **(b)** Quantum yields and peak positions for the particles mentioned in (a). **(c)** Fluorescence spectra of InP/ZnSeS particles synthesized using different InP core growth temperatures (R1), 300 °C (R2), and a residence time of 45 min (R1). **(d)** Quantum yields and peak positions for the particles mentioned in (c). **(e)** Fluorescence spectra of InP/ZnSeS particles synthesized using different shell-growth temperatures (R2), 230 °C (R1), and a residence time of 45 min (R1). **(f)** Quantum yields and peak positions for the synthesis conditions mentioned in (e).

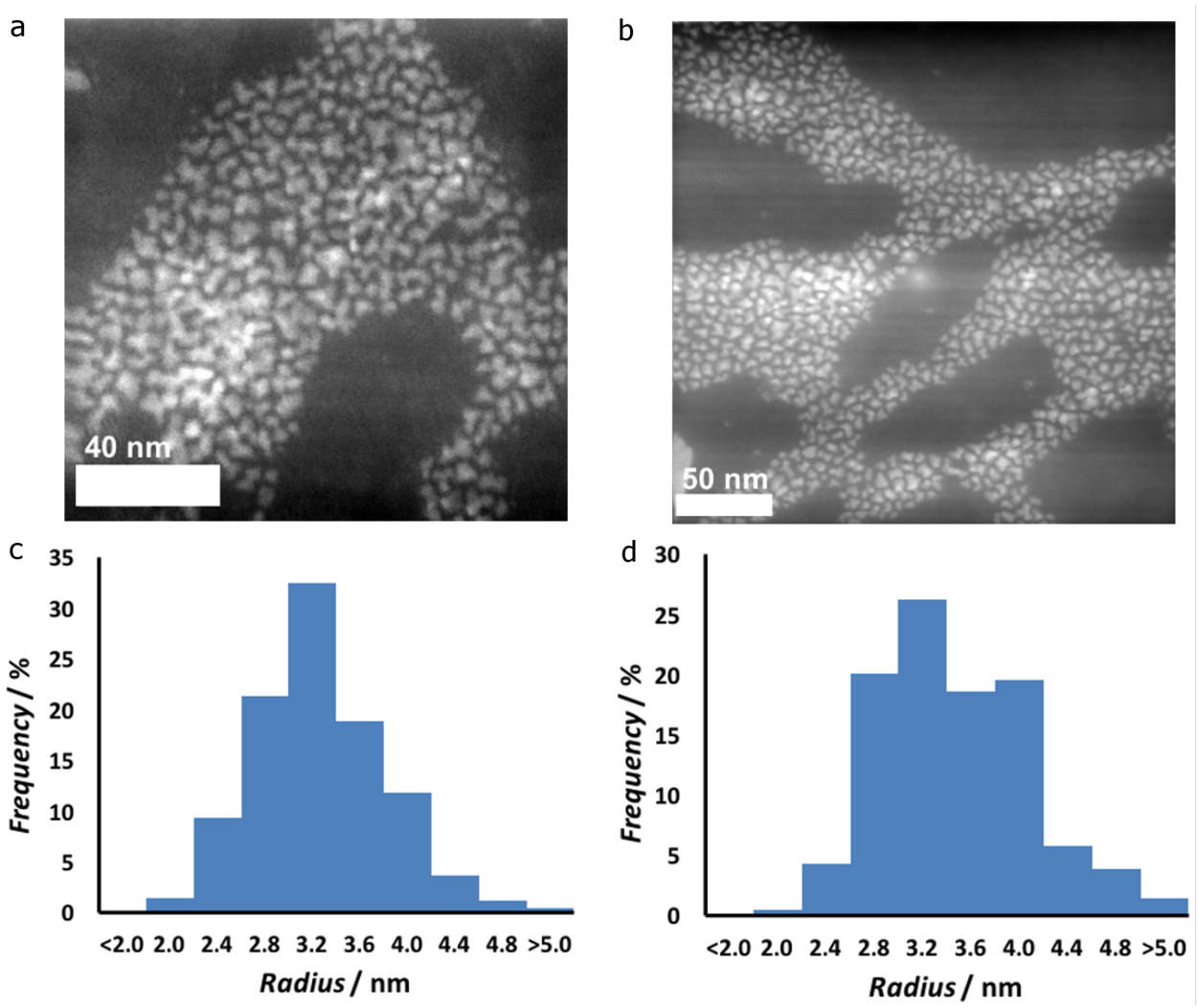

Figure 4.12. (a) STEM image of InP ZnSeS particles (emission peak position – 616 nm, QY – 49%) and the associated size distribution **(c)** for which 280 particles were analyzed. The effective mean diameter was found to be 6.1 ± 1 nm. **(b)** STEM image of InP/ZnSeS particles (emission peak position – 617 nm, QY – 37%) and the associated size distribution **(d)** for which 210 particles were analyzed. The effective mean diameter was found to be 6.5 ± 1.3 nm. Although (a) and (b) have similar emission spectra indicating similar core sizes (~ 2.9 – 3.0 nm), the difference in quantum yield can be attributed to extra thick shell for (b) that might have induced higher strain.

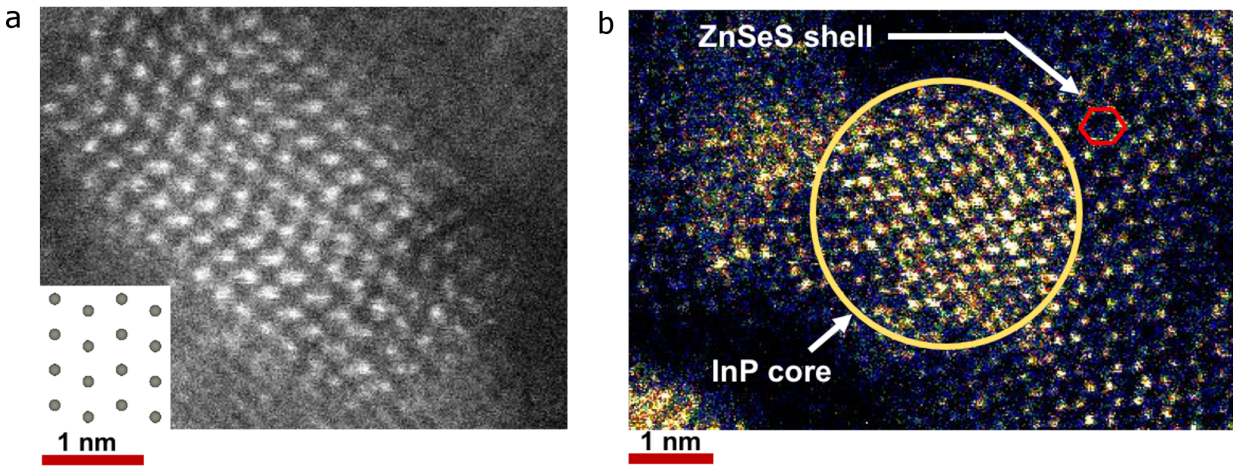

Figure 4.13. (a) HAADF STEM image of InP/ZnSeS particles, the PL spectrum for which is shown in Figure 10. Image clearly shows zinc blende crystal strucutre for ZnSeS shell seen along 010, the analogous arrangement for which is shown on bottom left of the image. **(b)** High contrast denote InP core (~2.9 nm) bounded by a yellow circle. The ZnSeS shell around it indicates hexagonal symmtery associated with zinc blende structure when along 001 direction. The edge of the hexagon (shown in red) is about 3.9 nm long, which is in agreement with the ZnSeS allow lattice parameters.

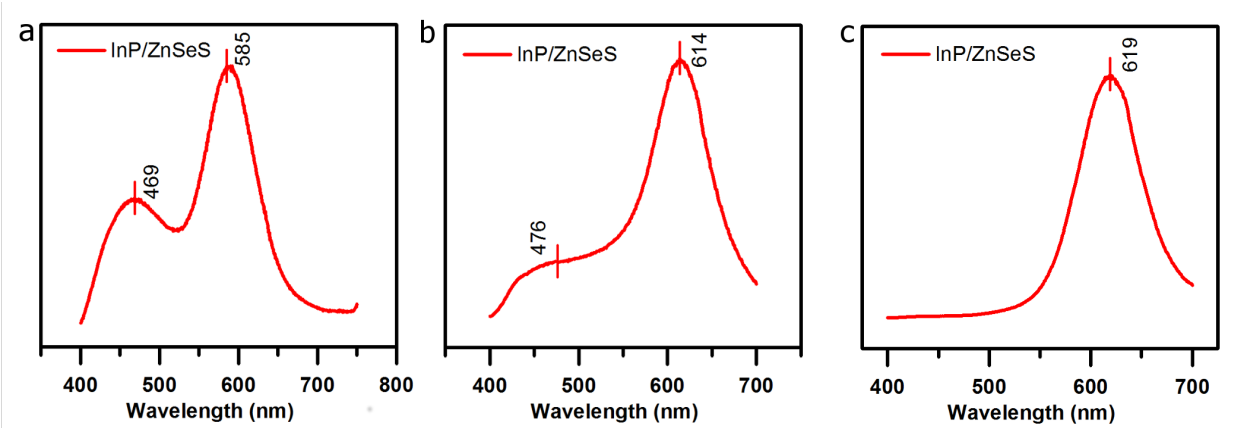

Figure 4.14. The secondary peak in 450 – 475 nm diminishes with the increasing residence time as shown in (a) through (c). **(a)** InP/ZnSeS synthesized at 220 °C (R1), 300 °C (R2), 17m (R1); **(b)** InP/ZnSeS synthesized at 220 °C (R1), 320 °C (R2), 24 m; **(c)** InP/ZnSeS synthesized at 220 °C (R1), 300 °C (R2), 45 m (R2).

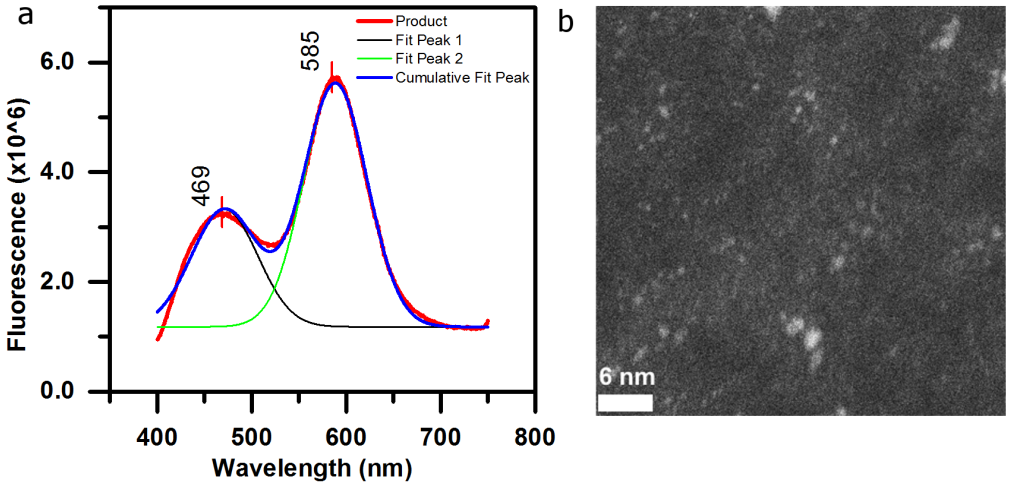

Figure 4.15: (a) Fluorescence spectrum of InP/ZnSeS particles synthesized at 220 °C (R1), 300 °C (R2), 17 min (R1) exhibiting dual peaks at 469 nm and 585 nm. **(b)** Showers of InP/ZnSeS particles with a mean diameter of 2.4 nm confirm the presence of small particles in the product that cause a secondary peak at 469 nm.

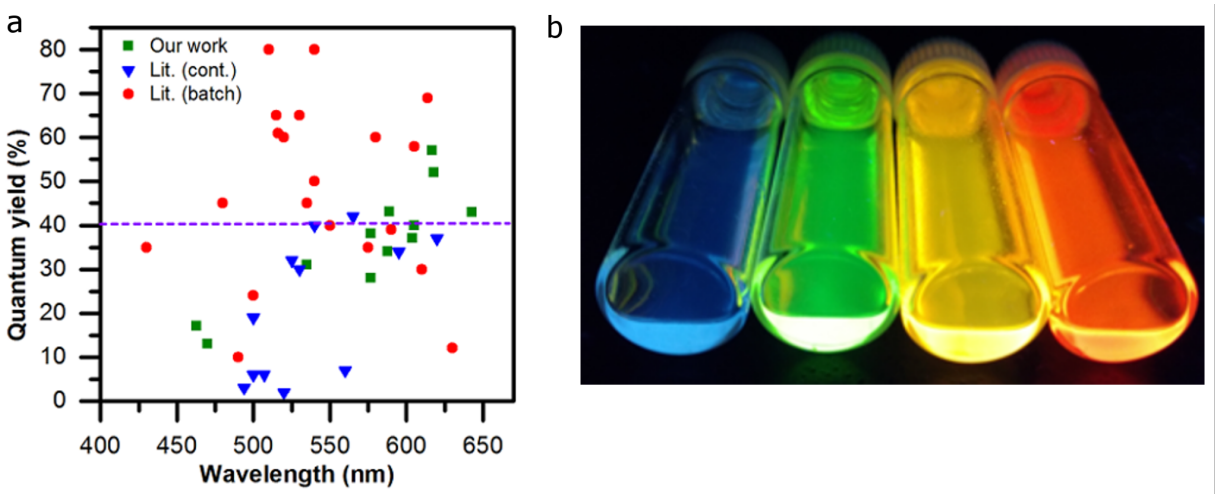

Figure 4.16. (a) A chart showing the quantum yields and the associated wavelengths for different synthesis modes including, batch (red) and continuous techniques (Kenis group – green, literature – blue). The InP/ZnSeS synthesized in our continuous flow reactor exhibits a quantum yield of ~55%, which exceeds all the previous values in the literature achieved in a continuous flow reactor. Furthermore, the high quantum yields achieved in the red region is comparable to the best works on InP-based particles synthesized using batch modes. **(b)** InP/ZnSeS particles of varying sizes that cover the entire visible spectrum synthesized in our continuous flow reactor.

4.9 References

1 Angelatos, G. & Hughes, S. Theory and design of quantum light sources from quantum dots embedded in semiconductor-nanowire photonic-crystal systems. *Phys Rev B* 90, doi:ARTN 20540610.1103/PhysRevB.90.205406 (2014).

2 Beveratos, A., Abram, I., Gerard, J. M. & Robert-Philip, I. Quantum optics with quantum dots Towards semiconductor sources of quantum light for quantum information processing. *Eur Phys J D* 68, doi:ARTN 37710.1140/epjd/e2014-50717-x (2014).

3 Orieux, A., Lemaitre, A., Filloux, P., Favero, I., Leo, G. & Ducci, S. Semiconductor integrated sources of quantum light at room temperature. *Proc Spie* 7945, doi:Artn 79452j10.1117/12.871442 (2011).

4 Pisanello, F., Luigi, M., Lemenager, G., Carbone, L., Bramati, A. & De Vittorio, M. Colloidal Quantum Light Sources Based on Asymmetric Semiconductor Nanocrystals. *Int C Trans Opt Netw* (2012).

5 Rohwer, L. E. S., Abrams, B. L., Wilcoxon, J. P. & Thoma, S. G. Development of solid state light sources based on II-VI semiconductor quantum dots. *P Soc Photo-Opt Ins* 5366, 66-74, doi:10.1117/12.527967 (2004).

6 Shields, A. J. Semiconductor quantum light sources. *Nat Photonics* 1, 215-223, doi:10.1038/nphoton.2007.46 (2007).

7 Yamanishi, M. & Suemune, I. Quantum-Mechanical Size Effect Modulation-Light Sources - a New Field-Effect Semiconductor-Laser or Light-Emitting Device. *Jpn J Appl Phys 2* 22, L22-L24, doi:Doi 10.1143/Jjap.22.L22 (1983).

8 Nam, S., Oh, N., Zhai, Y. & Shim, M. High efficiency and optical anisotropy in double-heterojunction nanorod light-emitting diodes. *Acs Nano* 9, 878-885, doi:10.1021/nn506577p (2015).

9 Oh, N., Nam, S., Zhai, Y., Deshpande, K., Trefonas, P. & Shim, M. Double-heterojunction nanorods. *Nat Commun* 5, doi:10.1038/ncomms4642 (2014).

10 Shim, M. & Guyot-Sionnest, P. Organic-capped ZnO nanocrystals: Synthesis and n-type character. *J Am Chem Soc* 123, 11651-11654, doi:10.1021/ja0163321 (2001).

11 Crooks, R. M., Zhao, M. Q., Sun, L., Chechik, V. & Yeung, L. K. Dendrimer-encapsulated metal nanoparticles: Synthesis, characterization, and applications to catalysis. *Accounts Chem Res* 34, 181-190, doi:10.1021/ar000110a (2001).

12 Tada, H., Kiyonaga, T. & Naya, S. Rational design and applications of highly efficient reaction systems photocatalyzed by noble metal nanoparticle-loaded titanium(IV) dioxide. *Chem Soc Rev* 38, 1849-1858, doi:10.1039/b822385h (2009).

13 Wittenberg, N. J. & Haynes, C. L. Using nanoparticles to push the limits of detection. *Wires Nanomed Nanobi* 1, 237-254, doi:10.1002/wnan.019 (2009).

14 Bally, M. & Voros, J. Nanoscale labels: nanoparticles and liposomes in the development of high-performance biosensors. *Nanomedicine-Uk* 4, 447-467, doi:10.2217/Nnm.09.16 (2009).

15 Sun, C., Lee, J. S. H. & Zhang, M. Q. Magnetic nanoparticles in MR imaging and drug delivery. *Adv Drug Deliver Rev* 60, 1252-1265, doi:10.1016/j.addr.2008.03.018 (2008).

16 Ito, A., Shinkai, M., Honda, H. & Kobayashi, T. Medical application of functionalized magnetic nanoparticles. *J Biosci Bioeng* 100, 1-11, doi:10.1263/jbb.100.1 (2005).

17 Kim, J. Y., Voznyy, O., Zhitomirsky, D. & Sargent, E. H. 25th Anniversary Article: Colloidal Quantum Dot Materials and Devices: A Quarter-Century of Advances. *Advanced materials* 25, 4986-5010, doi:10.1002/adma.201301947 (2013).

18 de Mello Donega, C., Liljeroth, P. & Vanmaekelbergh, D. Physicochemical evaluation of the hot-injection method, a synthesis route for monodisperse nanocrystals. *Small* 1, 1152-1162, doi:10.1002/smll.200500239 (2005).

19 Kwon, S. G. & Hyeon, T. Formation Mechanisms of Uniform Nanocrystals via Hot-Injection and Heat-Up Methods. *Small* 7, 2685-2702, doi:Doi 10.1002/Smll.201002022 (2011).

20 Deka, S., Quarta, A., Lupo, M. G., Falqui, A., Boninelli, S., Giannini, C., Morello, G., De Giorgi, M., Lanzani, G., Spinella, C., Cingolani, R., Pellegrino, T. & Manna, L. CdSe/CdS/ZnS Double Shell Nanorods with High Photoluminescence Efficiency and Their Exploitation As Biolabeling Probes. *J Am Chem Soc* 131, 2948-2958, doi:Doi 10.1021/Ja808369e (2009).

21 Yang, Y. A., Wu, H. M., Williams, K. R. & Cao, Y. C. Synthesis of CdSe and CdTe nanocrystals without precursor injection. *Angew Chem Int Edit* 44, 6712-6715, doi:10.1002/anie.200502279 (2005).

22 Becker, M. A., Radich, J. G., Bunker, B. A. & Kamat, P. V. How Does a SILAR CdSe Film Grow? Tuning the Deposition Steps to Suppress Interfacial Charge Recombination in Solar Cells. *J Phys Chem Lett* 5, 1575-1582, doi:10.1021/jz500481v (2014).

23 <Jensen-Kinetic and Scale-Up Investigations of Epoxide Aminolysis in Microreactors at High Temperatures and Pressures.pdf>.

24 Pathan, H. M., Sankapal, B. R., Desai, J. D. & Lokhande, C. D. Preparation and characterization of nanocrystalline CdSe thin films deposited by SILAR method. *Mater Chem Phys* 78, 11-14, doi:Pii S0254-0584(02)00198-0
Doi 10.1016/S0254-0584(02)00198-0 (2003).

25 Shirasaki, Y., Supran, G. J., Bawendi, M. G. & Bulovic, V. Emergence of colloidal quantum-dot light-emitting technologies. *Nat Photonics* 7, 13-23, doi:10.1038/Nphoton.2013.328 (2013).

26 De Farias, P. M. A., Santos, B. S., Menezes, F. D., Brasil, A. G., Ferreira, R., Motta, M. A., Castro-Neto, A. G., Vieira, A. A. S., Silva, D. C. N., Fontes, A. & Cesar, C. L. Highly fluorescent semiconductor core-shell CdTe-CdS nanocrystals for monitoring living yeast cells activity. *Appl Phys a-Mater* 89, 957-961, doi:10.1007/s00339-007-4267-3 (2007).

27 Kim, Y. K., Ahn, S. H., Cho, Y. S., Chung, K., Choi, C. J. & Shin, P. W. Influence of the Composition of Shell Layers on the Photoluminescence of Cu0.2InS2 Semiconductor Nanocrystals with a Core-shell Structure. *Korean J Met Mater* 49, 900-904, doi:10.3365/Kjmm.2011.49.11.900 (2011).

28 Liu, L. W., Hu, S. Y., Pan, Y., Zhang, J. Q., Feng, Y. S. & Zhang, X. H. Optimizing the synthesis of CdS/ZnS core/shell semiconductor nanocrystals for bioimaging applications. *Beilstein J Nanotech* 5, 919-926, doi:10.3762/bjnano.5.105 (2014).

29 Reiss, P., Protiere, M. & Li, L. Core/Shell Semiconductor Nanocrystals. *Small* 5, 154-168, doi:Doi 10.1002/Smll.200800841 (2009).

30 Xu, S., Ziegler, J. & Nann, T. Rapid synthesis of highly luminescent InP and InP/ZnS nanocrystals. *Journal of Materials Chemistry* 18, 2653-2656, doi:Doi 10.1039/B803263g (2008).

31 Li, L. & Reiss, P. One-pot synthesis of highly luminescent InP/ZnS nanocrystals without precursor injection. *J Am Chem Soc* 130, 11588-+, doi:Doi 10.1021/Ja803687e (2008).

32 Yang, X., Zhao, D., Leck, K. S., Tan, S. T., Tang, Y. X., Zhao, J., Demir, H. V. & Sun, X. W. Full visible range covering InP/ZnS nanocrystals with high photometric performance and their application to white quantum dot light-emitting diodes. *Advanced materials* 24, 4180-4185, doi:10.1002/adma.201104990 (2012).

33 Joung, S., Yoon, S., Han, C. S., Kim, Y. & Jeong, S. Facile synthesis of uniform large-sized InP nanocrystal quantum dots using tris(tert-butyldimethylsilyl)phosphine. *Nanoscale Res Lett* 7, 1-8, doi:Artn 93
10.1186/1556-276x-7-93 (2012).

34 Kim, K., Jeong, S., Woo, J. Y. & Han, C. S. Successive and large-scale synthesis of InP/ZnS quantum dots in a hybrid reactor and their application to white LEDs. *Nanotechnology* 23, doi:Artn 065602 10.1088/0957-4484/23/6/065602 (2012).

35 Yang, S. J., Oh, J. H., Kim, S., Yang, H. & Do, Y. R. Realization of InP/ZnS quantum dots for green, amber and red down-converted LEDs and their color-tunable, four-package white LEDs. *J Mater Chem C* 3, 3582-3591, doi:10.1039/c5tc00028a (2015).

36 Ippen, C., Greco, T. & Wedel, A. InP/ZnSe/ZnS: A Novel Multishell System for InP Quantum Dots for Improved Luminescence Efficiency and Its application in a Light-Emitting Device. *Journal of Information Display* 13, 91-95, doi:10.1080/15980316.2012.683537 (2012).

37 Kim, K., Lee, H., Ahn, J. & Jeong, S. Highly luminescing multi-shell semiconductor nanocrystals InP/ZnSe/ZnS. *Applied Physics Letters* 101, 073107, doi:10.1063/1.4745844 (2012).

38 Lim, J., Bae, W. K., Lee, D., Nam, M. K., Jung, J., Lee, C., Char, K. & Lee, S. InP@ZnSeS, Core@Composition Gradient Shell Quantum Dots with Enhanced Stability. *Chem Mater* 23, 4459-4463, doi:10.1021/cm201550w (2011).

39 Lim, J., Park, M., Bae, W. K., Lee, D., Lee, S., Lee, C. & Char, K. Highly Efficient Cadmium-Free Quantum Dot Light-Emitting Diodes Enabled by the Direct Formation of Excitons within InP@ZnSeS Quantum Dots. *ACS nano* 7, 9019-9026, doi:10.1021/nn403594j (2013).

40 Kim, S., Kim, T., Kang, M., Kwak, S. K., Yoo, T. W., Park, L. S., Yang, I., Hwang, S., Lee, J. E., Kim, S. K. & Kim, S. W. Highly Luminescent InP/GaP/ZnS Nanocrystals and Their Application to White Light-Emitting Diodes. *J Am Chem Soc* 134, 3804-3809, doi:10.1021/ja210211z (2012).

41 Kim, S., Park, J., Kim, T., Jang, E., Jun, S., Jang, H., Kim, B. & Kim, S. W. Reverse Type-I ZnSe/InP/ZnS Core/Shell/Shell Nanocrystals: Cadmium-Free Quantum Dots for Visible Luminescence. *Small* 7, 70-73, doi:10.1002/smll.201001096 (2011).

42 Nightingale, A. M. & de Mello, J. C. Controlled Synthesis of III-V Quantum Dots in Microfluidic Reactors. *Chemphyschem* 10, 2612-2614, doi:10.1002/cphc.200900462 (2009).

43 Baek, J., Allen, P. M., Bawendi, M. G. & Jensen, K. F. Investigation of Indium Phosphide Nanocrystal Synthesis Using a High-Temperature and High-Pressure Continuous Flow Microreactor. *Angew Chem Int Edit* 50, 627-630, doi:10.1002/anie.201006412 (2011).

44 Abolhasani, M., Coley, C. W., Xie, L. S., Chen, O., Bawendi, M. G. & Jensen, K. F. Oscillatory Microprocessor for Growth and in Situ Characterization of Semiconductor Nanocrystals. *Chem Mater* 27, 6131-6138, doi:10.1021/acs.chemmater.5b02821 (2015).

45 Xie, L. S., Harris, D. K., Bawendi, M. G. & Jensen, K. F. Effect of Trace Water on the Growth of Indium Phosphide Quantum Dots. *Chemistry of Materials* 27, 5058-5063, doi:10.1021/acs.chemmater.5b01626 (2015).

46 Ippen, C., Schneider, B., Pries, C., Kropke, S., Greco, T. & Hollander, A. Large-scale synthesis of high quality InP quantum dots in a continuous flow-reactor under supercritical conditions. *Nanotechnology* 26, doi:Artn 085604 10.1088/0957-4484/26/8/085604 (2015).

47 Jensen, K. F. Microreaction engineering - is small better? *Chem Eng Sci* 56, 293-303, doi:Doi 10.1016/S0009-2509(00)00230-X (2001).

48 Watts, P. & Haswell, S. J. The application of micro reactors for organic synthesis. *Chemical Society reviews* 34, 235-246, doi:10.1039/b313866f (2005).

49 Haswell, S. J., Middleton, R. J., O'Sullivan, B., Skelton, V., Watts, P. & Styring, P. The application of micro reactors to synthetic chemistry. *Chemical communications*, 391-398, doi:Doi 10.1039/B008496o (2001).

50 Knitter, R., Gohring, D., Risthaus, P. & Hausselt, J. Microfabrication of ceramic microreactors. *Microsystem Technologies* 7, 85-90, doi:Doi 10.1007/S005420100107 (2001).

51 Fogler, H. S. *Elements of Chemical Reaction Engineering*. (1987).

52 Levenspiel, O. *Chemical Reaction Engineering*. (Wiley, New York, 1972).

53 Bhunia, S. K., Saha, A., Maity, A. R., Ray, S. C. & Jana, N. R. Carbon Nanoparticle-based Fluorescent Bioimaging Probes. *Sci. Rep.* 3 (2013).

54 Allen, P. M., Walker, B. J. & Bawendi, M. G. Mechanistic Insights into the Formation of InP Quantum Dots. *Angew Chem Int Edit* 49, 760-762, doi:10.1002/anie.200905632 (2010).

55 Xie, R. G., Li, Z. & Peng, X. G. Nucleation Kinetics vs Chemical Kinetics in the Initial Formation of Semiconductor Nanocrystals. *J Am Chem Soc* 131, 15457-15466, doi:Doi 10.1021/Ja9063102 (2009).

56 Gary, D. C., Terban, M. W., Billinge, S. J. L. & Cossairt, B. M. Two-Step Nucleation and Growth of InP Quantum Dots via Magic-Sized Cluster Intermediates. *Chem Mater* 27, 1432-1441, doi:10.1021/acs.chemmater.5b00286 (2015).

57 Thomas, A., Nair, P. V. & Thomas, K. G. InP Quantum Dots: An Environmentally Friendly Material with Resonance Energy Transfer Requisites. *J Phys Chem C* 118, 3838-3845, doi:10.1021/jp500125v (2014).

58 Mordvinova, N. E., Vinokurov, A. A., Lebedev, O. I., Kuznetsova, T. A. & Dorofeev, S. G. Addition of Zn during the phosphine-based synthesis of indium phospide quantum dots: doping and surface passivation. *Beilstein J Nanotech* 6, 1237-1246, doi:10.3762/bjnano.6.127 (2015).

59 Jang, E., Jun, S. & Pu, L. High quality CdSeS nanocrystals synthesized by facile single injection process and their electroluminescence. *Chem Commun*, 2964-2965, doi:10.1039/b310853h (2003).

60 Naughton, M. S., Kumar, V., Bonita, Y., Deshpande, K. & Kenis, P. J. A. High temperature continuous flow synthesis of CdSe/CdS/ZnS, CdS/ZnS, and CdSeS/ZnS nanocrystals. *Nanoscale* 7, 15895-15903, doi:10.1039/c5nr04510j (2015).

61 Yang, H. & Holloway, P. H. Efficient and photostable ZnS-Passivated CdS : Mn luminescent nanocrystals. *Adv Funct Mater* 14, 152-156, doi:10.1002/adfm.200305011 (2004).

62 Talapin, D. V., Gaponik, N., Borchert, H., Rogach, A. L., Haase, M. & Weller, H. Etching of colloidal InP nanocrystals with fluorides: Photochemical nature of the process resulting in high photoluminescence efficiency. *J Phys Chem B* 106, 12659-12663, doi:10.1021/jp026380n (2002).

63 Hotje, U., Rose, C. & Binnewies, M. Lattice constants and molar volume in the system ZnS, ZnSe, CdS, CdSe. *Solid State Sci* 5, 1259-1262, doi:10.1016/S1293-2558(03)00177-8 (2003).

64 Allen, P. M., Walker, B. J. & Bawendi, M. G. Mechanistic insights into the formation of InP quantum dots. *Abstr Pap Am Chem S* 239 (2010).

65 Wang, F. D., Richards, V. N., Shields, S. P. & Buhro, W. E. Kinetics and Mechanisms of Aggregative Nanocrystal Growth. *Chem Mater* 26, 5-21, doi:10.1021/cm402139r (2014).

66 Shields, S. P., Richards, V. N. & Buhro, W. E. Nucleation Control of Size and Dispersity in Aggregative Nanoparticle Growth. A Study of the Coarsening Kinetics of Thiolate-Capped Gold Nanocrystals. *Chem Mater* 22, 3212-3225, doi:10.1021/cm100458b (2010).

67 Van Hyning, D. L., Klemperer, W. G. & Zukoski, C. F. Silver nanoparticle formation: Predictions and verification of the aggregative growth model. *Langmuir* 17, 3128-3135, doi:10.1021/la000856h (2001).

68 Talapin, D. V., Rogach, A. L., Haase, M. & Weller, H. Evolution of an ensemble of nanoparticles in a colloidal solution: Theoretical study. *J Phys Chem B* 105, 12278-12285, doi:10.1021/jp012229m (2001).

4.10 Supplementary information

Operating protocol for the synthesis of InP/ZnSeS nanoparticles in the multistep continuous flow reactor.

1. Known amounts of Zinc Acetate, oleic acid, ZnDDTC and octadecene for both core and shell precursor flasks were measured. Similarly, in the glove box, known amounts of TMSP, TOP-S, or TOP-Se were measured.
2. The core and shell precursor contents were mixed continuously and solid particles were dissolved by raising the temperature.
3. Valves V-1 and V-8 were closed, and three 10-minute vacuum cycles and 1-minute nitrogen cycles were performed alternatively.
4. Valves V-1 and V-8 were opened and nitrogen was flushed through both the reactors.
5. Valves V-1 and V-8 were closed after the nitrogen flush.
6. Step 3 was repeated to ensure good inert conditions in the three-neck flasks.
7. The air-tight collection vial is flushed with nitrogen. The flushed nitrogen is vented through the back pressure regulator.
8. The back pressure regulator is set to maintain desired back pressure in the reactors. and
9. The contents from the glovebox are added to the respective three-neck flasks.
10. Valves V-1 and V-8 were opened to let the reactants flow through the reactors at a set flow rate maintained by the peristaltic pumps
11. Valve V-4 was opened to allow the products to flow in the collection vial.

CHAPTER 5
FAST MILLIFLUIDIC STATIC MIXER FOR NANOPARTICLE SYNTHESIS*

5.1 Introduction

Abstract. Nanoparticles find use in various applications ranging from electronics (light emitting diodes, photovoltaics) to catalysis, biolabeling. Typically, these particles are produced via batch synthesis routes that are hampered by issues such as slow mixing, and lack of batch-to-batch reproducibility. These issues escalate further when attempting to scale up for production. Here, we report on a fast millifluidic static mixer that enables synthesis of uniform nanoparticles at operating flow rates as high as 10 ml/min. The applicability of the mixer was validated by synthesizing uniform gold nanoparticles without the use of any stabilizers or surfactants, thereby reducing any post-synthesis steps. The developed static mixer was used to synthesize uniform gold nanoparticles of different size, ranging from 39 to 57 nm (based on Dynamic Light Scattering data) by changing the operating flow rates, thereby demonstrating robust and effective mixing at various flow rates. Additionally, the mixer exhibited lower variation in the mean particle size for syntheses conducted at different times compared to the batch synthesis technique, thus addressing the reproducibility issue associated with the batch synthesis routes. The mixer was fabricated utilizing conventional machining approaches as opposed to any special, tedious fabrication process with controlled environment often associated with silicon-glass, glass, and ceramic reactors. Easy fabrication process will enable quick and fast

*This chapter has been adapted from the following manuscript in preparation: V. Kumar, J. Whittenberg, K. Lane , S. Verma, P.J.A. Kenis, "Fast millifluidic static mixer for nanoparticle synthesis".

manufacturing of customized mixers tailored specifically for different processes that will be extremely beneficial in scaling up the production process of nanoparticles.

Easy fabrication technique ensures low cost of production along with good prospects for scale-up production of the mixers. The total unoptimized cost (including the fabrication and materials cost) of the mixer was about ~$100, which is much cheaper than a comparable commercial mixer that costs over $1000. The design for the static mixer was optimized using Finite Element Modeling, which was found to be in agreement with the experiments.

Nanomaterials are being considered as the active elements in many applications, including optoelectronics[1-10], photocatalysis[11,12], biolabelling and bioimaging[13-15], therapeutics[15,16]. In each of these fields, the size-controlled physical and chemical properties of nanocrystals is harnessed to improve on conventional bulk materials in terms of chemical reactivity, magnetic, optical, or electronic behaviour. In all cases, this requires tightly specified nanocrystals of well-defined size, shape, composition and crystallinity[17-19]. In order to realize the full potential of nanomaterials, it is critical to have an efficient, reproducible synthesis technique of the nanoparticles. Currently, the majority of the synthesis of these nanomaterials happens in batch modes. In general, the batch synthesis techniques are known to produce great results on small scales (< 10 ml), which is sufficient to study the fundamental properties of the nanomaterials[17]. However, the batch techniques suffer from various disadvantages including slow heating/cooling, slow mixing, and the lack of batch-to-batch reproducibility[18,20,21] issues, which escalate further with the scale of the synthesis. It is imperative to maintain high standards in terms of the quality at high production levels for the nanomaterials to be a commercial success.

In the wake of such tight requirements on nanoparticle quality and synthesis, continuous flow synthesis, especially microfluidics has emerged as a viable technique to synthesize high quality

nanoparticles on a continuous scale. The small channel sizes (~10's μm) of microfluidic platforms enable superior control over nanoparticle size, morphology and composition due to fast heat and mass transfer at these length scales[19,22-26]. Microfluidics has been widely applied to a range of chemistries including, metal nanoparticles[27-29], semiconductor nanoparticles[20,30-32], polymer nanoparticles[33,34], ceramic nanoparticles[35-37], and even protein[38,39] and pharmaceutical[40,41] crystallizations with great success. Although microfluidics approach has contributed greatly to understanding the physical and chemical processes involved in synthesizing (and functionalizing) high-quality nanoparticles with high precision, it still fails to address the large scale production issues[42]; the operating flow rates in microfluidic reactors hover around tens of microliters a minute[19]. To address the issue of low throughput, a major push towards the application of millifluidic reactors for the synthesis of nanomaterials in place of microfluidic approach is currently underway. Millifluidic techniques are expected to marry the benefits of a microfluidic reactor while operating at higher flow rates. Despite its immense potential, millifluidic approach has been applied with limited success only to a few chemistries such as Gold NPs[43,44], Cd-based QDs[45], Copper nanoclusters[46] where fast mixing was either not required or intentionally not implemented given the complexity of the problem. A recent work on gold nanoparticles underscored the immediate need for good, inexpensive fast mixers to obtain high quality nanoparticles[43]. A few works in the literature report on circumventing the problem of fast mixing by the use of multiphase flows (droplets)[32,47] and impinging jet mixers, and turbulent jet mixers[48]. However, droplet mixing generally involves a carrier liquid, typically fluorocarbon-based liquids that pose potential contamination issues[19]. Furthermore, the window of operable flow rates is narrow for obtaining a stable train of uniform droplets hampering the robustness of this technique[49-51]. Most of the synthesis demonstrated in droplet-based reactors are

single-step synthesis in nature, which highly restricts the use of these reactors[52]. Similarly, impinging jet mixers require fast flow rates and incur high pressure drops to achieve effective and fast mixing[53,54]. In general, both these techniques are not robust enough to accommodate a wide range of flow rates suitable for millifluidic reactors.

In this work, we report on static mixers that can operate under a wide range of flow rates, in particular, 0.2 ml/min to 10 ml/min demonstrated by us. The mixer has been shown to achieve complete mixing in about 0.8 sec for flow rates as high as 4 ml/min. The mixer is based on the staggered herringbone design, which was further optimized using Finite Element Modeling for the operating length scales. The mixer design was validated by synthesizing uniform gold nanoparticles. The size of the gold nanoparticles could be changed from ~15 nm to 30 nm (based on the TEM images) by varying the flow rates of the precursors. No capping ligands were used in the synthesis, thereby reducing any further post-synthesis steps. The product obtained from the developed static mixer exhibited lower polydispersity index (PDI) values indicating more uniform products compared to the batch synthesis technique. Furthermore, the static mixer produced more consistent results for synthesis conducted at different times compared to the batch synthesis mode. The static mixer was fabricated using conventional milling machine, thereby obviating the need for any specialized fabrication facilities often associated with silicon-glass[24], glass[55,56], and ceramic[57] reactors. This greatly reduces the cost of the mixer compared to commercially available static mixers that typically cost over $1000. Easy fabrication procedure coupled with low cost of production allow for potential scale-up production of the mixer.

5.2 Materials and methods

Gold (III) chloride hydrate (product number: 254169, purity: 99.999% trace metals basis, supplier: Sigma Aldrich) was used as the precursor for gold nanoparticles and L-ascorbic acid (product number: A5960, purity: ≥99.0%, supplier: Sigma Aldrich) was used as the reducing agent. For a typical synthesis, a 0.375 mM gold (III) chloride hydrate solution and 6 mM ascorbic acid solution in E-pure water (> 18.1 MΩ cm) were used as the two inlets for the micromixer.

Nanoparticle size characterization. The dynamic light scattering (DLS) experiments were performed using a Malvern zetasizer nano instrument at 25 °C. The instrument uses a 633 nm red laser to perform the back light scatter. The gold nanoparticle sample collected from the micromixer outlet was used as is for the DLS experiments. The different nanoparticle solutions were imaged using TEM.

Device fabrication. Mixing devices were fabricated from 3 mm thick poly(methyl methacrylate) (PMMA) sheets (Astari Niagra International) except for the bottom substrate of the device used for confocal images which was a 0.175 mm thick PMMA sheet (Goodfellow). Sylgard 184 polydimethylsiloxane(PDMS) (Dow Corning) sheets were utilized during the bonding process. A plasma cleaner (Harrick, model PDC-001) and hot press (Carver, model 3851) were utilized to bond the PMMA together via heat and pressure.

10-32 coned NanoPort assemblies for 1/16" OD tubing (IDEX) and 20 gauge Teflon tubing (Allied Electronics) were used to interface devices with 50 mL glass syringes (Hamilton) or 60 mL Luer-Lok tip plastic syringes (Becton, Dickinson and Company). Flow rates were controlled by either a PHD 2000 syringe pump (Harvard Apparatus) or Milliliter Flow pumps (Harvard

Apparatus). Images of the mixing process were captured on a Leica microscope (Leica, model M205 C) using a Leica camera (Leica, model DFC295) and Leica Application Suite v.3.8.0 (Leica). ImageJ v.1.48v was utilized to quantify mixing.

Isopropanol (Sigma) was utilized for removing air pockets from reactors. Fast Green FCF (Sigma) and Amaranth (Sigma) were both dissolved in commercially available 1x PBS without magnesium and calcium (Corning). Dipotassium and monopotassium phosphate (Sigma) were dissolved in water purified in-house (E-Pure) to make the 50 mM phosphate buffer used for the 500 μM fluorescein (Sigma) solutions utilized in confocal microscopy experiments. The 50 mM fluorescein stock solution was dissolved in dimethyl sulfoxide (DMSO) (Macron Fine Chemicals). A LSM 700 confocal microscope (Zeiss) was utilized for confocal microscopy experiments and Imaris v.8.1.2 was used to capture slices of the confocal images.

Mixer fabrication. Fabrication of short devices started by cutting a 68 x 113 mm and a 58 x 103 mm piece of 3 mm thick poly(methyl methacrylate) (PMMA) from a PMMA sheet. Long devices consisted of 76 x 113 mm and 66 x 103 mm pieces. The larger PMMA piece is a blank to enclose the channels and was not machined. The channel and herringbone features were etched into the smaller top piece using conventional CNC milling techniques, and through holes were drilled at both inlets and the outlet using a 1.20 mm drill bit. The edges around the drilled holes were sanded carefully to remove burrs that may impact PMMA bonding. Both sheets of PMMA were then scrubbed with an aqueous Alconox solution and rinsed with E-Pure water (18.0 MΩ·cm) then isopropanol, and finally dried with a stream of nitrogen.

Immediately prior to bonding both PMMA sheets were placed in a plasma cleaner for 2 min at 500 mTorr to reduce bonding temperature and improve bonding strength.[1] The sheets were

then quickly assembled into the following assembly in order: (1) an aluminum block, (2) a PDMS sheet, (3) the PMMA blank piece, (4) the PMMA piece with milled features, (5) a PDMS sheet, and (6) an aluminum block. The entire assembly was placed in a hot press preheated to 95 °C. A pressure of 2900 kPa was applied for 40 min, and then the hot press was shut off and allowed to cool for 3 h before removing the PMMA device.

Placement of PDMS sheets, a deformable polymer, on either side of the PMMA pieces improved bonding by evenly applying force to the PMMA. Without PDMS present large sections of PMMA did not bond. The sheets were fabricated by pouring a degassed mixture of PDMS (10:1 ratio monomer to curing agent) on top of 2 clean glass plates with tape walls to contain the PDMS. The PDMS was baked overnight in a 65 °C oven and removed from the glass plates.

The device used for confocal microscopy was fabricated in an almost identical fashion except a 0.175 mm thick piece of PMMA was used for the bottom substrate. Additionally, a thin sheet (~0.5 mm) of titanium was inserted between the bottom sheet of PDMS and the thin sheet of PMMA to prevent the PDMS from pushing the thin PMMA sheet upwards, causing the channel to collapse.

NanoPorts were attached to both inlets and the outlet to enable injection of fluids and sample collection. The PMMA surface was first cleaned with IPA, and then the NanoPorts with gaskets underneath were lined up with each inlet or outlet. The NanoPorts were held in place using a binder clip and a 2-part epoxy was applied around the edges of the NanoPorts. The epoxy was allowed to cure overnight prior to using the mixer.

Mixing characterization. Mixing was quantified by injecting two aqueous dye solutions through the herringbone device. A 0.5 mM Fast Green FCF solution was prepared by mixing 0.182 g in 450 mL of 1x phosphate-buffered saline (1x PBS) and a 2 mM Amaranth solution was similarly prepared by dissolving 0.544 g in 450 mL of 1x PBS. Dyes were dissolved in PBS to ensure a consistent pH and ionic strength. Solutions were stored in amber glass containers in a 4 °C refrigerator when not in use for up to 3 months.[2] Solutions were injected into the device using syringes and 20 gauge Teflon tubing attached to NanoPort ferrules. Flow rates were controlled by either a PhD 2000 (dye solutions) or Milliliter Flow (water and isopropanol) pump. Prior to injecting dye solutions isopropanol was first injected through devices between ~0.6 – 1.5 mL/min to clear any air pockets out of the device followed by water (~0.6 mL/min) to remove isopropanol. When changing between different solvents care was taken to ensure NanoPorts were completely filled with fluid before attaching the next solvent line to prevent introducing air into the device.

Dye solutions were then injected through the short or long device, Fast Green FCF in one inlet and Amaranth in the other inlet. Prior to collecting data an image was analyzed to ensure intensity values were not saturated (i.e., not at the minimum or maximum value). 11 images were captured with a 2 s wait before capturing the next image at 5 different locations for the short mixer and 4 different locations for the long mixer. The flow rate was adjusted and the process was repeated for each additional flow rate. The device was cleaned with isopropanol, then water, and finally air was injected through the device prior to storage. This whole process was repeated on two separate dates for a total of three trials.

Images were analyzed using ImageJ (version 1.48v) using custom macros we developed to accelerate the analysis process. The captured images were split into 8-bit red, green, and blue channels, and the red channel was utilized for quantifying mixing. A line was drawn across the channel, orthogonal to the fluid flow, and a single column of intensity values was gathered from the line for each red channel image, ignoring ~20 μm of data on either side of the channel to avoid edge affects. The coefficient of variation (CoV) was calculated at each position for each trial (set of 11 images) using Equation 4.

Confocal microscopy. A 50 mM potassium phosphate buffer solution was prepared and the pH was adjusted to 8.00, and a stock solution of 50 mM fluorescein was prepared by dissolving 0.166 g in DMSO. A 500 μM solution of fluorescein was created by adding 1 mL of 50 mM fluorescein to 99 mL of phosphate buffer, pH 8.00. The syringe pump set-up and preparation was identical to the brightfield microscopy only the confocal device (0.175 mm thick PMMA bottom) was used instead and 500 μM fluorescein was injected into one inlet and 50 mM phosphate buffer in the other. Confocal images were collected using a 20x objective at different locations, all at a total flow rate of 0.2 mL/min. Cross-sections of each image were captured using Imaris x64 software (version 8.1.2) to analyze mixing in the z-direction.

On-Chip and off-chip gold nanoparticle synthesis. 6 mM ascorbic acid and 0.375 mM chloroauric acid solutions were prepared in E-Pure water immediately prior to nanoparticle synthesis experiments. Short or long mixers were prepared as discussed previously by injecting isopropanol then water to clear any air pockets from the devices. Then ascorbic acid and chloroauric acid were injected in separate inlets at equal flow rates. A new short or long mixer was used for each flow rate in Figures 5.9. Four separate 4 mL samples were collected at each flow rate for short and long devices, waiting 1 min in between each collection. DLS was utilized to analyze the hydrodynamic radius of particles in each sample. The average hydrodynamic radius and standard deviation was determined using the 4 separate samples at each flow rate. Off-chip nanoparticle synthesis was performed by directly adding 2 mL of 6 mM ascorbic acid to 2 mL of 0.375 mM chloroauric acid and immediately vortex mixing for 1 min. This was repeated two more times for a total of three samples. Hydrodynamic radius was determined by DLS for off-chip synthesis samples as well.

5.3 Finite Element Modelling and optimization

Three-dimensional CFD simulations of the static mixer were performed on COMSOL Multiphysics software. "Single-phase laminar flow" and "transport of diluted species" modules were coupled in COMSOL in order to solve Naviér-Stokes (N-S) equation (1), mass balance equation (2), and convective-diffusion (3) for incompressible fluid.

$$\boldsymbol{\rho(v.\nabla)v - \nabla.\eta(\nabla v + (\nabla v)^T) + \nabla p = 0} \quad (1)$$

$$\boldsymbol{\nabla.v = 0} \quad (2)$$

$$\boldsymbol{\mathcal{D}\nabla^2 c - v.\nabla c = 0} \quad (3)$$

In the above equations, ρ denotes density (kg/m^3), v is the velocity vector (m/s), η denotes viscosity (Pa s), p equals pressure (Pa), $\mathcal{D}$ denotes the diffusion coefficient (m^2/s) and c represents the concentration (mol/m^3). The following fluid properties were used in the simulation; water (stream1) – density: 1,000 kg/m^3, dynamic viscosity: 0.89 mPa-s, concentration: 1 M; water (stream2) – density: 1,000 kg/m^3, dynamic viscosity: 0.89 mPa-s, concentration: 0 M. The diffusion coefficient was kept as 10^{-9} m^2/s for both the streams, which is in agreement with the common values found in literature.[20]We ensured that the physical properties of the two streams do not change with the concentration of water molecules.

Two sets of simulations were carried out – (1) optimization exercise and (2) full-channel simulation. The optimization exercise was performed with just 1 herringbone structure (**Figure 5.1a**) to optimize the width, depth. We then used two herringbones to optimize the distance between two consecutive herringbones. Once the optimum dimensions were known, a simulation was performed to evaluate the extent of mixing for a device containing 12 herringbones (in sets of 3) with optimum dimensions, which we will refer to as the full-channel simulation. The number 12 was specifically chosen as it enables the use of at least two groups of alternate asymmetric herringbone sets, while minimizing the computation time for such a configuration. The maximum edge length for the tetrahedral mesh element was fixed at 0.02 mm for the herringbone grooves and 0.08 mm for the rectangular channel for all the simulations with 1 SHM (optimization exercise) resulting in a total of 274380 domain elements, 11391 boundary elements, and 550 edge elements. Similarly, the maximum size for the tetrahedral mesh element was fixed at 0.03 mm for the herringbone grooves and 0.08 mm for the channel resulting in 116,4619 tetrahedral elements, 69392 triangular elements, 3914 edge elements, and 180 vertex

elements for all the full-channel simulations with 12 SHMs. The mesh was calibrated for fluid dynamics physics for all the simulations used in this work.

The concept of Coefficient of variation (CoV) was used to estimate the level of mixing. Furthermore, we considered 95% mixing as the state of complete mixing[20]. CoV was calculated at outlet (past the flow focusing region) for various conditions to account for differences in the extent of mixing. The mixing times were estimated by calculating the time required to reach 95 % mixing for different conditions.

$$\frac{\sqrt{\frac{\int_0^{0.2}(c-\bar{c})^2.dl}{0.2}}}{\bar{c}} \tag{4}$$

In Equation 4, c denotes the concentration of water at the point on the cross-section where CoV is evaluated and $\bar{c}$ denotes the concentration of water in a fully mixed state that is calculated using the following formula

$$\bar{c} = \frac{v_1 c_{1,i} + v_2 c_{2,i}}{v_1 + v_2} \tag{5}$$

In Equation 5, v_1 and v_2 are the linear volumetric flow velocities of the two water streams in the channel, respectively. $c_{1.i}$ and $c_{2.i}$are the respective concentrations of H_20 in the inlet water streams. Reynolds number was calculated using the following formula

$$\mathbf{Re} = \frac{vl}{\nu} \tag{6}$$

where ν, l, and υ are total linear flow velocity, characteristic length scale, and kinematic viscosity of the water stream in the channel.

Optimization exercise. The optimization exercise was performed in two stages. In the first stage, we worked with only one herringbone to find optimum values for the width and depth of the staggered herringbone. In the second stage, we worked with two herringbones to optimize the distance between two consecutive herringbones. Some reports in the literature show that the optimum asymmetry in terms of the ratio of the lengths of each branch of a herringbone configuration lies at 1:2[58,59]. The optimum angle at which the arms meet the channel walls has been shown to be 45°[60]. We used the optimum asymmetry and angle for the herringbones as previously shown in the literature for all our simulations.

To optimize the dimensions of staggered herringbone design, CoV (equation 4)[59] was chosen as the response variable. CoV, in layman terms, indicates the extent of variation of a quantifiable metric in an ensemble and therefore, lower CoV represents lower ensemble variation and high uniformity. Essentially, CoV varies inversely with the extent of mixing and it has been widely accepted as a suitable representative of the extent of mixing for static mixers. The width and depth of the herringbone were varied from 200 μm to 900 μm and the respective CoV was calculated at the outlet of the channel. Based on the simulation, 400 μm and 600 μm yielded the lowest CoVs, therefore making the optimum values. A less deep herringbone is insufficient to promote lateral velocities in the flowing stream that are orthogonal to the direction of the flow, whereas a very deep herringbone results in a lot of dead zones resulting into inefficient mixing. The lateral velocities produced in the flowing streams due to herringbone grooves facilitate mixing. Therefore, an optimum depth and width exists at which the maximum mixing occurs (**Figure 5.2a-b**). As a next step, the distance between the subsequent herringbones was optimized (**Figure 5.2c**) Groove width seems to be the most sensitive parameter as its effect on the CoV (and mixing) is the highest per unit change in the width dimensions. Once all the

dimensions were optimized, more simulations were run with a set of 12 herringbones in the groups of 3, 2, and 4 to see find the optimum number of herringbones in one set. However, groups of 3 and 4 herringbones showed almost equal mixing which was slightly greater than the set of 2 herringbones. Finally, 12 herringbones in 4 sets of 3 (**Figure 5.1b**) were simulated with optimized herringbone dimensions as shown in for the full-channel simulation.

5.4 Results and discussion

Device characterization. A *long device* consisting of 156 herringbones in sets of 3 (**Figure 5.3b**) and a *short device* consisting of 42 herringbones in sets of 3 (**Figure 5.3a**) were fabricated. Two sets of 3 herringbones each make one full cycle. Mixing effectiveness was characterized for both devices by injecting different dyes (FCF Fast Green and Amaranth) dissolved in phosphate-buffered saline (PBS) in separate inlets (**Figure 5.4**). The short device exhibited full mixing (CoV ~ 0.05) for flow rates ranging from 0.2 ml/min to 2 ml/min (**Figure 5.5a-b**). However, incomplete mixing was observed for flow rates greater than 2 ml/min. The initial CoV is less than 1 in **Figure 5.7a** because CoV is concentration dependent. Similarly, we characterized the long devices with the same set of dyes to accommodate a greater range of flow rates, ranging from 0.2 ml/min to 13 ml/min. We observed full mixing for flow rates up to 10 ml/min. To demonstrate repeatability each flow rate was tested 3 separate times. To reduce any systemic errors, we used the same syringe pumps and the glass syringes for each experiment. Additionally, 11 separate images were taken to obtain an average dye intensity at each location in the device. The experiments were found to be in good agreement with the simulation results; both the experiments and the simulation exhibited very similar flow patterns (**Figure 5.6**).

We performed confocal microscopy to better understand (and visualize) mixing in the bulk of the liquid facilitated by the lateral velocities generated by the herringbone grooves (**Figure 5.5**). As

demonstrated in the simulations, the asymmetric herringbones promote lateral velocities orthogonal to the flow direction that help form striations or lamellae in the bulk of the liquid. As the streams flow through different sets of herringbones, these striations divide further into thinner bands, thereby reducing the diffusive distance between the alternate bands of unmixed regions. These observations indicate mixing via convective advection that grows exponentially (instead of linearly) with the mixing distance. This is well illustrated in **Figure 5.7a-b** where we see an exponential decay of CoV[60]. The exponential decay of CoV with number of cycles can be explained by assuming that the number of unmixed bands increases 2 folds with every turn[60], which results in the reduction of the diffusive distance by 2 times. Therefore, by the end of the N^{th} cycle, the effective diffusive distance should have reduced by an order of 2^N (Equation 8). Since higher CoV essentially means higher "unmixedness" therefore, CoV can be assumed to be proportional to the time (τ_{mix}) it would take to mix two unmixed regions with an effective diffusive distance, W_{eff}.

$$\boldsymbol{CoV_0 \sim \tau_{mix,0} = \frac{w^2}{D}} \tag{7}$$

After N cycles of herringbones,

$$\boldsymbol{w_{eff,n} = \frac{w}{2^N}} \tag{8}$$

$$\boldsymbol{CoV_n \sim \tau_{mix,n} = \frac{w_{eff}^2}{D} = \frac{w^2}{2^{2N}D}} \tag{9}$$

CoV_0 is the coefficient of variation at the starting point of the mixer where there is no mixing, making $CoV_0 = 1 \; or \; a \; constant$. Therefore, CoV decays exponential with the number of herringbone cycles, N as shown in equation 10.

$$\boldsymbol{\frac{CoV_n}{CoV_0} = \frac{CoV_n}{1} = \frac{1}{2^{2N}}} \tag{10}$$

Gold nanoparticle synthesis. In order to validate the design, we chose to synthesize gold nanoparticles without any capping agents in the fabricated static mixer. The gold nanoparticle chemistry (without any capping agent) was selected for the reaction is fast[61] (< 0.1 s), thereby allowing us to demonstrate the importance of fast mixing properties of the static mixer at high volumetric flow rates. We performed the gold nanoparticle synthesis for the flow rates (total) of 0.2, 0.6, 2 and 4 mL/min in the short device (Figure 9). The product was then analyzed using dynamic light scattering technique to characterize hydrodynamic diameter of the gold nanoparticles for each tested flow rate. We found that the hydrodynamic diameter of the gold nanoparticles increased with the flow rate, which was counterintuitive as lower residence times are expected to produce smaller particles due to low reaction times. A possible explanation for the anomalous trend could be an incomplete reaction in the device. The fast flow rates result in a very short residence time in the short device (**Table 5.1**), which may lead to incomplete reaction in the device. The left over precursors in the collection vial may react further resulting in unregulated growth or ripening of the formed gold nanoparticles. Ripening of the unmixed (no mixing occurs in the collection vial post the effluents exit the device) product may essentially result in uncontrolled growth producing larger gold nanoparticles with higher batch-to-batch variability. This hypothesis is corroborated by the fact that the error bars for the flow rates of 2 and 4 ml/min (short device) are comparable to the product obtained via batch synthesis indicating an unregulated growth due to improper mixing in the collection vial (**Figure 5.9**). Furthermore, the size of the particles obtained at the flow rates at or greater than 2 ml/min are either same as or bigger than the nanoparticles obtained via batch synthesis, which again, is indicative of potentially unregulated growth or ripening of the product.

Table 5.1. Residence times for different flow rates tested on the short device

Flow rate (ml/min)	0.2	0.6	2	4
Residence time (s)	5	1.66	0.5	0.25

Table 5.2 Residence times for various flow rates tested on the long device

Flow rate (ml/min)	2	4	10	13
Residence time (s)	1.64	0.82	0.33	0.25

The products obtained from the long device produced expected results in terms of the decreasing hydrodynamic diameter with an increasing flow rates or alternatively, shorter residence times. The biggest particles were about 53 nm in diameter (hydrodynamic) obtained at a flow rate of 0.2 ml/min and the smallest were about 37 nm synthesized at a flow rate of 4 ml/min. The results were reproducible as indicated by the small error bars in **Figure 5.9**. The particle diameter increased abruptly to about 56 nm for the flow rate of 10 ml/min, which is caused due to ineffective mixing coupled with very short residence time on the chip (**Table 5.2**). Ineffective mixing at 10 ml/min is further evidenced by a big variation in the size of the gold nanoparticles compared to the lower flow rates denoted by the errors bars in **Figure 5.9**. We observed that the variation in terms of the size of the product for similar syntheses (same reaction conditions) conducted at different times was significantly smaller for the runs performed in the herringbone device than the batch synthesis technique. This addresses the challenge of a lack of batch-to-batch reproducibility issues in batch synthesis modes. Furthermore, it is worth emphasizing that all the syntheses were performed in the absence of any capping agents making the reaction very fast. We also found it to be quite challenging to vary the size of the final

product (gold nanoparticle) in the absence of any capping agents for the batch synthesis mode, which is in stark contrast with the ability to tune the size using the developed static mixer.

5.5 Conclusions

In conclusion, we designed an effective millifluidic static mixer that enables fast mixing (~0.8 s) at a wide range of volumetric flow rates ranging from 0.2 ml/min to 10 ml/min. The design was optimized to achieve maximum mixing using finite element modeling (COMSOL). Different prototypes were fabricated out of PMMA that involved the use of a basic CNC milling machine, obviating the need for specialized fabrication facilities. A thorough mixing characterization (dye experiments and confocal imaging) revealed good alignment with the theoretical predictions for these groove mixers. Furthermore, the static mixer is easy to fabricate and can be customized easily to accommodate a wide range of flow rates and additional inlets, beyond just what has been shown in the work. The fabricated mixers were used to synthesize gold nanoparticles to validate the design. The use of the developed static mixer enabled size-controlled synthesis of gold nanoparticles at a wide range of flow rates ranging from 0.2 ml /min to 4 ml/min. Furthermore, the device showed much higher reproducibility compared to the batch synthesis technique at flow rates as high as 4 ml/min. Future work may include incorporation of additional inlets (for stabilizers, capping ligands etc.) to introduce a higher degree of control over the reactions in the static mixer.

Acknowledgements

We gratefully acknowledge financial support from the Dow Chemical Company for research agreement #226772AC and a graduate fellowship to VK. We thank Steven Warren for assistance with TEM imaging.

5.6 Figures

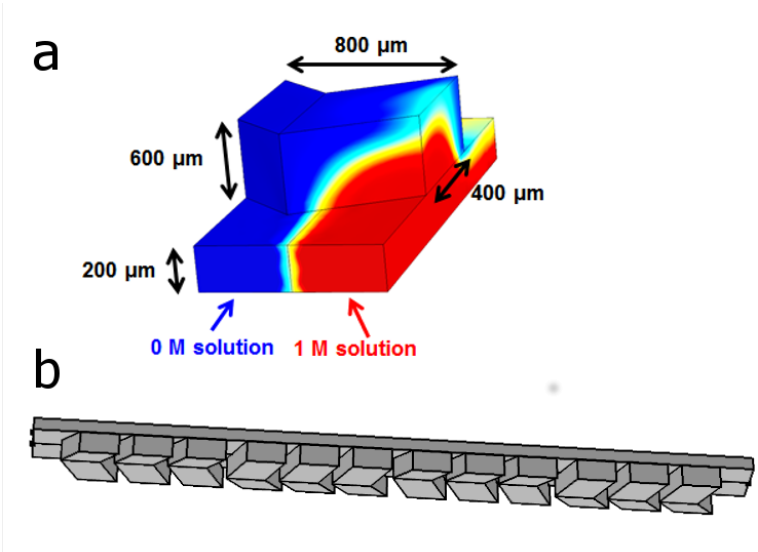

Figure 5.1. (a) The optimized herringbone structure with a width of 400 µm and depth of 600 µm. The red and blue streams denote water with 1 M and 0 M concentrations respectively. **(b)** The geometry used in the full-channel simulation comprising of 12 herringbones with optimum dimensions in sets of 3 (2 cycles). The entire geometry is about 11 mm long.

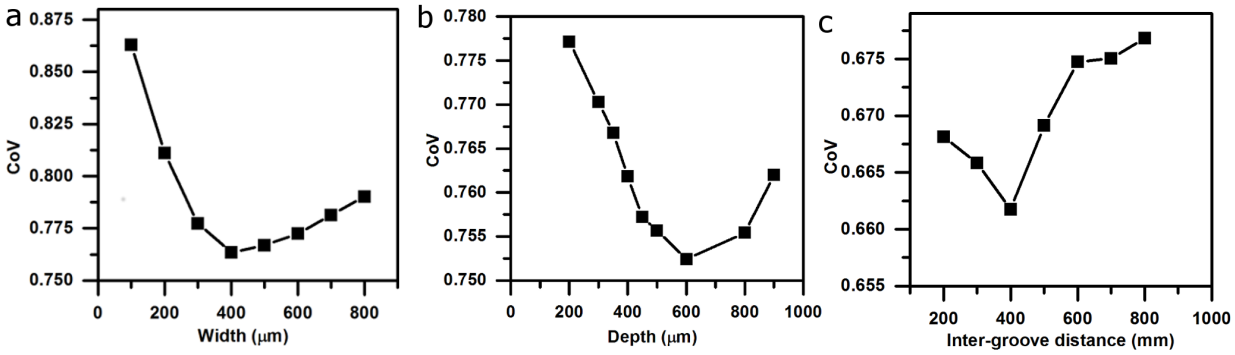

Figure 5.2. Results of the optimization exercise performed using a finite element modeling software, COMSOL. The simulations were performed with one herringbone, except for the optimization of inter-groove distance. CoV for each simulation was computed at the exit of the herringbone structure. The computed CoVs are plotted against **(a)** width, **(b)** depth, and **(c)** inter-groove distance of the herringbone. All the process parameters were kept the same for each optimization run. First, width and depth of the herringbones were optimized, following which the inter-groove distance was optimized using the optimum values for width and depth.

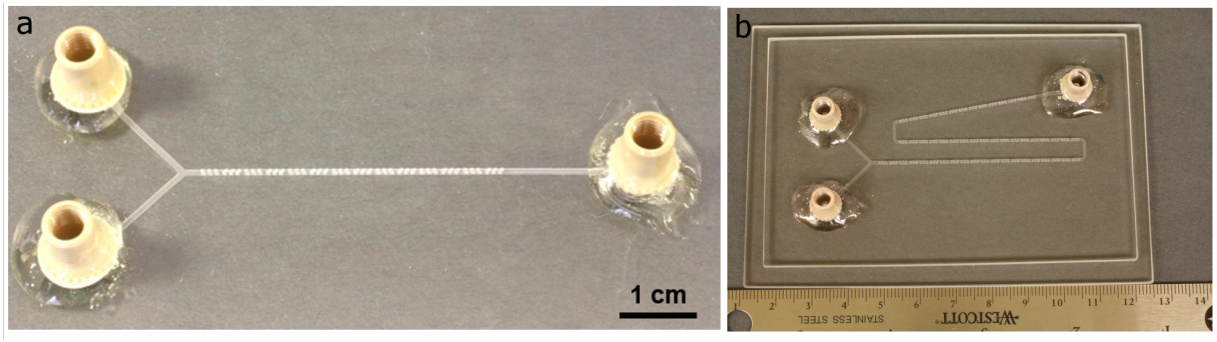

Figure 5.3. The fabricated pieces of **(a)** short device with 14 sets (7 cycles) of herringbones. **(b)** long device comprising of 52 sets of herringbones.

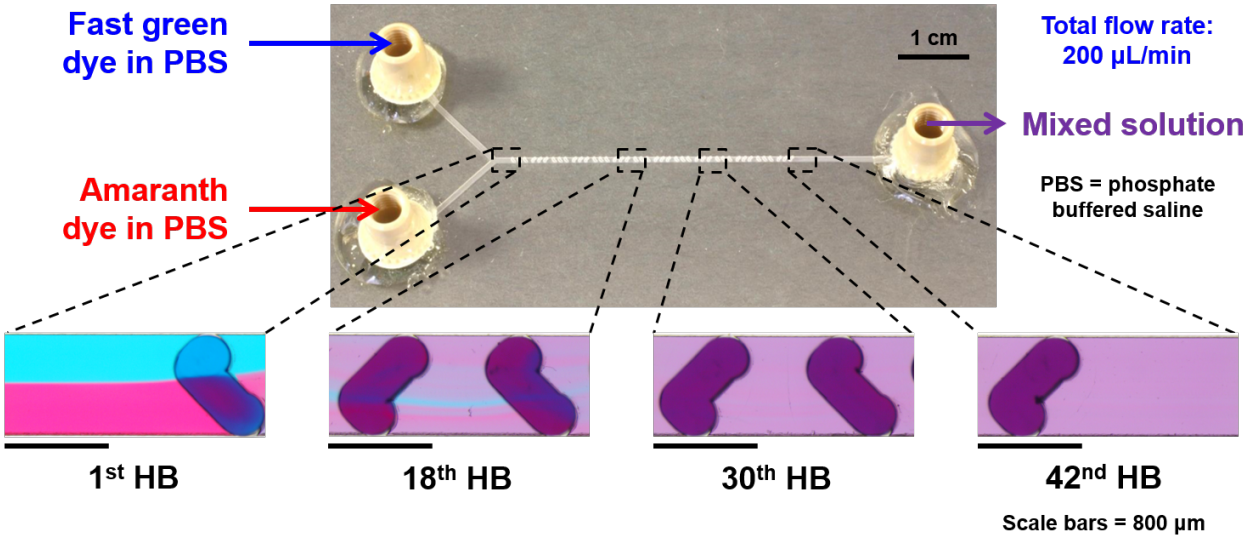

Figure 5.4. The top inset shows Fast green and Amaranth solutions in PBS buffer flowing into the short device through the top and bottom inlets respectively. The bottom insets show magnified images of the channel at the different positions marked on the top inset. The two streams that go in unmixed (1st HB) are effectively mixed by the time they exit the device (42nd HB).

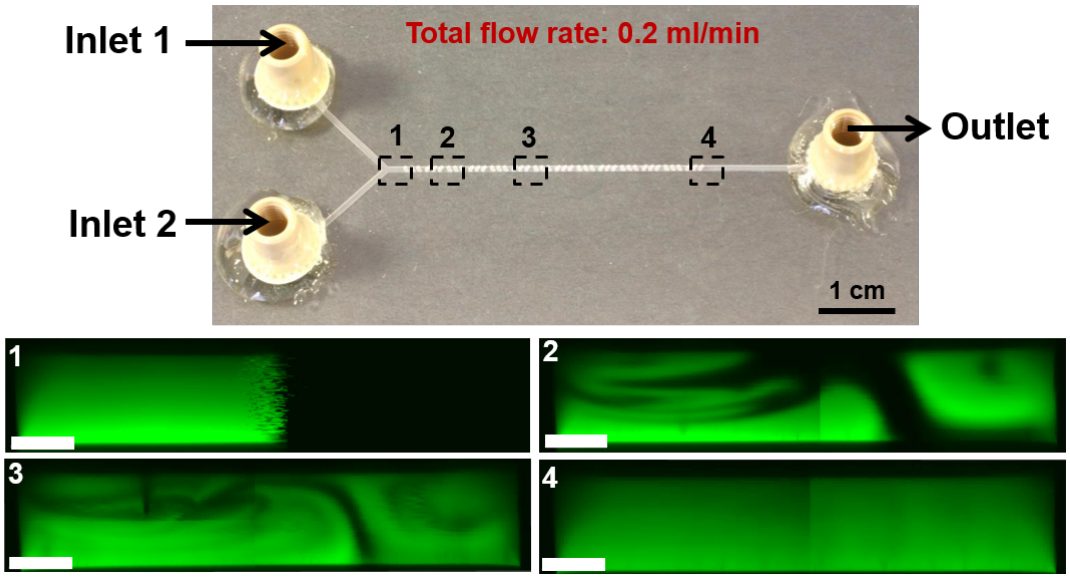

Figure 5.5. The top inset shows the short device with fluorescein solution and E-pure water flowing into the device through inlet 1 and 2 respectively. The total flow rate was kept constant at 0.2 ml/min. The bottom inset shows confocal images of the channel (in z-direction). Each image is marked using a number that corresponds to the position marked by the same number in the top inset. As shown, there is almost no mixing at the beginning of the channel (bottom, image 1). We see characteristic striations or lamellae (bottom, image 2 and 3) forming in the bulk of the liquid as the streams flow through the herringbones. The streams are fully mixed by the time they reach the end of the channel (bottom, image 4). Scale bar (bottom inset) = 100 μm.

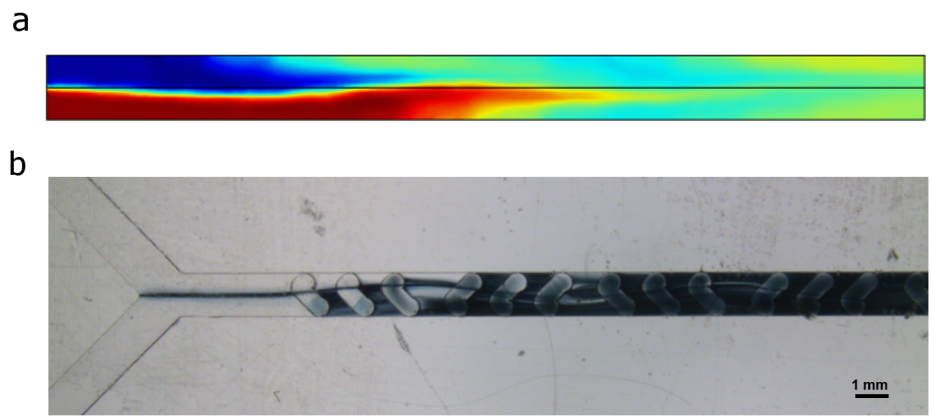

Figure 5.6: (a) COMSOL simulation showing the mixing of two unmixed streams (red and blue). The simulation geometry consists of an 11 mm long channel containing a total of 12 herringbone grooves (in sets of 3). The dimensions of the herringbone grooves were set to the optimized values obatined from the optimization exercise. The unmixed streams shown in red and blue twist and turn (indicated by the swerving interface) along the grooves, which results in the reduction of the diffusive length and fast mixing. **(b)** Gold nanoparticle synthesis in the fabricated static mixer. The stream on top and bottom are 6 mM ascorbic acid solution and 0.375 mM gold (III) chloride hydrate solution in E-pure water respectively. Gold nanoparticles (black) start to form instantly at the interface. The interface (marked by the dark gold nanoparticles) swerves along the herringbone grooves in a similar fashion as shown in the simulation in (a). The simulation and the actual device show very similar results in terms of fluid patterns and mixing. For a direct comparison, the image shows the first 12 herringbones for both the simulation and the actual device.

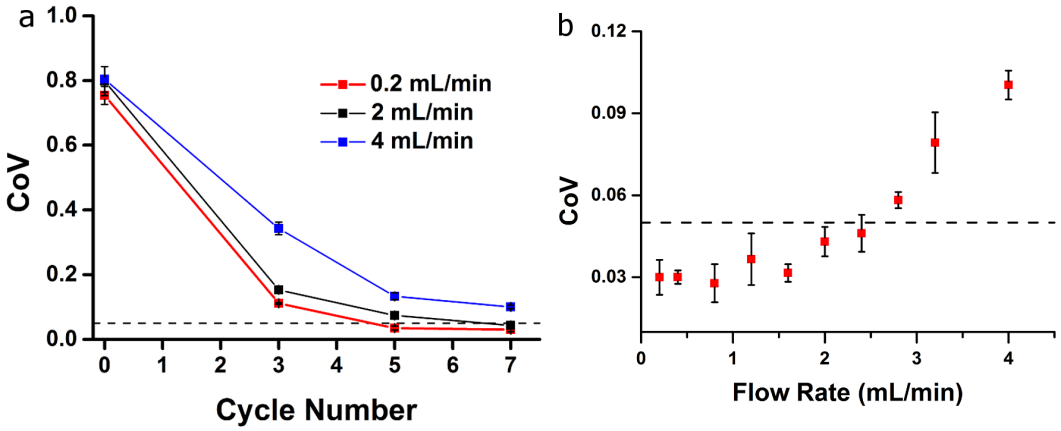

Figure 5.7. (a) Plot showing the variation in CoV with the herringbone cycles for different flow rates. Each cycle comprises of two sets of 3 herringbones. The starting CoV (at cycle 0) is 0.8 instead of 1 because of the concentration dependence of CoV. CoV exhibited an exponential decay with respect to the cycle number as was predicted in equation (10). **(b)** CoVs at the exit are plotted for different flow rates in the short device. As expected, the exit CoV increases with the flow rate, which indicates a lesser extent of mixing for faster flow rates. However, it is worth noting that faster flow rates result in shorter residence times in the mixer compared to the slower flow rates.

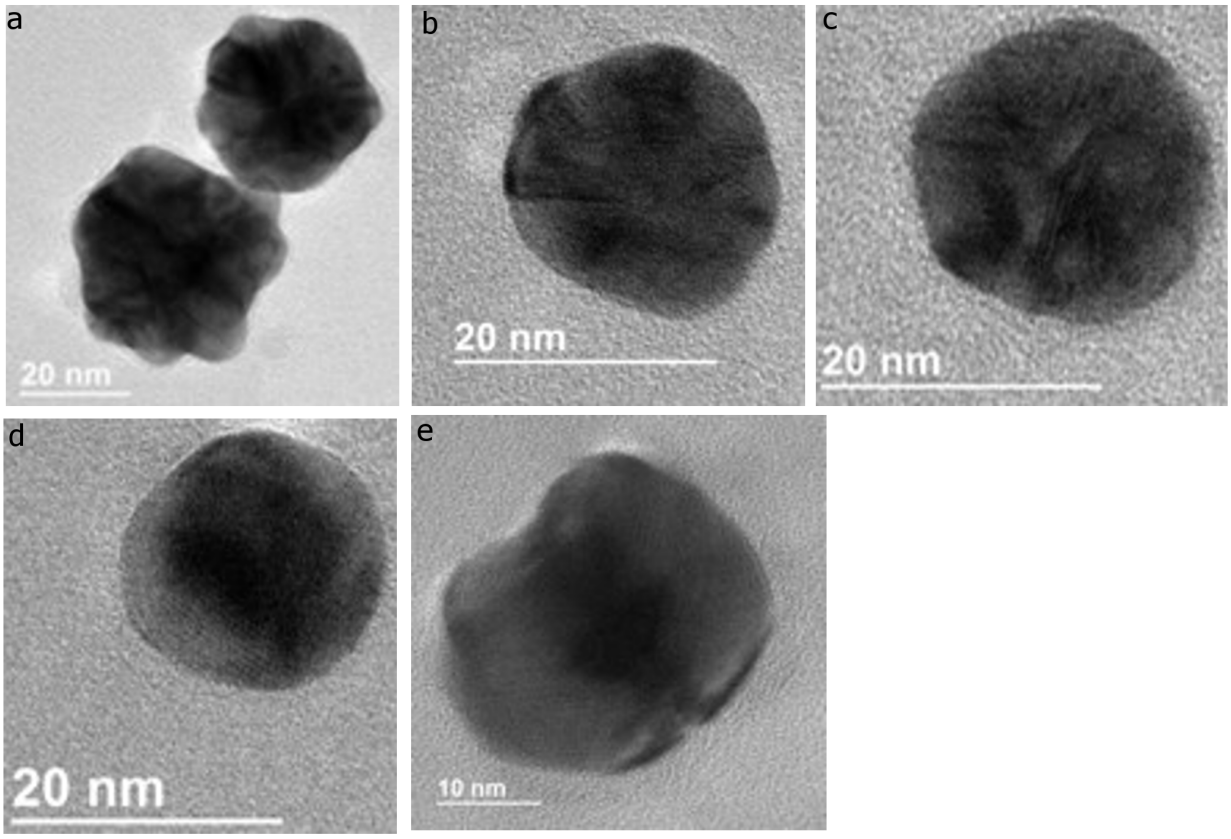

Figure 5.8. TEM images of the gold nanoparticles synthesized in the static mixer (short device) at different flow rates – **(a)** 0.2 ml/min, **(b)** 0.6 ml/min, **(c)** 2 ml, **(d)** 4 ml/min. **(e)** Gold nanoparticle synthesized on batch scale.

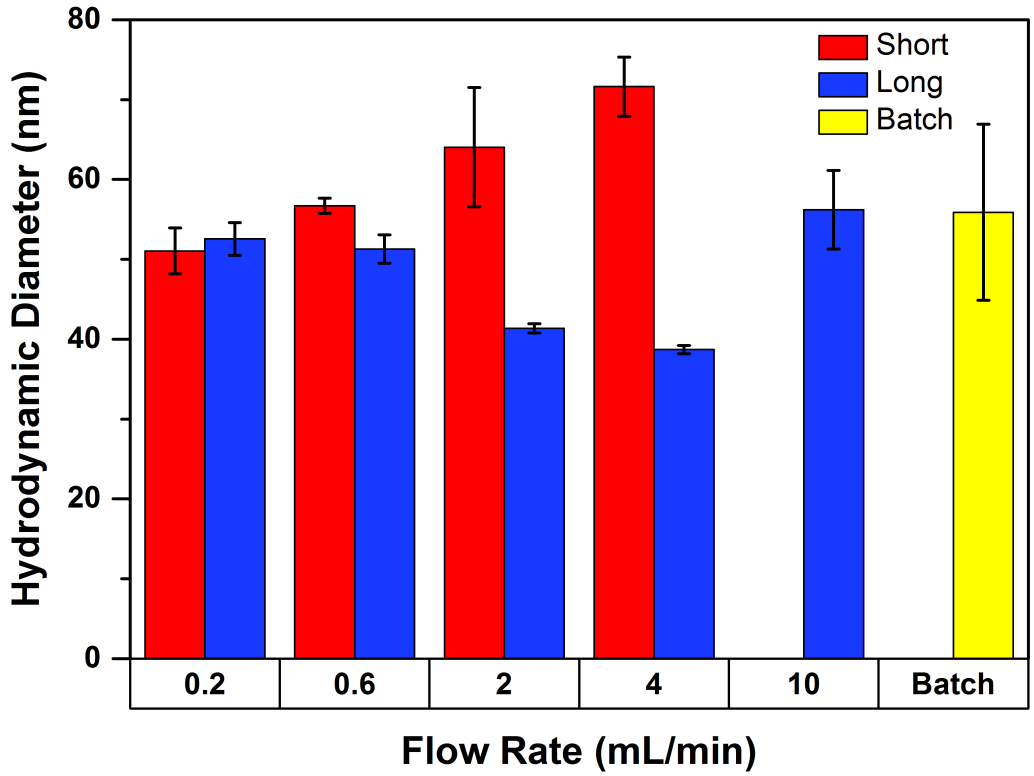

Figure 5.9. The average hydrodynamic diameter of gold nanoparticles is plotted against different flow rates for short (red) and long (blue) devices. The results from the static mixer are compared with the product obtained from the batch synthesis technique (yellow). These hydrodynamic diameters are obtained using the dynamic light scattering (DLS) technique. As expected, the size (average diameter) of the gold nanoparticles decreases with the increasing flow rate in the long device. However, an opposite trend is seen in the short device. A possible explanation for the opposite trend in the short device is incomplete reaction of the precursors in the device due to very short residence times. Incomplete reaction may result into ripening when collected in the vials before performing the DLS measurements. We believe that a higher variability in the product (indicated by the error bars) corroborate the hypothesis. Aside from the inability to control size of the nanoparticles, batch synthesis was also seen to have a greater product variability when compared to the product synthesized in the static mixer on a continuous scale.

5.7 References

1 Angelatos, G. & Hughes, S. Theory and design of quantum light sources from quantum dots embedded in semiconductor-nanowire photonic-crystal systems. *Phys Rev B* 90, doi:ARTN 20540610.1103/PhysRevB.90.205406 (2014).

2 Beveratos, A., Abram, I., Gerard, J. M. & Robert-Philip, I. Quantum optics with quantum dots Towards semiconductor sources of quantum light for quantum information processing. *Eur Phys J D* 68, doi:ARTN 37710.1140/epjd/e2014-50717-x (2014).

3 Orieux, A., Lemaitre, A., Filloux, P., Favero, I., Leo, G. & Ducci, S. Semiconductor integrated sources of quantum light at room temperature. *Proc Spie* 7945, doi:Artn 79452j10.1117/12.871442 (2011).

4 Pisanello, F., Luigi, M., Lemenager, G., Carbone, L., Bramati, A. & De Vittorio, M. Colloidal Quantum Light Sources Based on Asymmetric Semiconductor Nanocrystals. *Int C Trans Opt Netw* (2012).

5 Rohwer, L. E. S., Abrams, B. L., Wilcoxon, J. P. & Thoma, S. G. Development of solid state light sources based on II-VI semiconductor quantum dots. *P Soc Photo-Opt Ins* 5366, 66-74, doi:10.1117/12.527967 (2004).

6 Shields, A. J. Semiconductor quantum light sources. *Nat Photonics* 1, 215-223, doi:10.1038/nphoton.2007.46 (2007).

7 Yamanishi, M. & Suemune, I. Quantum-Mechanical Size Effect Modulation-Light Sources - a New Field-Effect Semiconductor-Laser or Light-Emitting Device. *Jpn J Appl Phys 2* 22, L22-L24, doi:Doi 10.1143/Jjap.22.L22 (1983).

8 Nam, S., Oh, N., Zhai, Y. & Shim, M. High efficiency and optical anisotropy in double-heterojunction nanorod light-emitting diodes. *Acs Nano* 9, 878-885, doi:10.1021/nn506577p (2015).

9 Oh, N., Nam, S., Zhai, Y., Deshpande, K., Trefonas, P. & Shim, M. Double-heterojunction nanorods. *Nat Commun* 5, doi:10.1038/ncomms4642 (2014).

10 Shim, M. & Guyot-Sionnest, P. Organic-capped ZnO nanocrystals: Synthesis and n-type character. *J Am Chem Soc* 123, 11651-11654, doi:10.1021/ja0163321 (2001).

11 Crooks, R. M., Zhao, M. Q., Sun, L., Chechik, V. & Yeung, L. K. Dendrimer-encapsulated metal nanoparticles: Synthesis, characterization, and applications to catalysis. *Accounts Chem Res* 34, 181-190, doi:10.1021/ar000110a (2001).

12 Tada, H., Kiyonaga, T. & Naya, S. Rational design and applications of highly efficient reaction systems photocatalyzed by noble metal nanoparticle-loaded titanium(IV) dioxide. *Chem Soc Rev* 38, 1849-1858, doi:10.1039/b822385h (2009).

13 Wittenberg, N. J. & Haynes, C. L. Using nanoparticles to push the limits of detection. *Wires Nanomed Nanobi* 1, 237-254, doi:10.1002/wnan.019 (2009).

14 Bally, M. & Voros, J. Nanoscale labels: nanoparticles and liposomes in the development of high-performance biosensors. *Nanomedicine-Uk* 4, 447-467, doi:10.2217/Nnm.09.16 (2009).

15 Sun, C., Lee, J. S. H. & Zhang, M. Q. Magnetic nanoparticles in MR imaging and drug delivery. *Adv Drug Deliver Rev* 60, 1252-1265, doi:10.1016/j.addr.2008.03.018 (2008).

16 Ito, A., Shinkai, M., Honda, H. & Kobayashi, T. Medical application of functionalized magnetic nanoparticles. *J Biosci Bioeng* 100, 1-11, doi:10.1263/jbb.100.1 (2005).

17 Marre, S. & Jensen, K. F. Synthesis of micro and nanostructures in microfluidic systems. *Chemical Society reviews* 39, 1183-1202, doi:10.1039/b821324k (2010).

18 Nightingale, A. M. & de Mello, J. C. Microscale synthesis of quantum dots. *Journal of Materials Chemistry* 20, 8454, doi:10.1039/c0jm01221a (2010).

19 Phillips, T. W., Lignos, I. G., Maceiczyk, R. M., deMello, A. J. & deMello, J. C. Nanocrystal synthesis in microfluidic reactors: where next? *Lab on a chip* 14, 3172-3180, doi:10.1039/c4lc00429a (2014).

20 Yang, H., Luan, W., Wan, Z., Tu, S.-t., Yuan, W.-K. & Wang, Z. M. Continuous Synthesis of Full-Color Emitting Core/Shell Quantum Dots via Microreaction. *Crystal Growth & Design* 9, 4807-4813, doi:10.1021/cg900652y (2009).

21 Phillips, T. W., Lignos, I. G., Maceiczyk, R. M., deMello, A. J. & deMello, J. C. Nanocrystal synthesis in microfluidic reactors: where next? *Lab on a chip* 14, 3172-3180, doi:10.1039/c4lc00429a (2014).

22 Edel, J. B., Fortt, R., deMello, J. C. & deMello, A. J. Microfluidic routes to the controlled production of nanoparticles. *Chemical communications*, 1136-1137, doi:Doi 10.1039/B202998g (2002).

23 Huebner, A., Sharma, S., Srisa-Art, M., Hollfelder, F., Edel, J. B. & Demello, A. J. Microdroplets: a sea of applications? *Lab on a chip* 8, 1244-1254, doi:10.1039/b806405a (2008).

24 Jensen, K. F. Microreaction engineering - is small better? *Chem Eng Sci* 56, 293-303, doi:Doi 10.1016/S0009-2509(00)00230-X (2001).

25 Song, Y., Hormes, J. & Kumar, C. S. Microfluidic synthesis of nanomaterials. *Small* 4, 698-711, doi:10.1002/smll.200701029 (2008).

26 Park, J. I., Saffari, A., Kumar, S., Günther, A. & Kumacheva, E. Microfluidic Synthesis of Polymer and Inorganic Particulate Materials. *Annual Review of Materials Research* 40, 415-443, doi:10.1146/annurev-matsci-070909-104514 (2010).

27 Shalom, D., Wootton, R. C. R., Winkle, R. F., Cottam, B. F., Vilar, R., deMello, A. J. & Wilde, C. P. Synthesis of thiol functionalized gold nanoparticles using a continuous flow microfluidic reactor. *Materials Letters* 61, 1146-1150, doi:10.1016/j.matlet.2006.06.072 (2007).

28 Duraiswamy, S. & Khan, S. A. Droplet-Based Microfluidic Synthesis of Anisotropic Metal Nanocrystals. *Small* 5, 2828-2834, doi:10.1002/smll.200901453 (2009).

29 Boleininger, J., Kurz, A., Reuss, V. & Sonnichsen, C. Microfluidic continuous flow synthesis of rod-shaped gold and silver nanocrystals. *Phys Chem Chem Phys* 8, 3824-3827, doi:10.1039/b604666e (2006).

30 Yang, H. W., Luan, W. L., Tu, S. T. & Wang, Z. M. High-Temperature Synthesis of CdSe Nanocrystals in a Serpentine Microchannel: Wide Size Tunability Achieved under a Short Residence Time. *Crystal Growth & Design* 9, 1569-1574, doi:Doi 10.1021/Cg800425f (2009).

31 Baek, J., Allen, P. M., Bawendi, M. G. & Jensen, K. F. Investigation of indium phosphide nanocrystal synthesis using a high-temperature and high-pressure continuous flow microreactor. *Angewandte Chemie* 50, 627-630, doi:10.1002/anie.201006412 (2011).

32 Nightingale, A. M., Krishnadasan, S. H., Berhanu, D., Niu, X., Drury, C., McIntyre, R., Valsami-Jones, E. & deMello, J. C. A stable droplet reactor for high temperature nanocrystal synthesis. *Lab on a chip* 11, 1221-1227, doi:10.1039/c0lc00507j (2011).

33 Dendukuri, D., Pregibon, D. C., Collins, J., Hatton, T. A. & Doyle, P. S. Continuous-flow lithography for high-throughput microparticle synthesis. *Nature materials* 5, 365-369, doi:10.1038/nmat1617 (2006).

34 Pregibon, D. C., Toner, M. & Doyle, P. S. Multifunctional encoded particles for high-throughput biomolecule analysis. *Science* 315, 1393-1396, doi:10.1126/science.1134929 (2007).

35 Frenz, L., El Harrak, A., Pauly, M., Begin-Colin, S., Griffiths, A. D. & Baret, J. C. Droplet-based microreactors for the synthesis of magnetic iron oxide nanoparticles. *Angew Chem Int Edit* 47, 6817-6820, doi:10.1002/anie.200801360 (2008).

36 Lee, I., Yoo, Y., Cheng, Z. & Jeong, H. K. Generation of Monodisperse Mesoporous Silica Microspheres with Controllable Size and Surface Morphology in a Microfluidic Device. *Advanced Functional Materials* 18, 4014-4021, doi:10.1002/adfm.200801093 (2008).

37 Cottam, B. F., Krishnadasan, S., deMello, A. J., deMello, J. C. & Shaffer, M. S. P. Accelerated synthesis of titanium oxide nanostructures using microfluidic chips. *Lab on a chip* 7, 167-169, doi:10.1039/b616068a (2007).

38 Khvostichenko, D. S., Kondrashkina, E., Perry, S. L., Pawate, A. S., Brister, K. & Kenis, P. J. A. An X-ray transparent microfluidic platform for screening of the phase behavior of lipidic mesophases. *The Analyst* 138, 5384-5395, doi:10.1039/c3an01174g (2013).

39 Perry, S. L., Guha, S., Pawate, A. S., Bhaskarla, A., Agarwal, V., Nair, S. K. & Kenis, P. J. A. A microfluidic approach for protein structure determination at room temperature via on-chip anomalous diffraction. *Lab on a chip* 13, 3183-3187, doi:10.1039/c3lc50276g (2013).

40 Goyal, S., Thorson, M. R., Schneider, C. L., Zhang, G. G. Z., Gong, Y. C. & Kenis, P. J. A. A Microfluidic Platform for Evaporation-based Salt Screening of Pharmaceutical Parent compounds. *Lab on a chip* 13, 1708-1723, doi:10.1039/c3lc41271g (2013).

41 Horstman, E. M., Goyal, S., Pawate, A., Lee, G., Zhang, G. G. Z., Gong, Y. C. & Kenis, P. J. A. Crystallization Optimization of Pharmaceutical Solid Forms with X-ray Compatible Microfluidic Platforms. *Crystal Growth & Design* 15, 1201-1209, doi:10.1021/cg5016065 (2015).

42 DeMello, A. J. Control and detection of chemical reactions in microfluidic systems. *Nature* 442, 394-402, doi:10.1038/nature05062 (2006).

43 Lohse, S. E., Eller, J. R., Sivapalan, S. T., Plews, M. R. & Murphy, C. J. A Simple Millifluidic Benchtop Reactor System for the High-Throughput Synthesis and Functionalization of Gold Nanoparticles with Different Sizes and Shapes. *Acs Nano* 7, 4135-4150, doi:10.1021/nn4005022 (2013).

44 Li, Y. H., Sanampudi, A., Reddy, V. R., Biswas, S., Nandakumar, K., Yemane, D., Goettert, J. & Kumar, C. S. S. R. Size Evolution of Gold Nanoparticles in a Millifluidic Reactor. *Chemphyschem : a European journal of chemical physics and physical chemistry* 13, 177-182, doi:10.1002/cphc.201100726 (2012).

45 Naughton, M. S., Kumar, V., Bonita, Y., Deshpande, K. & Kenis, P. J. High temperature flow synthesis of CdSe/CdS/ZnS, CdS/ZnS, and CdSeS/ZnS nanocrystals *Nanoscale*, doi:10.1039/C5NR04510J (2015).

46 Biswas, S., Miller, J. T., Li, Y., Nandakumar, K. & Kumar, C. S. Developing a millifluidic platform for the synthesis of ultrasmall nanoclusters: ultrasmall copper nanoclusters as a case study. *Small* 8, 687-698, doi:10.1002/smll.201102100 (2012).

47 Nightingale, A. M., Bannock, J. H., Krishnadasan, S. H., O'Mahony, F. T. F., Haque, S. A., Sloan, J., Drury, C., McIntyre, R. & deMello, J. C. Large-scale synthesis of nanocrystals in a multichannel droplet reactor. *Journal of Materials Chemistry A* 1, 4067, doi:10.1039/c3ta10458c (2013).

48 Lim, J. M., Swami, A., Gilson, L. M., Chopra, S., Choi, S., Wu, J., Langer, R., Karnik, R. & Farokhzad, O. C. Ultra-High Throughput Synthesis of Nanoparticles with Homogeneous Size Distribution Using a Coaxial Turbulent Jet Mixer. *Acs Nano* 8, 6056-6065, doi:10.1021/nn501371n (2014).

49 Tice, J. D., Lyon, A. D. & Ismagilov, R. F. Effects of viscosity on droplet formation and mixing in microfluidic channels. *Analytica Chimica Acta* 507, 73-77, doi:10.1016/j.aca.2003.11.024 (2004).

50 Christopher, G. F., Noharuddin, N. N., Taylor, J. A. & Anna, S. L. Experimental observations of the squeezing-to-dripping transition in T-shaped microfluidic junctions. *Physical Review E* 78, doi:ARTN 03631710.1103/PhysRevE.78.036317 (2008).

51 Christopher, G. F. & Anna, S. L. Microfluidic methods for generating continuous droplet streams. *Journal of Physics D: Applied Physics* 40, R319-R336, doi:10.1088/0022-3727/40/19/r01 (2007).

52 Nightingale, A. M. & Demello, J. C. Segmented flow reactors for nanocrystal synthesis. *Advanced materials* 25, 1813-1821, doi:10.1002/adma.201203252 (2013).

53 Johnson, B. K. & Prud'homme, R. K. Chemical processing and micromixing in confined impinging jets. *Aiche Journal* 49, 2264-2282, doi:Doi 10.1002/Aic.690490905 (2003).

54 Marchisio, D. L., Rivautella, L. & Barresi, A. A. Design and scale-up of chemical reactors for nanoparticle precipitation. *Aiche Journal* 52, 1877-1887, doi:10.1002/aic.10786 (2006).

55 Watts, P. & Haswell, S. J. The application of micro reactors for organic synthesis. *Chemical Society reviews* 34, 235-246, doi:10.1039/b313866f (2005).

56 Haswell, S. J., Middleton, R. J., O'Sullivan, B., Skelton, V., Watts, P. & Styring, P. The application of micro reactors to synthetic chemistry. *Chemical communications*, 391-398, doi:Doi 10.1039/B008496o (2001).

57 Knitter, R., Gohring, D., Risthaus, P. & Hausselt, J. Microfabrication of ceramic microreactors. *Microsystem Technologies* 7, 85-90, doi:Doi 10.1007/S005420100107 (2001).

58 Lynn, N. S. & Dandy, D. S. Geometrical optimization of helical flow in grooved micromixers. *Lab on a chip* 7, 580-587, doi:10.1039/b700811b (2007).

59 Stroock, A. D. & McGraw, G. J. Investigation of the staggered herringbone mixer with a simple analytical model. *Philos T Roy Soc A* 362, 971-986, doi:10.1098/rsta.2003.1357 (2004).

60 Stroock, A. D., Dertinger, S. K., Ajdari, A., Mezic, I., Stone, H. A. & Whitesides, G. M. Chaotic mixer for microchannels. *Science* 295, 647-651, doi:10.1126/science.1066238 (2002).

61 Polte, J., Erler, R., Thunemann, A. F., Sokolov, S., Ahner, T. T., Rademann, K., Emmerling, F. & Kraehnert, R. Nucleation and Growth of Gold Nanoparticles Studied via in situ Small Angle X-ray Scattering at Millisecond Time Resolution. *Acs Nano* 4, 1076-1082, doi:10.1021/nn901499c (2010).

CHAPTER 6
CONCLUSIONS AND FUTURE DIRECTIONS

Despite numerous advantages, semiconductor nanomaterials are yet to realize their full potential on a commercial scale partly because of a lack of scalable synthesis techniques. Furthermore, recent regulations inhibiting the use of Cadmium in consumer products have posed even more stringent conditions on the use of semiconductor nanomaterials in consumer products. Amidst these challenges, continuous flow synthesis is expected to address the aforementioned issue of a lack of scalable synthesis technique and there have been some major studies reporting on the large scale continuous flow synthesis of high performing Cd-based nanomaterials. However, there is only a limited literature on the continuous flow synthesis of Cd-free particles. Furthermore, there is no major study on scalable continuous flow synthesis of luminescent Cd-free nanoparticles. Our efforts in the last few years have focused to fill this gap by working on the design, fabrication, and application of continuous flow platforms that enable scalable multistep synthesis of highly luminescent Cd-free nanomaterials in a controlled environment.

To date a manuscript reporting on high throughput continuous flow synthesis of high quality, multilayered Cd-based isotropic particles has been published (Chapter 2). Cd-based quantum dots with different morphologies (core, core-shell, core-shell-shell) were synthesized using a continuous flow reactor that was designed and fabricated in-house. The synthesized particles exhibited quantum yields in excess of 60% with a narrow full width at half maximum (FWHM) of ~33 nm. The product was characterized using absorbance and fluorescence spectroscopy, ICP OES, and TEM. In the later stages of the project, the reactor setup was modified to enable air-sensitive reactions composed of solid/viscos reactants. The design modifications were

particularly necessary since the majority of the anisotropic nanoparticles syntheses (of interest) involve precursors that are solid at room temperature. The modified reactor setup enabled the synthesis of highly uniform anisotropic CdSe nanoparticles. The same setup was further used to synthesize ZnSe nanowires and nanorods. To our knowledge, this will be the first instance of synthesis of anisotropic CdSe and ZnSe nanoparticles in a continuous flow system. All synthesized particles were characterized using UV-Vis spectroscopy, XRD, ICP OES, and HRTEM confirming their composition and morphology. A patent application (Serial # PCT/US2016/017906) describing our work on the continuous flow synthesis of anisotropic CdSe and ZnSe nanoparticles has been successfully submitted. A second manuscript discussing the results on anisotropic CdSe (Cd-based) and ZnSe (Cd-free) nanoparticles is ready for submission. We then went on to modify the reactor to enable continuous flow multistep synthesis of highly luminescent InP/ZnSeS (Cd-free) particles as described in **Chapter 4**. The reactor was redesigned to reduce any dispersion effects inside the reactor. The new continuous flow reactor setup also included inline analysis capabilities to monitor the absorption and emission properties of the product. We demonstrated the multistep synthesis of InP/ZnSeS particles that exhibited quantum yields as high as 55% (unoptimized results) in our flow reactor. The highest quantum yield achieved in our flow reactor exceeds the prior best results for Cd-free particles synthesized in any continuous flow system. Furthermore, we were able to tune the particle size by varying different process parameters such as the flow rate, reactor temperatures, and precursor concentrations. This enabled us to span the entire visible spectrum with the In-based particles synthesized in our reactor. The operating flow rates were of the order of 1 ml/min that can be improved further by making quick modifications to the reactor. Effective and fast mixing is critical to obtain uniform nanocrystals. To tackle the problem of fast mixing without incurring

high pressure drops, we developed a millifluidic static mixer based on the concept of staggered herringbone structures. The millifluidic mixer enabled fast mixing (~0.8 s) for a wide range flow rates (0.2 – 4 ml/min). We were able to demonstrate good size control for gold nanoparticles synthesized in the mixer via a fast reduction reaction. The mixer also yielded low product variability compared to the batch synthesis technique. The results pertaining to design, fabrication, and validation of the developed fast millifluidic static mixer are discussed in **Chapter 5**.

In the future, the performance of the InP-based nanoparticles can be further improved by optimizing the synthesis conditions and synthesis strategy for the continuous flow reactor. A sensitivity analysis can be performed to identify the important process parameters based on their impact on quantum yield of the final product. Once the important process parameters have been identified, a comprehensive set of experiments can be designed to maximize the quantum yield of the final product based on the "Design of Experiments" principles. To ensure a distinct layer of ZnSe shell around the InP cores, the shell formation step can be performed in two separate steps. First, a layer of ZnSe shell can be grown over InP particles followed by the growth of a thick ZnS layer in a separate step. The results of the two-step shell formation can then be compared with the single-step shell formation to distinguish the more effective shell-growth procedure. In addition to optimizing the synthetic strategies to achieve high quantum yields, the reactor setup can also be applied to obtain more insight into the growth mechanism of InP particles, building up on the preliminary evidence of aggregative growth exhibited by InP particles observed in the continuous flow reactor.